GDAŃSK UNIVERSITY
OF TECHNOLOGY
Faculty of Applied Physics and
Mathematics

The author of the PhD dissertation: mgr inż. Maciej Klein
Scientific discipline: Physics

DOCTORAL DISSERTATION

Title of PhD dissertation: Magnetic field effects in dye-sensitized and organic solar cells

Title of PhD dissertation (in Polish): Efekty magnetyczne w barwnikowych i organicznych ogniwach słonecznych

Supervisor *signature*
dr hab. inż. Waldemar Stampor, prof. nadzw. PG

Gdańsk, year 2018

GDAŃSK UNIVERSITY OF TECHNOLOGY
FACULTY OF APPLIED PHYSICS AND MATHEMATICS

Doctor of Philosophy Dissertation

Magnetic field effects in dye-sensitized and organic solar cells

by

Maciej Klein

Supervisor: dr hab. inż. Waldemar Stampor, prof. nadzw. PG

Gdańsk, 2018

This work was supported by the Polish Ministry of Science and Higher Education under "Diamond Grant" (0228/DIA/2013/42).

This work was supported by the Foundation for Polish Science (FNP).

Contents

List of Symbols and Abbreviations

ΔE_{ST}	Singlet-triplet splitting energy
ℓ	Orbital quantum number
ϵ_0	Vacuum permittivity
η	Solar-to-electric power conversion efficiency
γ_{ST}	Singlet-triplet interaction constant
γ_{Tq}	Triplet-charge carrier interaction constant
γ_{TT}	Triplet-triplet interaction constant
$\hat{H}$	Hamiltonian operator
$\hbar$	Reduced Planck constant
$\jmath$	Total angular momentum quantum number
μ_B	Bohr magneton
ω_p	Precession frequency
ω_{hf}	Hyperfine field precession frequency
ω_{hop}	Hopping frequency
$\vec{\mu}_\ell$	Orbital magnetic dipole moment
$\vec{\mu}_\jmath$	Total magnetic dipole moment
$\vec{\mu}_s$	Spin magnetic dipole moment
$\vec{L}_\ell$	Orbital angular momentum
$\vec{L}_\jmath$	Total angular momentum
$\vec{L}_s$	Spin angular momentum (spin)
^{2}TD	Doublet trion

^{4}TD	Quartet trion
A_C	Electron affinity
A_G	Electron affinity of an isolated molecule
B	Magnetic field strength (induction)
B_{HF}	Hyperfine magnetic field strength
c	Speed of light
CT	Charge-transfer
e	Elementary charge
$e-h$	Electron-hole
E_C	Coulomb integral energy
E_G	Energy gap
E_S	Singlet energy level
E_T	Triplet energy level
E_{CT}	Charge-transfer state energy
FF	Fill factor
g	Lande factor
g_e	Lande g factor for an electron
g_h	Lande g factor for a hole
I_C	Ionization energy of a crystal
I_G	Ionization energy of an isolated molecule
I_{MP}	Current at maximum power point
I_{rad}	Irradiance
I_{SC}	Short-circuit current
J	Exchange interactions energy
J_{ex}	Exchange integral

k_B	Boltzmann constant
L_D	Diffusion length
LC	Ligand-centered
$LMCT$	Ligand-to-metal charge transfer
m_ℓ	Magnetic orbital quantum number
m_e	Electron mass
m_s	Magnetic spin quantum number
MC	Metal-centered
$MLCT$	Metal-to-ligand charge transfer
P	Power
P_e	Electron polarization energy
P_h	Hole polarization energy
P_{MAX}	Maximum value of power
s, S	Spin quantum number
V_{MP}	Voltage at maximum power point
V_{OC}	Open circuit voltage
A	Acceptor
AFM	Atomic force microscopy
AM	Air mass
BHJ	Bulk-heterojunction
BP	Bipolaron
D	Donor or doublet (depending on the context)
DFT	Density functional theory
DI	Deionized
DSSC	Dye-sensitized solar cell

EHP	Electron-hole pair
EL	Electroluminescence
EPR	Electron paramagnetic resonance
FSM	Fine structure modulation
FTO	Fluorine-doped tin oxide
HFM	Hyperfine interaction modulation
HOMO	Highest occupied molecular orbital
HWHM	Half width at half maximum
I-V	Current-voltage
IC	Internal conversion
IPA	Isopropyl alcohol
ISC	Intersystem crossing
ITO	Indium-tin oxide
LED	Light emitting diode
LUMO	Lowest unoccupied molecular orbital
MC	Magneto-conductivity
MEL	Magneto-electroluminescence
MFE	Magnetic field effect
MO	Molecular orbital
MPC	Magneto-photocurrent
MPL	Magneto-photoluminescence
NP	Nanoparticle
NT	Nanotube
OMAR	Organic magnetoresistance
OPV	Organic photovoltaics

PCE	Photoconversion efficiency
PHJ	Planar-heterojunction
PPMS	Physical property measurement system
PV	Photovoltaics
S	Singlet
SEM	Scanning electron microscopy
STC	Standard test conditions
T	Triplet
TCO	Transparent conductive oxide
TTA	Triplet-triplet annihilation
USMFE	Ultrasmall magnetic field effect
VR	Vibrational relaxation
XRD	X-ray diffraction
ZFS	Zero-field splitting

1 Introduction

1.1 Introductory remarks

Growing energy demand along with fossil fuels deficiency and the need for global environment protection has made the development of non-polluting renewable energy technologies of a highest priority in science and technology [1, 2]. Solar technologies, especially photovoltaics (PV), are the most promising ones. Over the past several years, achievements made in the field of solar cells resulted in a great reduction of the cost of PV electrical energy such that it is rapidly approaching the cost of electrical energy produced by power plants fueled by coal, natural gas and nuclear reactors [3]. Nowadays solar cells are divided into three categories, or generations. The first generation is based on monocrystalline and polycrystalline silicon, the second generation on thin films of various inorganic semiconducting materials (CdTe, GaAs, CuInGaSe - CIGS) while the third generation consist mainly of organic materials and organic-inorganic systems incorporated into organic or polymer, dye-sensitized and perovskite solar cells [4]. However, the relatively high production costs of the first and the second generation of solar cells and the fact that their production processes, involves high energy consumption, as well as the use of ultra pure materials and toxic chemicals, hamper a widespread use of these devices [5]. So, it is reasonable to investigate other materials capable to convert solar radiation into electricity and meet the requirements for sustainable development. An interesting alternative is the use of organic and dye-sensitized solar cells, though their performance parameters and long-term stability are still inferior to commercially available crystalline silicon devices. Performance improvement of these devices is expected to occur due to intensive research in photoactive materials and in-depth understanding of the fundamental physical processes determining the operation of solar cell.

1.2 Aims and objectives

All photovoltaic devices generate photocurrent through a series of the following events: light absorption, electronic excitation, charge carriers separation and their collection by electrodes. Unlike in conventional solar cells, where free carriers are generated in a single layer of silicon directly after photoexcitation, in organic and dye-sensitized solar cells the electronic excitations (excitons) are strongly bound entities which dissociate mainly at an interface of electron donor (D) and electron acceptor (A) layers. Due to low relative permittivities of organic materials this primary charge separation step proceeds through an intermediate stage of coulombically bound electron (A^-) - hole (D^+) pair. The electron - hole pair dissociation into free charge carriers and their recombination are generally recognized as basic electronic processes limiting photoconversion efficiency of organic material-based solar cells. Moreover, multiplicity of various electronic states, of neutral (molecular excitons) or ionic (free charge carriers or electron-hole pairs) character, and their mutual interactions affect the interrelations between relevant electronic processes. If electronic states are endowed with magnetic moment (as in triplet or doublet species) their contribution to charge photogeneration can be identified and controlled by a magnetic field. Therefore, the magnetic field effect technique, in which photocurrent is modulated by the external magnetic field, provides unique opportunities to unravel the mechanisms underlying efficient operation of solar cells.

The aim of this thesis is to understand the electronic processes limiting the operation of efficient photovoltaic cells with particular emphasis on the role of electronic states endowed with magnetic dipole moment.

In order to achieve this aim the following issues have been addressed:

- literature review, in particular, concerning the magnetic field effects in organic solids,
- selection of appropriate materials for photoactive layers and electrodes,
- design of solar cell architectures and structures of electrodes,
- fabrication and characterization of dye-sensitized solar cells and organic solar cells,
- design, assembly and calibration of experimental setups for phtocurrent measurements in an external magnetic field, applying a light modulation technique to derive small signals from an electronic background noise,

- carry out measurements and analyze their results.

The detailed objectives of this dissertation are as follows:

- reveal that photogeneration of free charge carriers in dye-sensitized solar cells proceeds *via* the intermediate state of electron-hole pair, similarly as observed previously in organic solar cells,
- show that the photocurrent in organic and dye-sensitized solar cells can be affected and controlled by the external magnetic field,
- experimentally modify the radius and spin coherence time of electron-hole pairs in dye-sensitized solar cells by the photoanode morphology and the electronic orbital structure of various dye molecules,
- unravel the role of electron-hole pair (or charge-transfer state) spin in a photocurrent generation process in organic solar cells depending on electron donor to electron acceptor concentration ratio.

The thesis consist of seven chapters. First three chapters introduce the reader to the issue of dye-sensitized and organic solar cells, giving basic information about their construction and operating principles. Moreover, a physical background regarding electronically excited states in molecular systems is presented. Chapter 4 begins with a description of magnetic properties of electron and nuclear spins. Afterwards, possible spin dependent processes underlying magnetic field effects in organic solids are thoroughly discussed. The chapter concludes with a literature review on the magnetic field effects in dye-sensitized and organic solar cells. Chapters 5 and 6 are based on the work of the author (and co-workers). Materials used, samples and solar cells preparation and characterization methods as well as experimental techniques applied are presented in chapter 5. The experimental results and discussion are given in chapter 6 divided into two sections. Section 6.1 deals with dye-sensitized solar cells with sensitizers based on organic molecules (squaraine) and ruthenium complexes, while section 6.2 regards organic solar cells of a single-layer (squaraine) and bulk-heterojunction (squaraine:fullerene) architecture. The dissertation ends with final remarks and conclusions.

Results presented in this thesis were published in:

- M. Klein, S. Majumdar, P. Zassowski and W. Stampor, *Unravelling the role of electron-hole pair spin in exciton dissociation in squaraine-based organic solar cells by magneto-photocurrent measurements*, Journal of Materials Chemistry C, 2018, **6**, 482-490,

- M. Klein, R. Pankiewicz, M. Zalas and W. Stampor, *Magnetic field effects in dye-sensitized solar cells controlled by different cell architecture*, Scientific Reports, Nature, 2016, **6**, 30077,
- D. Pelczarski, P. Grygiel, K. Falkowski, M. Klein and W. Stampor, *Electromodulation and magnetomodulation of exciton dissociation in electron donor (starburst amine) : electron acceptor (bathocuproine) system*, Organic Electronics, 2016, **25**, 362-376,
- M. Zalas, B. Gierczyk, M. Klein, K. Siuzdak, T. Pędziński and T. Łuczak, *Synthesis of a novel dinuclear ruthenium polypyridine dye for dye-sensitized solar cells application*, Polyhedron, 2014, **67**, 381-387.

A list below presents other publications of the author.

- M. Zalas, B. Gierczyk, A. Bossi, P. R. Mussini, M. Klein, R. Pankiewicz, M. Makowska-Janusik, Ł. Popenda and W. Stampor, *The influence of anchoring group position in ruthenium dye molecule on performance of dye-sensitized solar cells*, Dyes and Pigments, 2018, **150**, 335-346.
- M. Szkoda, K. Trzciński, M. Klein, K. Siuzdak and A. Lisowska-Oleksiak, *The influence of photointercalaction and photochromism effects on the photocatalytic properties of electrochemically obtained maze-like MoO_3 microstructures*, Separation and Purification Technology, 2018, **197**, 382-387.
- A. Zielińska-Jurek, M. Klein and J. Hupka, *Enhanced visible light photocatalytic activity of Pt/I-TiO_2 in a slurry system and supported on glass packing* Separation and Purification Technology, 2017, **189**, 246-252.
- M. Klein, M. Szkoda, M. Sawczak, A. Cenian, A. Lisowska-Oleksiak and K. Siuzdak, *Flexible dye-sensitized solar cells based on Ti/TiO_2 nanotubes photoanode and Pt-free and TCO-free counter electrode system*, Solid State Ionics, 2017, **302**, 192-196.
- K. Siuzdak, M. Klein, M. Sawczak, G. Wróblewski, M. Słoma, M. Jakubowska and A. Cenian, *Spray-deposited carbon-nanotube counter-electrodes for dye-sensitized solar cells*, Physica Status Solidi (A), 2016, **213**, 1157-1164.
- K. Siuzdak, M. Sawczak, M. Klein, G. Nowaczyk, S. Jurga and A. Cenian, *Preparation of platinum modified titanium dioxide nanoparticles with the use of laser ablation in water*, Physical Chemistry Chemical Physics, 2014, **16**, 15199-15206.

- M. Zalas and M. Klein, *The influence of titania electrode modification with lanthanide ions containing thin layer on the performance of dye-sensitized solar cells*, International Journal of Photoenergy, 2012, **2012**, 927407.

- M. Klein, K. Łapiński, K. Siuzdak and A. Cenian, *Fundamentals of solar energy*, In: Geothermal, Wind and Solar Energy Applications in Agriculture and Aquaculture, CRC Press, 2017.

- K. Żelechowska and M. Klein, *Fotokatalityczne właściwości TiO_2*, In: Nanotechnologia w praktyce, Wydawnictwo Naukowe PWN, 2016.

2 Electronically excited states in molecular systems

2.1 Electronic structure of molecules

Electronic structure of molecules as well as changes in this structure due to absorption of electromagnetic radiation can be explained on the basis of the molecular orbital (MO) theory. Molecular orbitals are formed as linear combinations of the valence shell atomic orbitals. Therefore, the interaction of two atomic orbitals, described by the wavefunctions ϕ_A and ϕ_B, gives rise to two molecular orbitals of the form:

$$\psi_1 = \phi_A + \phi_B \tag{2.1}$$

$$\psi_2 = \phi_A - \phi_B. \tag{2.2}$$

The ψ_1 molecular orbital is bonding (i.e. more stable, of lower energy than the initial atomic orbitals) while the ψ_2 is antibonding (i.e. of higher energy than the initial atomic orbitals) - Fig. 2.1.

Three types of molecular orbitals can be distinguished: n, π and σ. σ bonding and $\sigma^\star$ antibonding molecular orbitals are completely symmetrical about the internuclear axis and are formed by head-on overlapping of two atomic orbitals (ϕ_A and ϕ_B). π bonding and $\pi^\star$ antibonding molecular orbitals result from side-by-side overlap of two parallel p-orbitals. Nonbonding

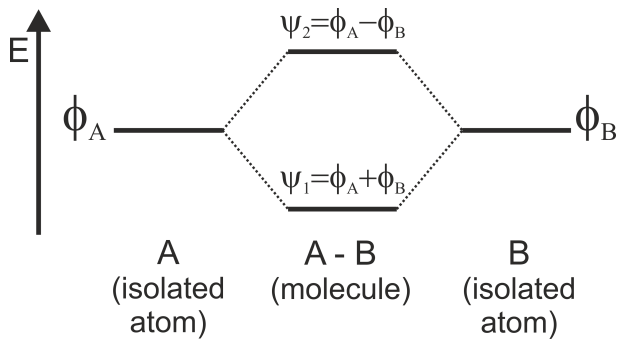

Figure 2.1. Interaction of two identical atomic orbitals

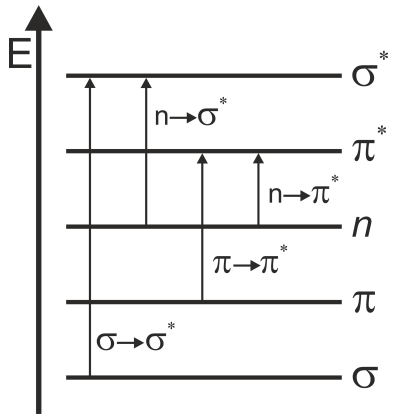

Figure 2.2. Electronic transitions within an organic molecule due to its excitation

molecular orbitals (n) contain lone pairs of electrons localized on one atom, that are neither bonding nor antibonding [6].

Electronic excitation of a molecule occurs when the absorption of electromagnetic radiation leads to an electron transfer from the occupied molecular orbital to the unoccupied molecular orbital of higher energy. These transitions are usually marked as follows: $\sigma \to \sigma^\star$, $\pi \to \pi^\star$, $n \to \pi^\star$, $n \to \sigma^\star$ (Fig. 2.2).

One of the examples of conjugated organic systems is benzene, whose molecular orbital model is shown in Fig. 2.3. Benzene is an archetypical aromatic compound composed of six unhybridized $2p$ orbitals of carbon (C) which are perpendicular to the ring plane. C atoms are regarded as $sp2$ hybridized. As a result of the combination of these six parallel $2p$ atomic orbitals a set of six π molecular orbitals is obtained (Fig. 2.4). Three of them are π-bonding MOs, while the other three are $\pi^\star$-antibonding MOs [7]. In the ground state of an organic system orbitals are filled in the order of increasing energy according to the Pauli exclusion principle: no more than two electrons may occupy any given orbital, and if two do occupy one orbital, then their spins must be paired [8]. Thus, in benzene all six electrons of the π system occupy bonding molecular orbitals.

Photochemistry and photophysics of octahedral transition-metal complexes is a bit more complicated. As a representative example the $Ru(bpy)_3^{2+}$ (bpy=2,2-bipyridine) is discussed. The electron configuration of ruthenium (Ru) atom is $4d^7 5s^1$. Ru(II) occurring in bipyridine complexes as an ion Ru^{2+} is a d^6 system. In isolated atoms five d-orbitals are degenerate, while in complexes these orbitals are split into three t_{2g} (nonbonding) and two $e_g^\star$ (antibonding) molecular orbitals (Fig. 2.5) [9]. The breaking of orbital degeneracy is related to the electrostatic interactions between the ligands

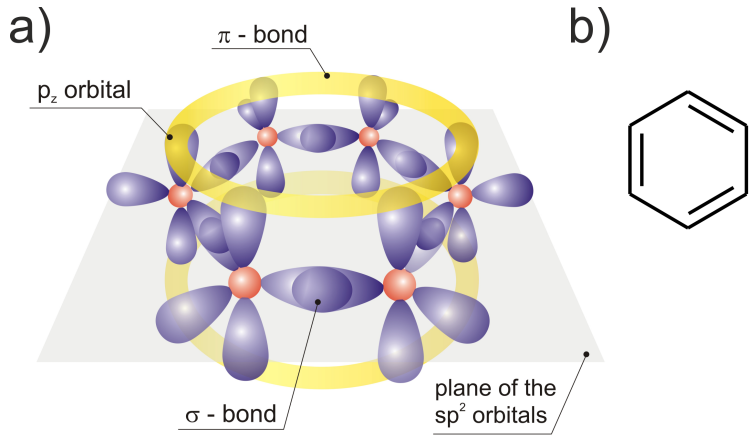

Figure 2.3. Molecular orbitals (a) and chemical structure (b) of the benzene molecule

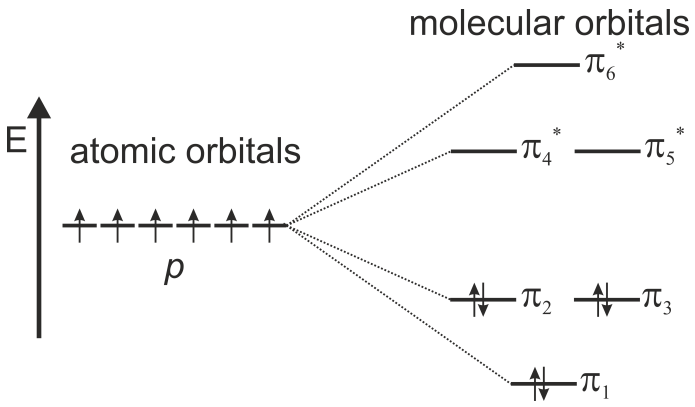

Figure 2.4. Benzene electronic energy levels

and central metal ion. Energy difference between d-orbital sublevels is called crystal field splitting [10]. In the ground state of the $Ru(bpy)_3^{2+}$ complex the σ_L and π_L bonding MOs of ligands and t_{2g} metal-centered MO are completely filled. As in fully organic systems photoexcitation of such a complex in the simplest one-electron description means promotion of an electron from an occupied to a vacant molecular orbital. So in the case of the complex in question we can distinguish four basic electronic transitions:

- metal-centered (MC) transitions between the π_M (t_{2g}) and $\sigma_M^\star$ ($e_g^\star$) MOs,
- ligand-centered (LC) transitions between the π_L and $\pi_L^\star$ MOs,
- metal-to-ligand charge transfer ($MLCT$) transitions between the $\pi_M(t_{2g})$ and $\pi_L^\star$ MOs,

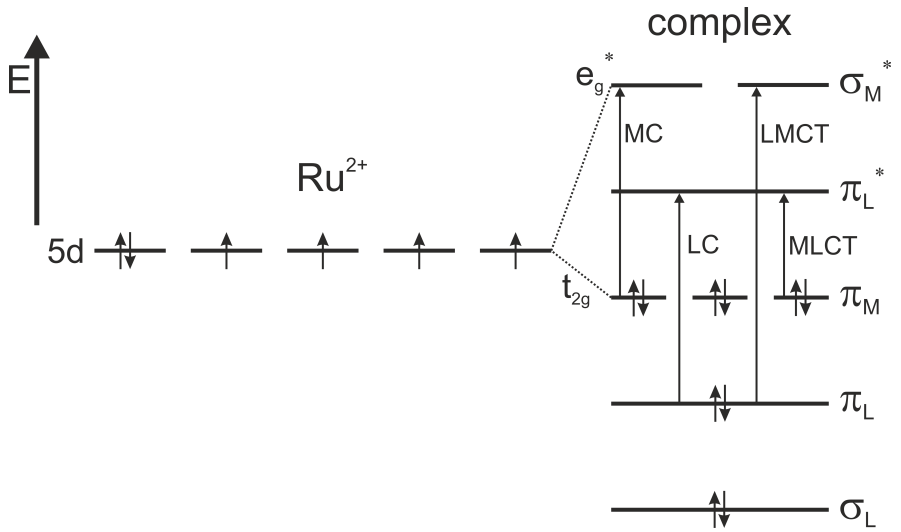

Figure 2.5. Electronic energy levels and charge transfer processes in the Ru(bpy)$_3^{2+}$ complex

- ligand-to-metal charge transfer ($LMCT$) transitions between the π_L and $\sigma_M^\star$ ($e_g^\star$) MOs.

2.2 Multiplicity of states, singlet-triplet splitting energy

The probability density of finding an electron at a particular point in space for a fixed position of the nuclei is expressed by $|\Psi|^2$ - the squared modulus of the electronic wavefunction (Ψ). Nevertheless, for a complete description of the molecule state in addition to electronic wavefunction the spin ($\vec{L}_s$) of the electron should also be considered. The spin angular momentum (spin) quantum number of an electron is $s = 1/2$. The total spin of a state is given by the sum of spins of all electrons in all orbitals. Let now consider two one-electron states denoted by α and β spin wavefunctions with $s = 1/2$, $m_s = 1/2$ and $s = 1/2$, $m_s = -1/2$, where m_s is a spin magnetic quantum number, that can be obtained upon excitation of a molecular system. In this case, unpaired electrons from π and $\pi^\star$ orbitals create a two-particle system

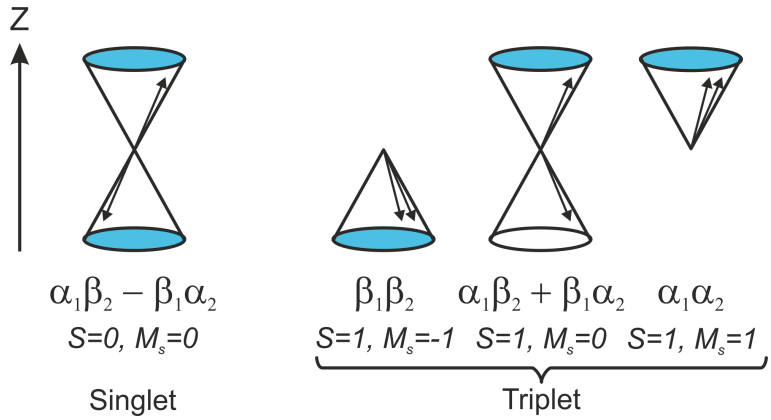

Figure 2.6. Relative orientations of two electron spins for a singlet and a triplet state illustrated in a form of a vector diagram

with spin wavefunction (Ψ_{spin}) that can be written as

$$\Psi_{spin,S} = \frac{1}{\sqrt{2}}(\alpha_1\beta_2 - \beta_1\alpha_2) \qquad for\ S = 0,\ M_s = 0; \tag{2.3}$$

$$\Psi_{spin,T0} = \frac{1}{\sqrt{2}}(\alpha_1\beta_2 + \beta_1\alpha_2) \qquad for\ S = 1,\ M_s = 0; \tag{2.4}$$

$$\Psi_{spin,T+} = \alpha_1\alpha_2 \qquad for\ S = 1,\ M_s = 1; \tag{2.5}$$

$$\Psi_{spin,T-} = \beta_1\beta_2 \qquad for\ S = 1,\ M_s = -1. \tag{2.6}$$

The paired-spin arrangement (antiparallel) with the total spin quantum number $S = 0$, described by antisymmetric spin wavefunction is called a singlet while the parallel spin arrangement with $S = 1$, described by symmetric spin wavefunction is called a triplet (for a vector representation see Fig. 2.6). Hence the total spin can be specified by its spin multiplicity: $2S + 1$. For $S = 0$ spin multiplicity $= 1$ (singlet), for $S = 1/2$ spin multiplicity $= 2$ (doublet), for $S = 1$ spin multiplicity $= 3$ (triplet), etc. With respect to the Pauli principle the total electronic wavefunction (represented by the product of space and spin wavefunctions) must be antisymmetric thus triplet states will have an antisymmetric spatial wavefunction while singlets a symmetric one [6].

In general, the energies of singlet and triplet states are different. The energy difference between these states, called singlet-triplet splitting energy ($\Delta E_{ST} = E_S - E_T$), depends on the spatial separation and of the extent overlap of the highest occupied molecular orbital (HOMO) and the lowest unoccupied molecular orbital (LUMO). Singlet and triplet energy levels (E_S

and E_T, respectively) are equal to

$$E_S = E_C + J_{ex}, \tag{2.7}$$
$$E_T = E_C - J_{ex}, \tag{2.8}$$

where

$$E_C = \iint |\Psi_H(\vec{r}_1)|^2 \frac{e^2}{4\pi\epsilon_0|\vec{r}_1 - \vec{r}_2|} |\Psi_L(\vec{r}_2)|^2 d^3\vec{r}_1 d^3\vec{r}_2, \tag{2.9}$$

and

$$J_{ex} = \iint \Psi_H^\star(\vec{r}_1)\Psi_L^\star(\vec{r}_2) \frac{e^2}{4\pi\epsilon_0|\vec{r}_1 - \vec{r}_2|} \Psi_H(\vec{r}_2)\Psi_L(\vec{r}_1) d^3\vec{r}_1 d^3\vec{r}_2. \tag{2.10}$$

E_C is the Coulomb integral and represents the Coulomb interaction between charge distributions of electrons in HOMO (the electronic wavefunction Ψ_H) and LUMO (the electronic wavefunction Ψ_L) orbitals, J_{ex} is known as the exchange integral and describes quantum mechanical correction to the E_C, e is the elementary charge, ϵ_0 is the vacuum permittivity and $|\vec{r}_1 - \vec{r}_2|$ denotes spatial separation of electrons [11].

It should be noted that J_{ex} integrals are usually positive, therefore, the energy of a triplet state is lower than the energy of a singlet one and their difference is equal to the double exchange integral

$$\Delta E_{ST} = E_S - E_T = 2J_{ex}. \tag{2.11}$$

2.3 Jabłoński diagram

Jabłoński diagram represents the electronic structure of a molecule with all physical processes involved in the interconversion of its states (Fig. 2.7) [6]. The ground state is denoted by S_0 while the excited singlet and triplet states are ranged and numbered in the order of increasing energy. These states are denoted by S_1, S_2... and T_1, T_2..., respectively. Each electronic energy level is composed of vibrational sublevels, while each of vibrational sublevels has a series of rotational energy quantum levels (not indicated in the diagram due to a very small energy gaps between them). The following processes are shown in the diagram: transitions associated with absorption of a photon, radiative decay processes, non-radiative decay processes and vibrational relaxation.

In the radiative transitions, the excited species goes from a higher excited state to a lower one with the emission of a photon. According to Kasha's rule

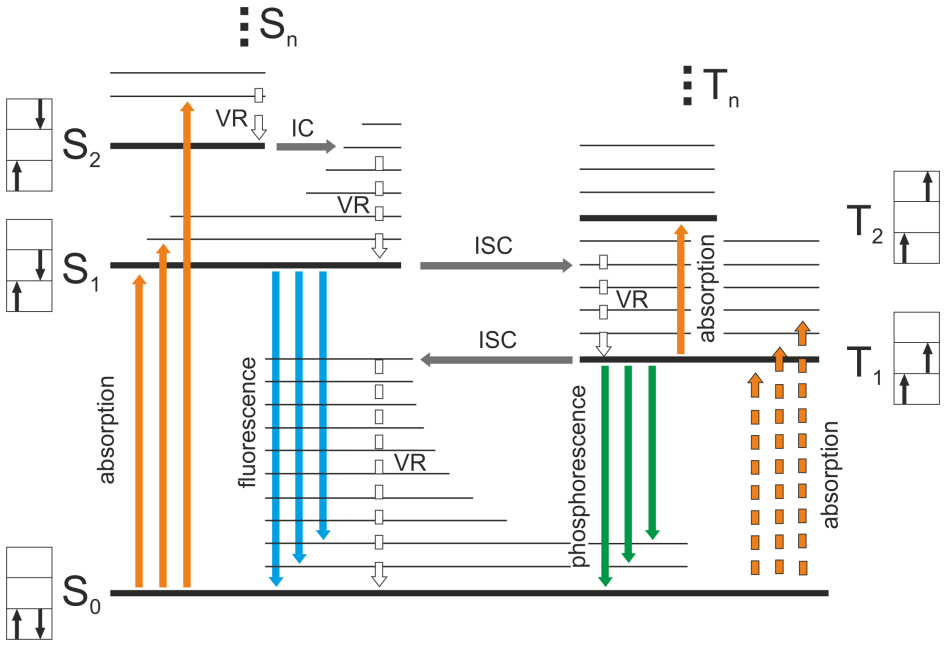

Figure 2.7. Jabłoński diagram for an organic molecule, illustrating excited-state photophysical processes. VR - vibrational relaxation, IC - internal conversion, ISC - intersystem crossing (after [12])

the emitting state is the lowest excited state of a given multiplicity. Three types of radiative transitions can be distinguished: fluorescence, phosphorescence and delayed fluorescence.

Fluorescence is the result of a radiative transition between states of the same multiplicity, $S_1 \rightarrow S_0$. This is a spin-allowed rapid process ($k_f \approx 10^8 - 10^9$ s^{-1}).

Phosphorescence is due to a radiative transition between states of different multiplicity, typically $T_1 \rightarrow S_0$. This process is spin-forbidden, so its rate constant is much lower ($k_p \approx 10^{-2} - 10^4$ s^{-1}) than that for fluorescence.

Delayed fluorescence, is associated with the $S_1 \rightarrow S_0$ radiative transition, but unlike direct (prompt) fluorescence, the singlet S_1 state arises here due to the thermal activation of a triplet T_1 state or due to the triplet-triplet annihilation, followed by a reverse intersystem crossing process. The delayed fluorescence lifetime is determined by the lifetime of a triplet state.

An excited species at the moment of its creation, besides the electronic energy, is endowed with excess vibrational (and rotational) energy. The loss of vibrational energy takes place as a result of collisions (in a solid state with the emission of phonons) wherein it is converted into kinetic energy distributed between molecules involved in the collisions. This process is called vibrational relaxation (VR).

Between isoenergetic (or degenerate) levels of different electronic states non-radiative (or radiationless) transitions occur. Thus, if the total energy of the system is preserved, no photon is emitted. Two kinds of such transitions can be distinguished:

- **internal conversion** (IC), a non-radiative transition between isoenergetic states of the same multiplicity,
- **intersystem crossing** (ISC), a radiationless transition between states of different multiplicity.

The intersystem crossing $S_1 \rightsquigarrow T_1$ or $S_1 \rightsquigarrow T_n$ are usually main formation pathways for triplet manifolds. However, the ISC is in general a spin-forbidden transition.

It should be noted that the intensities of electronic transitions are proportional to the square of the transition moment $\vec{\mu}_{if} = \langle \Psi_i | \hat{\vec{\mu}} | \Psi_f \rangle$, where Ψ_i and Ψ_f are the total wavefunctions (products of nuclear θ, spin ψ_S and electronic φ wavefunctions) of the initial and final states of the system, respectively, and $\hat{\vec{\mu}}$ is an electric dipole moment operator. Taking into account the Born-Oppenheimer approximation (electrons are thought of as moving in the potential field of the static nuclei) the $\vec{\mu}_{if}$ can be expressed by three terms: overlap integral of the wavefunctions for nuclear vibrations (Franck-Condon factor), the spin overlap integral and the electronic transition moment

$$\vec{\mu}_{if} = \int \theta_i \theta_f d\tau_N \cdot \int \psi_{Si} \psi_{Sf} d\tau_S \cdot \int \varphi_i \cdot \vec{\mu} \cdot \varphi_f d\tau_e, \tag{2.12}$$

where subscripts N, s and e refer to nuclear, electron spin and electron space coordinates; θ, ψ_S and φ stand for the nuclear, electron spin and electron space parts of the total wavefunction for i and f electronic states, respectively [6].

If any of the above integrals is zero then the transition moment equals zero as well, which means that the transition is forbidden (has a zero probability of occurrence). Therefore, the multiplicity change during the $S \rightsquigarrow T$ transitions leads to zeroing of the spin integral. The fact that these transitions may occur at all is due to spin-orbit coupling (for simplicity vibronic coupling is neglected here), which is basically an interaction of spin magnetic moment $\vec{\mu}_s$ with the magnetic field $\vec{B}_l$ associated with the electron orbital motion [11]. The term

$$\hat{H}_{SO} = \xi \vec{L}_\ell \cdot \vec{L}_s \tag{2.13}$$

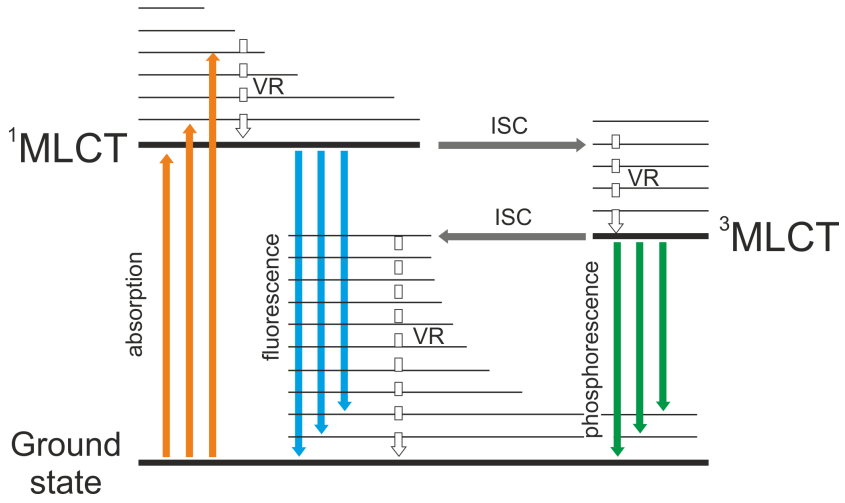

Figure 2.8. Jabłoński diagram for an organic complex with a heavy atom in its structure. VR - vibrational relaxation, ISC - intersystem crossing

determines spin-orbit coupling energy, where $\vec{L}_\ell$ is the orbital angular momentum operator and $\vec{L}_s$ is the spin angular momentum operator. This term is a part of Hamiltonian operator $\hat{H}$ that describes the total energy of the system. The degree of coupling (for hydrogen-like atoms) is determined by the constant of spin-orbit coupling

$$\xi = \frac{Z^4 e^2}{8\pi\epsilon_0 m_e^2 c^2 a_0^3}, \tag{2.14}$$

where Z is the atomic number, m_e denotes the mass of an electron, a_0 is the Bohr radius and c stands for the speed of light [13]. Hence, the value of ξ depends on the atomic number Z and it is proportional to the Z^4. The effect of spin-orbit coupling is a small amount of singlet character mixed into the triplet states and *vice-versa*, so that pure singlet and triplet states no longer exist. The presence of so-called heavy atoms such as ruthenium (Ru) in the parent molecule (internal heavy atom effect) or e.g. bromine (Br) in the solvent (external heavy atom effect) increases the ISC probability by increasing the magnitude of the spin-orbit coupling [14].

For organic complexes with a heavy atom in their structure the Jabłoński diagram should be changed taking into account the $MLCT$ states (Fig. 2.8) [9]. Then the excited states can have both singlet and triplet multiplicity. Moreover, strong spin-orbit coupling associated with the Ru heavy atom induces singlet-triplet mixing of $MLCT$ states. Hence, intersystem crossing between ^1MLCT and ^3MLCT becomes spin allowed [15].

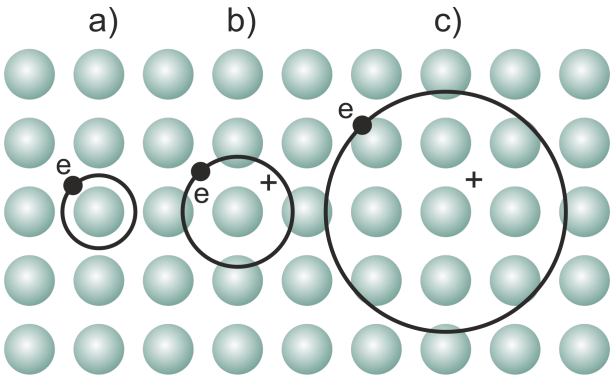

Figure 2.9. A diagram illustrating Frenkel exciton (a), charge-transfer exciton (b) and Wannier-Mott exciton (c)

2.4 Neutral and ionic excited states in organic solids

Molecular solids bonded by the van der Waals forces retain the properties of individual molecules to a large extent [16]. Excited electronic states in organic solids (or molecular crystals) can be classified as neutral or ionized. The creation of ionized states proceeds mainly *via* neutral states [17].

Neutral excited states in a molecular crystal can be described in terms of molecular exciton theory developed by Davydov [18]. An exciton is formed by two correlated charges, an electron and a hole, attracted by the Coulomb force. Thus, excitons are electrically neutral mobile quasi-particles. Three types of excitons can be distinguished: Frenkel, Wannier-Mott or a charge-transfer (CT) exciton (cf. Fig. 2.9) [16]. A strongly correlated electron-hole pair located on the same molecule, with a separation distance between an electron and a hole (exciton radius) smaller than the lattice constant is called a Frenkel exciton. A weakly bound, large radius (more than an order of magnitude larger then the lattice parameters) electron-hole pair is called a Wannier-Mott exciton. Such an exciton is the most common in inorganic systems, in which the interaction energies are great and dielectric constants are high. An electron-hole pair localized on adjacent molecules with the radius comparable to the lattice constant is referred to as charge-transfer exciton. In molecular crystals with unit cells composed of two non-translationally equivalent molecules Frenkel excitons should experience a splitting of electronic levels. In general, this so called Davydov splitting is a splitting of each molecular level to a maximum of n sublevels, resulting from the resonant interaction between n non-translationally equivalent molecules in the excited state.

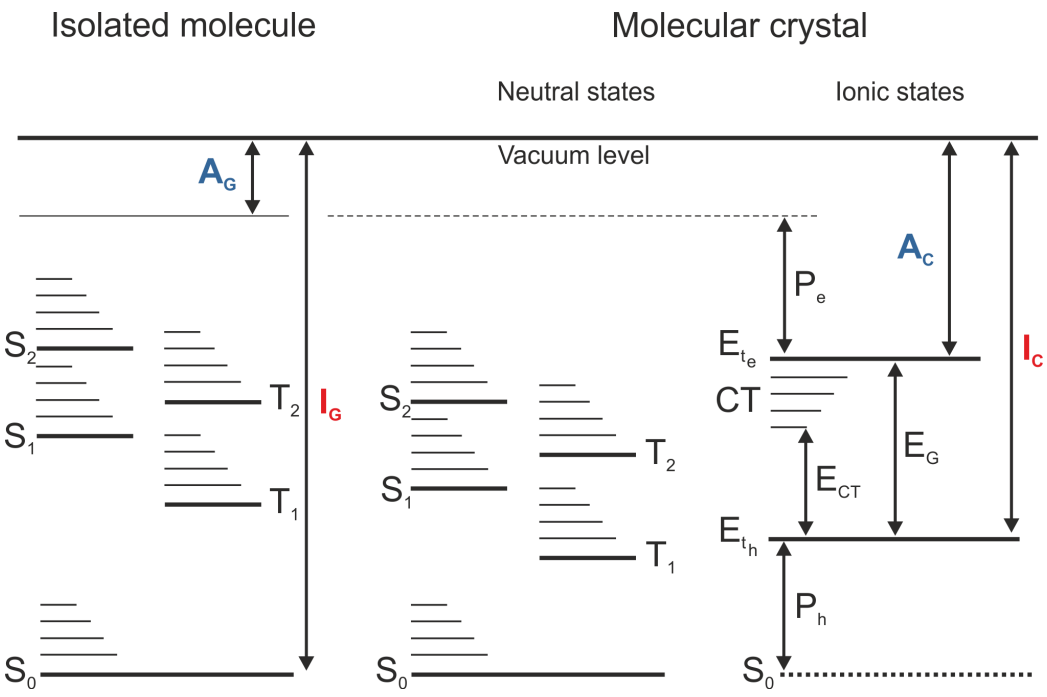

Figure 2.10. Energy level diagram of an isolated molecule and an ideal molecular crystal. Symbols are explained in the text

The excitation energy of excitons with wavevector $\vec{k}$ can be expressed as

$$E_n(\vec{k}) = \Delta\epsilon + D + \epsilon_n(\vec{k}), \quad n = 1, 2, 3... \tag{2.15}$$

where $\Delta\epsilon$ is the excitation energy of an isolated molecule, D is the change in energy due to dispersion interaction of the excited molecule with the crystalline environment in the ground state, $\epsilon_n(\vec{k})$ is a term determining the resonance energy of the exciton in the n^{th} band (resonance interaction between molecules) [17]. Exciton bands in organic solids are usually very narrow, about 0.01 to 0.04 eV wide for a singlet exciton and on the order of 0.001 eV for a triplet exciton. Therefore, at room temperature, where considerable interaction between the exciton and lattice vibrations occurs, exciton transport is assigned to incoherent diffusion of localized excitons by site-to-site hopping in the lattice rather than coherent wave-like motion [16, 17].

When molecules are closely packed, as in a solid, interactions between them, associated with electronic polarization effects, modifies the positions of their energy levels (Fig. 2.10) [17]. Therefore, the ionization energy I_C of a crystal is lower than the corresponding ionization energy I_G of an isolated molecule (or in a gas phase). This energy difference, expressed as

$$P_h = I_G - I_C, \tag{2.16}$$

is called the hole polarization energy. Moreover, intermolecular interactions are also responsible for the increase in the electron affinity A_C compared to the electron affinity of an isolated molecules A_G. This energy shift equal to

$$P_e = A_C - A_G \tag{2.17}$$

is called the electron polarization energy. E_{t_e} energy level corresponds to the narrow (due to weak intermolecular interactions) conduction band responsible for transport of excessive electron within an organic crystal while the energy level E_{t_h} to the relevant band transporting excessive hole. The separation energy of these levels is called the energy gap E_G and determines the energy that the electron has to gain in order to create a pair of free charge carriers. Charge-transfer states are located below the E_{t_e} level and their energy E_{CT} is lower than the width of the energy gap. E_{t_e} and E_{t_h} levels are usually referred to as conduction and valence band, respectively, and correspond to the LUMO and HOMO of an isolated molecule. It should be noted that in organic electronic devices usually the HOMO and LUMO names are identified with the designation of valence and conduction bands (and in principle with the I_C and A_C) while they stand for a one-electron orbitals for a single molecule. Thus, the energy difference between HOMO and LUMO is, in fact, only a very rough approximation for the energy gap between the E_{t_e} and E_{t_h} levels [19]. In order to determine the energies of I_C and A_C photoelectron spectroscopic methods: UV photoelectron spectroscopy - UPS, and inverse photoelectron spectroscopy - IPES, should be employed [20].

Strong charge carrier-lattice interaction that occurs in organic solids (especially in conjugated polymers) leads to the formation of a quasi-particle called polaron. It is, in fact, a self-localized composite state containing the charge surrounded by a cloud of phonons. A polaron possesses charge $\pm e$ and spin $\pm\frac{1}{2}$ [19].

3 Fundamentals of dye-sensitized and organic solar cells

3.1 Dye-sensitized solar cells (DSSCs)

Dye-sensitized solar cells (DSSC), also known as photoelectrochemical cells, are devices that convert solar energy to electricity using low-cost and non-toxic materials [21, 22]. First attempts to develop dye-sensitized photoelectrochemical cells have been made in the 60s of the 20th century but the conversion yields from solar energy to electricity were well below 1% [23, 24]. Nevertheless, it was not until the breakthrough work of O'Regan and Grätzel, in which a mesoporous semiconductor electrode with a high internal surface area was applied, that the way towards the rapid development of DSSCs has been paved [21]. Because of recent reports on the remarkable photoconversion efficiencies (PCE) of DSSCs of over 14% thanks to molecular engineering of organic sensitizers and over 21% for a panchromatic dye-sensitized cell in conjunction with a perovskite cell utilizing a system of spectral splitting, this technology is becoming a credible alternative for the most popular first generation silicon-based inorganic solar cells [25, 26]. The transparent photoanode in the form of a mesoporous layer of a nanocrystalline wide-band gap semiconductor (mostly TiO_2) with adsorbed monolayer of dye molecules deposited onto transparent conductive oxide (TCO) glass substrate and the counter electrode made of TCO glass coated with a thin catalytic layer (usually platinum, Pt), between which there is a liquid electrolyte containing mostly I^-/I_3^- redox couple, form a typical DSSC (Fig. 3.1) [21, 27]. Indium-tin oxide (In_2O_3:Sn, ITO) TCO is the most common substrate used in many optoelectronic devices, nevertheless due to its poor thermal stability at higher temperatures (of over $400°C$) fluorine-doped tin oxide (SnO_2:F, FTO) is usually used as the TCO substrate for DSSCs.

The operational mechanism is as follows: incident solar radiation is absorbed by a dye molecule which is excited from the ground state D_0 to the excited state $D^\star$

$$D_0 + h\nu \rightarrow D^\star \quad (photoexcitation). \tag{3.1}$$

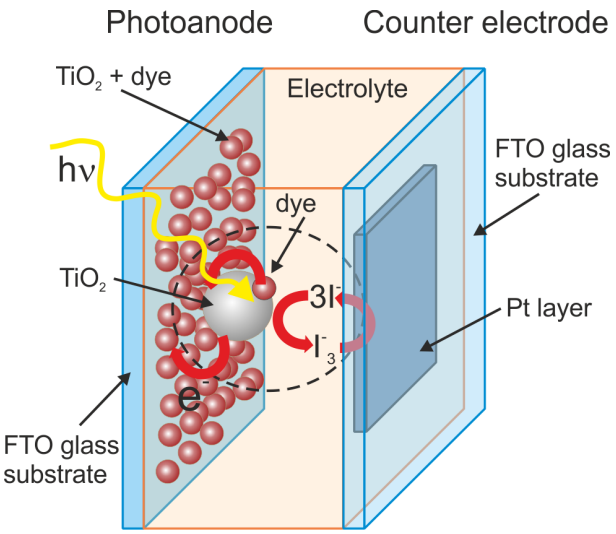

Figure 3.1. Schematic illustration of a dye-sensitized solar cell

This step is followed by an electron transfer from $D^{\star}$ to the conduction band of the semiconductor leaving the dye molecule in an oxidized state D^{+}

$$D^{\star} \rightarrow D^{+} + e^{-} \quad (\mathrm{TiO2}\ charge\ injection). \tag{3.2}$$

Then, injected electrons percolate through the semiconductor layer up to TCO coated glass, and next, through external load to the counter electrode. The dye is restored to its ground state by electron transfer from the electrolyte

$$2D^{+} + 3\mathrm{I}^{-} \rightarrow 2D_0 + \mathrm{I}_3^{-} \quad (regeneration\ of\ D_0). \tag{3.3}$$

Simultaneously, the I_3^{-} ions formed by oxidation of I^{-} diffuse through the electrolyte to the cathode where the regenerative cycle is completed by electron transfer to reduce I_3^{-} to I^{-}

$$\mathrm{I}_3^{-} + 2e^{-}(\mathrm{Pt}) \rightarrow 3\mathrm{I}^{-} \quad (regeneration\ of\ \mathrm{I}^{-}). \tag{3.4}$$

The DSSC operation is associated with an appropriate adjustment of energy levels of each component, namely, the excited state of the dye molecule has to be located above the conduction band of the semiconductor and the energy level of the redox pair should lie above the ground state of the dye molecule (Fig. 3.2). This means that there is no energy barrier on the electron path through the entire cell. The photocurrent generated in a DSSC is basically determined by the energy difference between the HOMO and the LUMO of the photosensitizer - the smaller the HOMO-LUMO energy gap, the larger

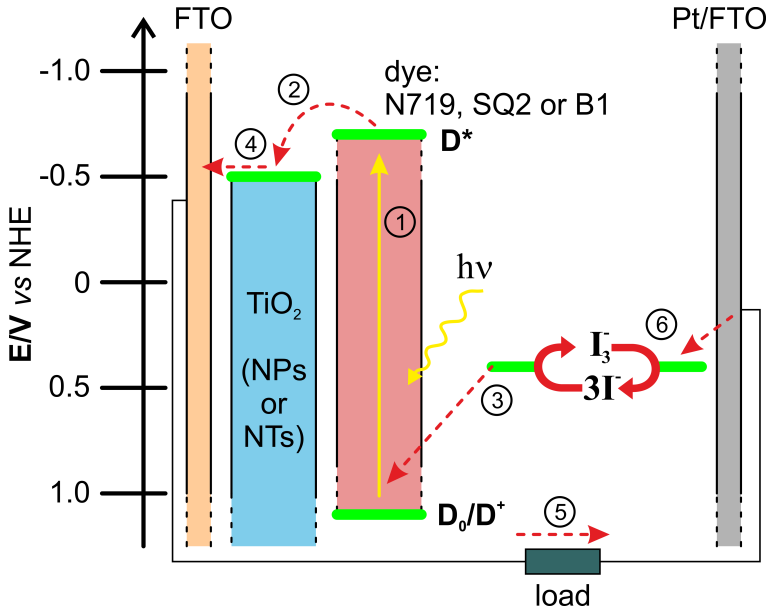

Figure 3.2. Energy level diagram and principles of operation of a DSSC

the photocurrent. On the other hand, the energy gap between the Fermi level of the semiconductor electrode and the redox potential of the mediator in the electrolyte specifies the voltage [4, 27, 28].

The process of electron transfer in photoelectrochemical cells is based on a series of chemical reactions and physical phenomena occurring in individual elements of the cell as well as at the interface of relevant materials. The rate constants of these processes and the properties of the materials used have a very large impact on the final cell performance. The processes leading to the photocurrent generation (indicated by green arrows) occur much faster than the limiting processes, e.g. recombination or relaxation processes (indicated by red arrows) (Fig. 3.3). The slowest process is the electron diffusion through the semiconductor layer [4, 22, 27, 28].

3.2 Organic solar cells

The photovoltaic effect in organic solids was observed for the first time in anthracene crystals in 1959 by Kallmann and Pope [29]. That was the beginning of organic photovoltaic (OPV) devices based on a single active layer sandwiched between two metal electrodes with different work functions [30]. In order to provide sufficient light penetration one of the electrodes has to be transparent (or semi-transparent). For this purpose the ITO glass substrate is usually employed while the other electrode (a non-transparent

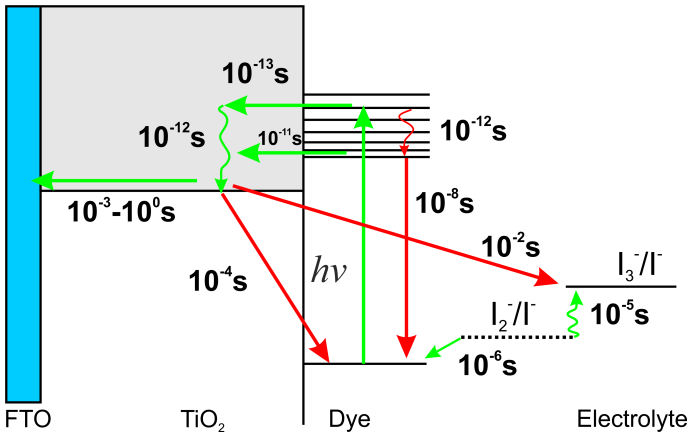

Figure 3.3. Kinetic of processes and their time constants under working conditions in a Ru-based DSSC with I^-/I_3^- electrolyte (after [27])

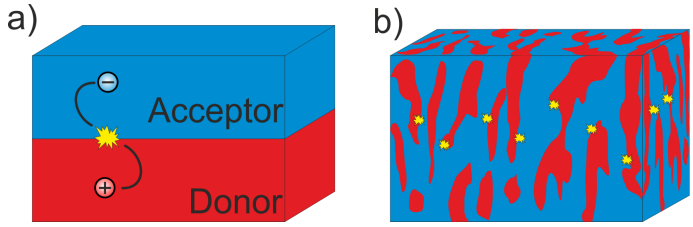

Figure 3.4. Schematic diagram of a planar (a) and bulk-heterojunction (b) solar cell

one) is a metal layer (usually Al, Ag, LiF+Al). In single layer organic solar cells incident solar radiation is absorbed by an organic layer. Afterwards, exciton generation occurs followed by its dissociation at the organic material/electrode interface (junction). To provide efficient exciton dissociation as well as charge carrier collection, one of the junctions has to constitute a rectifying (Schottky) contact while the other one an ohmic contact, respectively. The performance of these devices was generally poor (due to a short exciton diffusion length, L_D) until the breakthrough work of Tang [31]. In 1986 Tang introduced a concept of a bilayer donor/acceptor solar cell based on a planar-heterojunction (PHJ) of two organic materials: a copper phthalocyanine and a perylene derivative, with a photoconversion efficiency of 1% (Fig. 3.4a). Another milestone in the field of OPVs was the discovery of photoinduced ultrafast electron transfer from a conducting polymer to a buckminsterfullerene reported by Sariciftci *et al.* in 1992 [32]. Due to a novel concept of an interpenetrating polymer:fullerene (donor:acceptor) blend, the so called bulk-heterojunction (BHJ) solar cell, a significant improvement in the efficiency has been achieved (Fig. 3.4b).

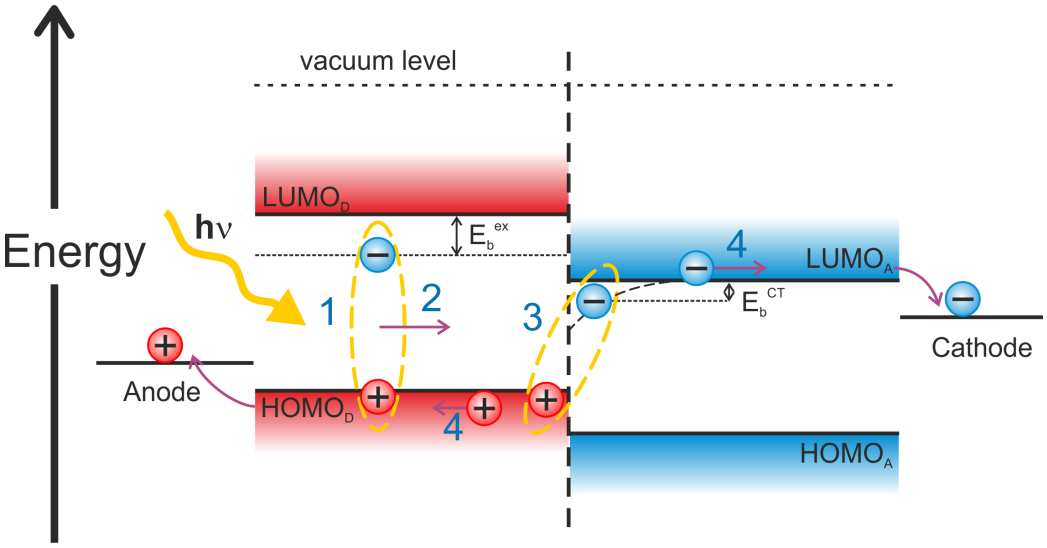

Figure 3.5. Schematic structure with indicated energy levels and operating mechanism of an OPV. E_b^{ex} denotes an exciton binding energy while E_b^{CT} denotes a CT state binding energy

The photocurrent generation mechanism for bilayer organic solar cells consists of four fundamental steps. First, upon absorption of light, an electron in the donor (or alternatively in the acceptor) undergoes photoinduced excitation from the HOMO to the LUMO of the organic material, forming a Frenkel exciton. Second, before the exciton decays, it moves to the donor-acceptor (D-A) interface within the diffusion length. Third, an exciton at a D-A interface undergoes charge-transfer process to form a *CT* exciton (electron-hole pair, $e-h$ pair), where the hole and electron are localized at the adjacent donor and acceptor molecules, respectively, held together through coulombic attraction. Fourth, the *CT* exciton dissociates into free holes and electrons with the assistance of built-in electric field. Free charge carriers are then transported to the respective electrodes: a hole through the donor and an electron through the acceptor phases [33]. The maximum value of the open circuit voltage, V_{OC}, can by roughly determined by the difference between the energy levels of HOMO of the donor and the LUMO of the acceptor [19]:

$$eV_{OC} = LUMO_A - HOMO_D. \tag{3.5}$$

In the bilayer architecture of a solar cell organic materials should form ohmic contacts with electrodes to ensure efficient charge collection.

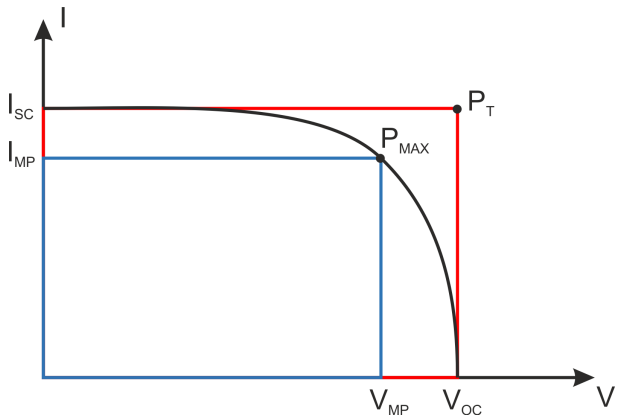

Figure 3.6. Typical I-V curve with a graphical representation of the fill factor

3.3 Performance parameters of solar cells

In order to characterize the solar cell and to estimate its electrical parameters the current-voltage (I-V) characteristics under illumination should be determined. The I-V curve is a graphical representation of the current and voltage changes as different loads are applied. There are characteristic points on the I-V curve, these are: the short-circuit current, I_{SC}, the open-circuit voltage, V_{OC}, and the maximum power point, P_{MAX}. I_{SC} is the value of the current intensity under short-circuit conditions i.e. when the voltage equals zero. V_{OC} is the value of voltage under open-circuit conditions i.e. when the current does not flow. The power P produced by a solar cell can be easily calculated from the following formula

$$P = IV, \tag{3.6}$$

where I and V are the current and the voltage between the terminals of a cell. Maximum power point is such a point on the I-V curve for which the power produced by the cell is the greatest (marked as P_{MAX}). At this point the voltage and current are denoted by V_{MP} and I_{MP}, respectively. The basic quantity that determines the solar cell performance is the solar-to-electric power conversion efficiency η (PCE, photoconversion efficiency). This is the ratio of the electrical power output measured at the maximum power point of the solar cell P_{MAX} to the solar power input $P_{IN} = I_{rad}A$ which is the product of irradiance, I_{rad}, and the area of a solar cell A,

$$\eta = \frac{P_{MAX}}{P_{IN}} = \frac{I_{MP}V_{MP}}{I_{rad}A}. \tag{3.7}$$

Another coefficient defining a quality of the solar cell is the fill factor (FF). It is calculated as a ratio of the maximum power of a solar cell and the

theoretical power, P_T, that would be generated if the cell could deliver the maximum current equal to I_{SC} at the voltage equal to V_{OC}:

$$FF = \frac{P_{MAX}}{P_T} = \frac{I_{MP}V_{MP}}{I_{SC}V_{OC}}. \tag{3.8}$$

Fill factor can also be estimated from the I-V curve by comparing the area of the smaller (blue) and bigger (red) rectangles (Fig. 3.6). Knowing this parameter it is possible to calculate the solar-to-electric power conversion efficiency from the following relation

$$\eta = \frac{I_{SC}V_{OC}FF}{I_{rad}A}. \tag{3.9}$$

To compare the performance of various solar cells measured in different laboratories equipped with different solar simulators, the standard test conditions (STC) were introduced. The STC conditions mean the cell temperature of $25°C$, AM1.5 spectrum of light and irradiance of 1000 Wm^{-2}, where air mass (AM) refers to the distance travelled by light in the Earth's atmosphere normalized to the shortest possible path length (that is, when the Sun is in zenith). The value "AM1.5", 1.5 of the atmosphere thickness, corresponds to a solar zenith angle of $\Theta = 48.2°$ [4, 34].

4 Magnetic field effects (MFEs)

4.1 Types of magnetic field effects

4.1.1 Magnetic properties of electron and nuclear spins

Orbital angular momentum and orbital magnetic moment

In the Bohr model an electron of mass m_e and charge $-e$ moves around a nucleus in a circular orbit with velocity $\vec{v}$ and position vector $\vec{r}$ relative to the nucleus. Accordingly, it possesses a non-zero orbital angular momentum $\vec{L}_\ell = \vec{r} \times \vec{p}$, where $\vec{p} = m_e\vec{v}$ is its momentum (Fig. 4.1). In terms of quantum mechanics the possible values of orbital angular momentum of an electron in an atom are

$$|\vec{L}_\ell| = \sqrt{\ell(\ell+1)}\hbar, \tag{4.1}$$

where ℓ is the orbital quantum number ($\ell = 0, 1, 2, 3, ..., n-1$), $\hbar$ is the reduced Planck constant while n is the principal quantum number ($n = 1, 2, 3, ...$). Such a system might be represented by a single circular conducting loop carrying a current. Therefore, the movement of an electron in its orbit induces formation of orbital magnetic dipole moment $\vec{\mu}_\ell$ that is oppositely directed to the vector of orbital angular momentum $\vec{L}_\ell$ and given by

$$\vec{\mu}_\ell = -\frac{e}{2m_e}\vec{L}_\ell. \tag{4.2}$$

The magnitude of the component of $\vec{\mu}_\ell$ in a given direction, the z-component, is

$$\mu_{\ell z} = -g_\ell \frac{e}{2m_e} L_{\ell z} = -\frac{e}{2m_e} g_\ell m_\ell \hbar = -g_\ell \mu_B m_\ell, \tag{4.3}$$

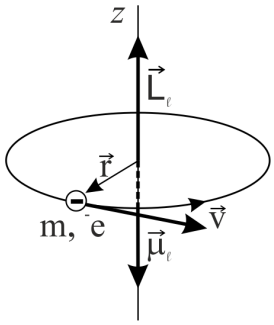

Figure 4.1. Orbital magnetic moment ($\vec{\mu}_\ell$) induced by the circulating electron

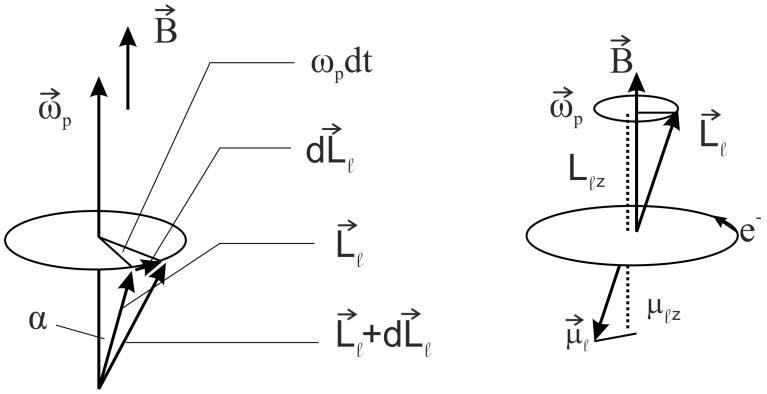

Figure 4.2. Precession of the orbital angular momentum in the external magnetic field

where m_ℓ is the magnetic orbital quantum number ($m_\ell = 0, \pm1, \pm2, \pm3, ..., \pm\ell$), $\mu_B = \frac{e\hbar}{2m_e}$ stands for the Bohr magneton, and $g_\ell = 1$ is a dimensionless gyromagnetic factor (g-factor), that is a measure of the ratio of the magnetic moment to the angular momentum.

The external magnetic field $\vec{B}$, directed along z axis causes rotation of $\vec{\mu_\ell}$ about the direction of the field called a precession (Fig. 4.2). The precession frequency, called the Larmor frequency, is

$$\omega_p = \frac{\mu_\ell B \sin\alpha}{|\vec{L}_\ell| \sin\alpha} = \frac{g_\ell \mu_B}{\hbar} B. \tag{4.4}$$

Spin angular momentum and spin magnetic moment

The experiments carried out by Stern and Gerlach showed that electrons possess an intrinsic magnetic moment which is independent of the magnetic moment produced by orbital motion. This magnetic moment that does not

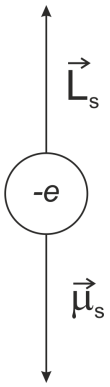

Figure 4.3. Spin and magnetic moment of an electron

have a clear analogy in classical mechanics is due to an intrinsic angular momentum called spin angular momentum or spin (Fig. 4.3):

$$|\vec{L}_s| = \sqrt{s(s+1)}\hbar, \tag{4.5}$$

where s is a spin quantum number (for a single electron $s = \frac{1}{2}$). Thus, this intrinsic magnetic moment called spin magnetic moment is given by

$$\vec{\mu}_s = -g_s \frac{e}{2m} \vec{L}_s, \tag{4.6}$$

where $g_s = 2$ is a g-factor for a free electron. The value of the spin magnetic moment in the z direction is

$$\mu_{sz} = -g_s \frac{e}{2m} m_s \hbar = -g_s m_s \mu_B, \tag{4.7}$$

where m_s is the magnetic spin quantum number (for a single electron $m_s = \pm\frac{1}{2}$).

In the external magnetic field $\vec{B}$ directed along z axis, the spin angular momentum, precesses like the orbital angular momentum, having two possible orientations in space defined by the spin magnetic quantum number m_s.

Total angular momentum

The vector sum of the orbital angular momentum $\vec{L}_\ell$ and spin angular momentum $\vec{L}_s$ called total angular momentum $\vec{L}_J$ is given by

$$\vec{L}_J = \vec{L}_\ell + \vec{L}_s, \tag{4.8}$$

where $|\vec{L}_\jmath| = \sqrt{\jmath(\jmath+1)}\hbar$, $|\vec{L}_\ell| = \sqrt{\ell(\ell+1)}\hbar$, $|\vec{L}_s| = \sqrt{s(s+1)}\hbar$. $\vec{L}_\ell$ and $\vec{L}_s$ vectors precess around the $\vec{L}_\jmath$ vector (Fig. 4.4). $\jmath$ stands here for the total angular momentum quantum number ($\jmath = \ell - \frac{1}{2}, \ell + \frac{1}{2}$ for $\ell > 0$ or $\jmath = \frac{1}{2}$ for $\ell = 0$).

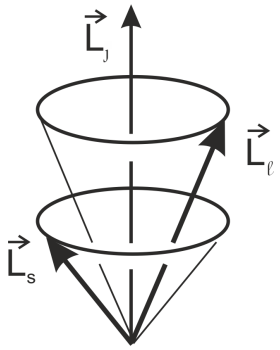

Figure 4.4. Precession of the spin ($\vec{L}_s$) and orbital ($\vec{L}_\ell$) angular momentum around the total angular momentum vector ($\vec{L}_\jmath$)

Total magnetic moment

The total magnetic dipole moment $\vec{\mu}_\jmath$ of an electron is associated with the total angular momentum $\vec{L}_\jmath$. The g-factors for relevant spin and orbital moments are different, hence the directions of the $\vec{L}_\jmath$ and $\vec{\mu}_\jmath$ vectors are different as well (Fig. 4.5). As a result the instantaneous magnetic moment $\vec{\mu}_\jmath$ precesses around the vector $\vec{L}_\jmath$. Thus we may observe only the projection of $\vec{\mu}_\jmath$ on $\vec{L}_\jmath$ given by

$$|(\vec{\mu}_\jmath)_\jmath| = g_\jmath\sqrt{\jmath(\jmath+1)}\mu_B, \tag{4.9}$$

where $g_\jmath$ is the Lande factor expressed as follows

$$g_\jmath = 1 + \frac{\jmath(\jmath+1) + s(s+1) - \ell(\ell+1)}{2\jmath(\jmath+1)}. \tag{4.10}$$

Fine and hyperfine interactions

The interaction between magnetic dipole moment of a nucleus with the magnetic field of its surrounding electron shells is referred to as *hyperfine interaction*. In general, two kinds of hyperfine interaction can be distinguished: anisotropic dipole-dipole through-space interaction and isotropic

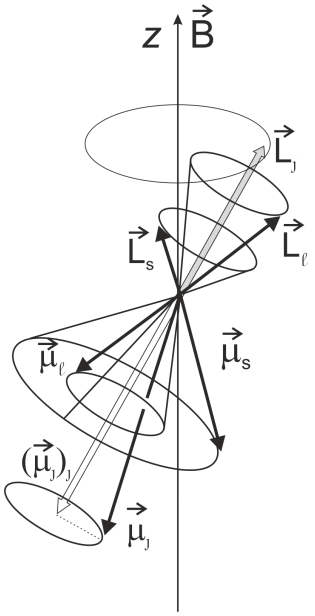

Figure 4.5. The relation between the total angular momentum $\vec{L}_J$, the total magnetic moment $\vec{\mu}_J$ and their orientation with respect to the magnetic field $\vec{B}$ directed along z axis

contact (Fermi type) through-bond interaction [35]. In the second type the hyperfine coupling constant a is proportional to the squared amplitude of the electronic wavefunction at the nucleus.

The *fine interaction* in turn is related to the interaction between the total magnetic dipole moment of an electron with the magnetic field originating from magnetic dipole moments of other electrons in this system.

The Zeeman effect

In the Zeeman effect the splitting of the electronic energy levels of atoms is observed due to discrete orientations of magnetic dipole moment with respect to the magnetic field. This phenomenon is associated with spatial quantization of the total angular momentum (and hence also the total magnetic moment). The interaction between the external magnetic field and the magnetic dipole moment results in different energy levels associated with these orientations. The number of splitting components in the field is $2J + 1$. The energetic difference between the adjacent components, called the Zeeman energy, in the external magnetic field B is given by

$$\Delta E = g_J \mu_B B. \tag{4.11}$$

4.1.2 Physical background of MFEs in organic materials

This thesis focuses on magnetic field effects (MFEs) that occur in organic solids without magnetic elements (such as tris-(8-hydroxyquinolinato) aluminum (III), Alq3, described in the pioneering works of Kalinowski and co-workers [36, 37]) incorporated into systems without ferromagnetic electrodes, at room temperature. In these effects pairs of particles endowed with magnetic moment, namely doublet-doublet (D-D), doublet-triplet (D-T) or triplet-triplet (T-T) pairs, are involved. In the MFE technique the external magnetic field causes the precession of Coulombically bound electron-hole $(e-h)$ pair spins at a frequency dependent on the field strength B which results in magnetic field-dependent intersystem crossing between singlet, $^1(e-h)$, and triplet, $^3(e-h)$, pair spin states. The external magnetic field competes with the internal magnetic field - the fine field originating from electrons or the hyperfine field originating from magnetic nuclei, mainly hydrogen nuclei, i.e. protons. Due to different recombination and dissociation rates for $(e-h)$ pair states the population of emissive states involved in the electroluminescence (EL) processes and the charge carrier population in the dissociation events in the PV devices can be changed and, in fact, they are observed as a magnetic field effect on electroluminescence (MEL), photoluminescence (MPL), conductivity (MC) or photocurrent (MPC). The MFEs occur when effective spin mixing process takes place, provided that the spin coherence time of the $(e-h)$ pairs is long enough in comparison to electron spin flip time (e.g. 2 ns in the magnetic field of 10 mT) and that the electrostatic electron exchange interaction is sufficiently weak for efficient spin evolution to occur. Nevertheless, the origin of low magnetic field effects in organic solids is currently under heavy debate [38–40]. In order to clarify the MFEs previously observed in organic solar cells the following models have been proposed: (i) electron-hole pair (EHP) model involving reaction of charge carriers (polarons) with carriers of opposite sign into excitons, (ii) bipolaron (BP) model involving reaction of polarons with the same charge signs and (iii) fine structure modulation (FSM) model (Fig. 4.6). The above models are discussed in detail in the next sections.

4.1.3 Fine structure modulation (FSM)

The fine structure modulation (FSM) includes triplet-triplet annihilation (TTA) and triplet-polaron (T-q) interaction.

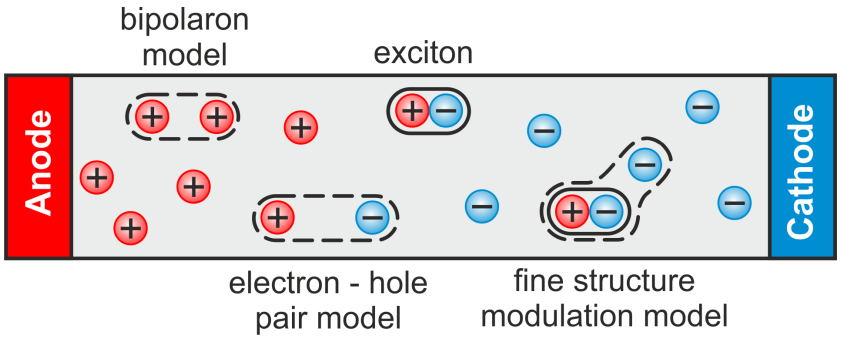

Figure 4.6. Illustration of particle interactions that are considered in the different MFE models (after [40])

T-T annihilation (TTA)

As a result of the collision of two triplet states ($S = 1$), a system called an encounter complex can be formed (see Fig. 4.7). Depending on the relative orientation of the spins, it may have the nature of singlet ($S = 0$), triplet ($S = 1$) or quintet ($S = 2$). In the case of typical organic solids (such as anthracene crystal) a pure quintet state is not energetically achievable. There are two possible decay pathways of such an encounter complex, i.e. a triplet channel resulting in a formation of a triplet excited state (T) and a singlet channel giving rise to the population of singlet states (S). The number of triplets participating in the triplet channel is independent of the magnetic field while the singlet channel, described with the rate constant k_s, is sensitive to the external magnetic field. In this case, the encounter complex is formed by mixed singlet and quintet states. The contribution of the quintet part is modulated by an external magnetic field, which has a direct impact on the number of emerging singlet states. Thus, the triplet-triplet interaction constant γ_{TT} and the rate constant k_s become functions dependent on the external magnetic field B (Figure 4.8) [41, 42].

The spin Hamiltonian of the system has the following form

$$\hat{H} = 2(g\mu_B \vec{B} \cdot \vec{S} + \vec{S}\mathbb{D}\vec{S}), \tag{4.12}$$

where the Lande factor g relates to the triplet state, $\vec{S}$ is the spin operator of a single triplet and $\mathbb{D}$ is a tensor of fine interactions of magnetic dipoles associated with two electrons that form the triplet state. The first term of the sum describes the Zeeman energy of the triplet while the second one is related to the fine interaction energy of electron magnetic dipoles. The

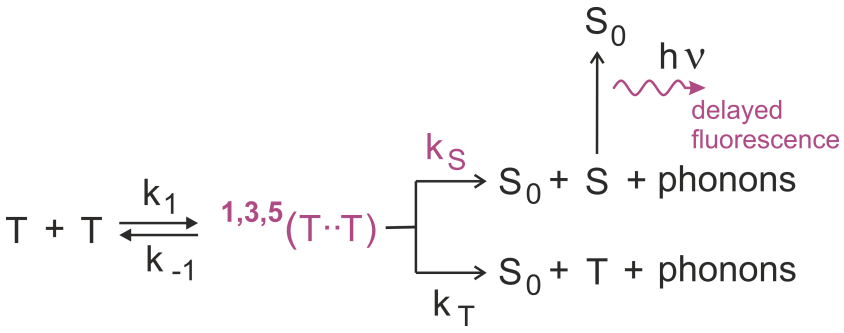

Figure 4.7. Schematic representation of the triplet-triplet annihilation process in a fluorescent emitter

triplet-triplet interaction constant is given by

$$\gamma \equiv \gamma_{TT}^{(S)} = \frac{1}{9} k_1 \sum_{n=1}^{9} \frac{k_s |C_S^n|^2}{k_{-1} + k_S |C_S^n|^2}, \tag{4.13}$$

where $C_S^n =< S|n >$ determines the contribution of the singlet state to the n^{th} state of the encounter complex.

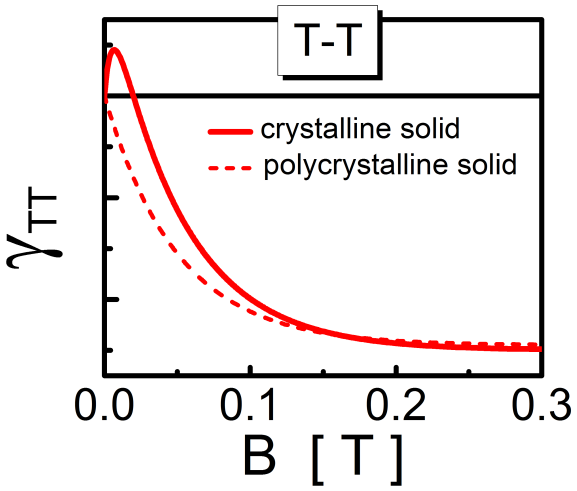

Figure 4.8. Dependence of the triplet-triplet interaction constant γ_{TT} on the external magnetic field B

In a crystal the dependence of the triplet-triplet interaction constant γ_{TT} is nonmonotonic which is related to the anisotropic properties of a crystal lattice while in the isotropic system (eg. polycrystalline film), the interaction constant value decreases with the increase of the external magnetic field. The

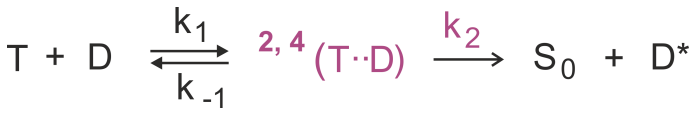

Figure 4.9. Schematic representation of the T-q mechanism. D - charge carrier, D - "hot" charge carrier*

interaction constant in a crystal takes a minimum value for the resonance directions. These MFEs occur if the value of the external magnetic field is comparable to the value of the fine structure interaction magnetic field, i.e. around 100 - 200 mT [43].

T-q interaction

In the T-q mechanism the external magnetic field, competing with the internal (fine) magnetic field of electronic spin origin, modulates the triplet state zero-field splitting (ZFS). In consequence, changes in carrier concentration or carrier mobility are observed as originally proposed in Ern and Merrifield model [44] or in trion model by Kadashchuk *et al.* [45] (see also [46, 47]), respectively. Recently Cox *et al.* proposed the trion model as the origin of magnetoresistance in organic semiconductors (organic magnetoresistance, dubbed often as OMAR) [46].

During the interaction of the triplet state ($S = 1$) with a charge carrier (doublet) state ($S = \frac{1}{2}$) a doublet-quartet mixed state can be formed with six different possible spin orientations (see Fig. 4.9). In the case of organic solids a pure quartet ($S = \frac{3}{2}$) state is usuallly not energetically achievable but it may be involved in the process of mixing with the doublet state. The contribution of the quartet part is modulated by the external magnetic field, which has an influence on the number of resulting final overall doublet states (S_0+D). Thus, the triplet-doublet interaction constant γ_{Tq} and the rate constant k_2 become the functions of the external magnetic field B (Figure 4.10).

The spin Hamiltonian of the system has the following form

$$\hat{H} = g_e \mu_B \vec{B} \cdot \vec{S}_e + g \mu_B \vec{B} \cdot \vec{S} + \vec{S} \mathbb{D} \vec{S}, \tag{4.14}$$

where the Lande factor g_e describes the doublet state, the Lande factor g is related to the triplet state, $\vec{S}_e$ is the spin operator of a doublet, $\vec{S}$ is the spin operator of a triplet and $\mathbb{D}$ is a tensor of fine interactions of magnetic dipoles associated with two electrons that form the triplet state. The first term describes the Zeeman energy of the doublet, the second - the Zeeman energy of the triplet while the third term describes the fine interaction energy of the magnetic dipoles forming the triplet state.The triplet-doublet interaction

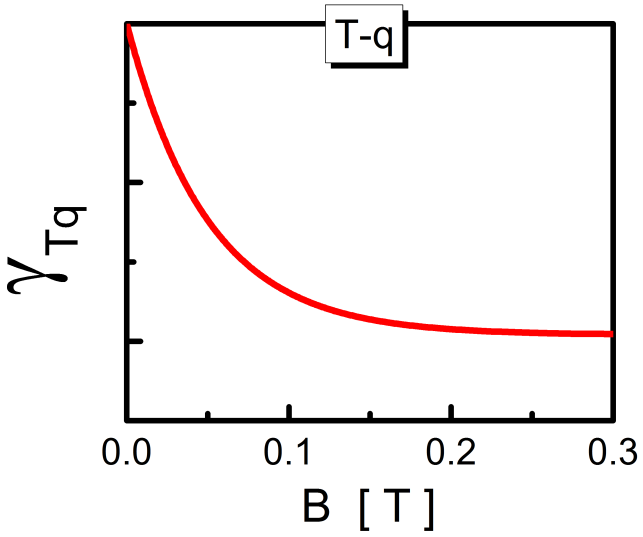

Figure 4.10. Dependence of the triplet-doublet interaction constant γ_{Tq} on the external magnetic field B

constant is given by

$$\gamma \equiv \gamma_{Tq}^{(D)} = \frac{1}{6} k_1 \sum_{n=1}^{6} \frac{k_n}{k_{-1} + k_n}, \tag{4.15}$$

where $k_n = k_2(| < D_{1/2}|n > |^2 + | < D_{-1/2}|n > |^2)$ determines the contribution of the doublet state $(m_s = +\frac{1}{2}, -\frac{1}{2})$ in the n^{th} state of the encounter complex.

The maximum value of the γ_{Tq} interaction constant is obtained in the absence of external magnetic field when the doublet character is shared equally by all six states. In higher magnetic fields, when the Zeeman energy is large compared to the zero-field splitting, all spin states are quantized along the external field. Then, at most four states have a doublet character, hence the smaller value of the interaction constant γ_{Tq}. In a crystal in the high magnetic field range, the γ_{Tq} interaction constant is anisotropic and reaches a minimum value for the orientation of the field, at which levels $|0, \pm\frac{1}{2} >$ and $| \pm 1, \mp\frac{1}{2} >$ are crossed (aligned) [44, 48].

In the trion model doublet-quartet precursor states, formed with rate constants $\frac{1}{3}k$ and $\frac{2}{3}k$ respectively, can back-dissociate with k_{-2} and k_{-4} rate constants, respectively, or generate overall doublet, ^{2}TD, and overall quartet, ^{4}TD, trions with the relevant rate constants, k_2 and k_4, respectively (Fig. 4.11). The ^{2}TD and ^{4}TD trions recombine with k_D and k_Q rates, respectively, restoring ground state, S_0, and free doublets, (q_f). Essential condition for

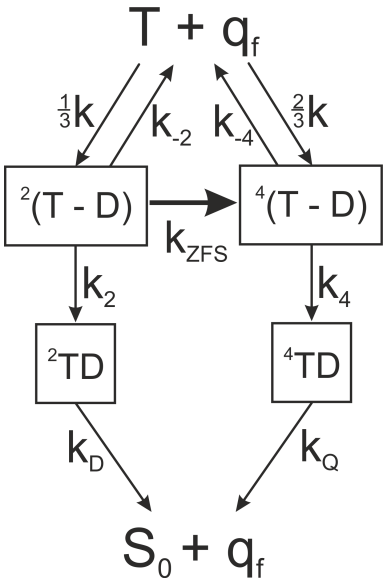

Figure 4.11. The simplified kinetic scheme representing the trion model (after [46, 47])

the functionality of this model is that the triplets operate as free-carrier-capturing centers hindering the carrier mobility. As a consequence, the overall process may be interpreted as a scattering of free carriers on triplet states. Since the recombination process of doublet trions is spin-allowed while the recombination of the quartet trions remaining spin-forbidden, the lifetime of the doublet trions is much shorter than that of quartet ones. Therefore, the quartet trions are more efficient in capturing free carriers and, hence, in reducing the photocurrent. Importantly, in the FSM-scale of magnetic field the population of the quartet trions is reduced whereas the population of the doublet ones increases due to reducing of the k_{ZFS} constant. This leads to the lower contribution of the quartet trions and, simultaneously, higher contribution of the doublet trions to the overall scattering process. One, therefore, should observe the increase in photoconductivity of an organic solid due to rising mobility of charge carriers [47].

4.1.4 Electron-hole pair mechanism (EHP)

The spin Hamiltonian of the electron-hole pair, $\hat{H}_{(e-h)}$, can be expressed by the sum of two components: the first one related to the exchange interactions between electron and hole, $\hat{H}_{ex}$, and the second one associated with the interaction of the external magnetic field with the electron-hole pair, $\hat{H}_{mag}$:

$$\hat{H}_{(e-h)} = \hat{H}_{ex} + \hat{H}_{mag}, \tag{4.16}$$

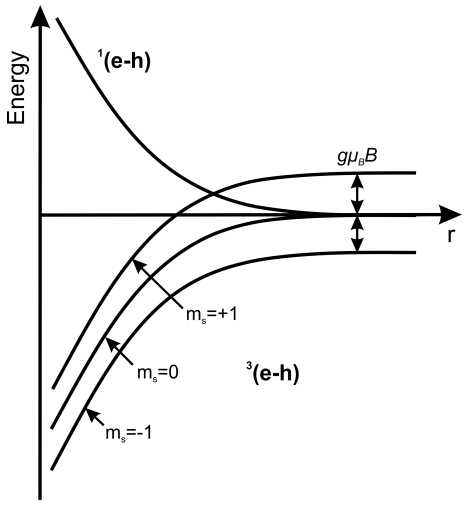

Figure 4.12. Dependence of $(e-h)$ pair energy on the distance (r) between an electron and a hole in the presence of the external magnetic field (after [12])

where

$$\hat{H}_{ex} = -J(2\vec{S}_e\vec{S}_h + \frac{1}{2}), \tag{4.17}$$

$$\hat{H}_{mag} = g\mu_B\vec{B}\cdot(\vec{S}_e + \vec{S}_h) + \sum_i \vec{S}_e a_{ei}\vec{I}_{ei} + \sum_j \vec{S}_h a_{hj}\vec{I}_{hj}. \tag{4.18}$$

In the expression for $\hat{H}_{ex}$ the term J is a parameter describing exchange interactions. The first term in eq. 4.18 denotes symmetrical Zeeman energy (the identical g factors of the electron and hole), the next two terms express the hyperfine interaction of the electron with the i^{th} nucleus and the hole with the j^{th} nucleus, characterized by the interaction coefficients a. $\vec{I}$ is the operator of the spin of the i^{th} (j^{th}) proton interacted with the electron (hole), $\vec{B}$ is the external magnetic field vector while $\vec{S}_e$ ($\vec{S}_h$) is the electron (hole) spin operator [12].

With reduction of the electron-hole distance (r) in an $(e-h)$ pair the energy of the $^1(e-h)$ state grows while the energy of the state $^3(e-h)$ state decreases, and therefore singlet-triplet splitting energy, conditioned by exchange interactions ($\hat{H}_{ex}$), increases (Fig. 4.12). In the prescene of the external magnetic field the term associated with the Zeeman effect splits the triplet level into three components $m_s = 0$, $m_s = -1$, $m_s = +1$. When r becomes large enough the triplet sublevels and singlet level are almost equal in energy (they are degenerate).

Hyperfine interaction modulation (HFM)

For a negligible exchange interactions (J) the electron-hole pair spin Hamiltonian takes the following form

$$\hat{H}_{(e-h)} = g\mu_B \vec{B} \cdot (\vec{S}_e + \vec{S}_h) + \sum_i \vec{S}_e a_{ei} \vec{I}_{ei} + \sum_j \vec{S}_h a_{hj} \vec{I}_{hj}. \tag{4.19}$$

In weakly bound $(e-h)$ pairs S and T levels are quasi-degenerate, which enables efficient intersystem conversion as a result of spin magnetic dipole precession in the internal (hyperfine) magnetic field of nuclear spins. If local magnetic fields experienced by the electron and the hole are the same then the identical precession frequencies preserve the initial spin configuration (Fig. 4.14 top and middle panels). However, in the case of the difference in local magnetic fields between proton environments of the electron and the hole, different spin precession frequencies lead to dephasing of spin magnetic dipoles (Fig. 4.14 bottom panel). Consequently, a singlet spin state is converted to a triplet spin state, and *vice versa*. According to Zeeman effect the low external magnetic field of several militesla competes with the hyperfine field (hyperfine interaction modulation - HFM) and thus splits the triplet sublevels $m_s = +1$ and $m_s = -1$, leading to the suppression of the ISC process between singlet and triplet $(e-h)$ pairs (Fig. 4.13). Assuming that the precession frequency of two spins differs by $\Delta\omega$ the time needed for a spin flip is $\frac{\pi}{\Delta\omega}$ [49–51].

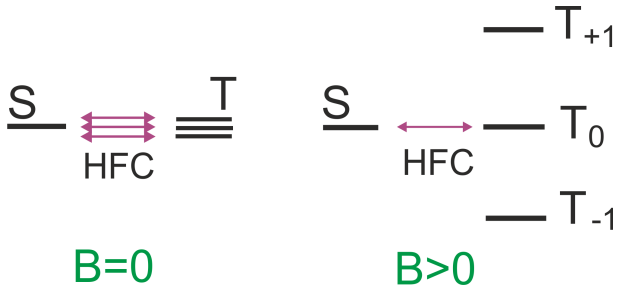

Figure 4.13. Schematic representation of the conversion mechanism of $^1(e-h) \leftrightarrow ^3(e-h)$ *pairs regarding to the hyperfine interaction modulation mechanism*

In a low external magnetic field singlet-triplet transition occurs to all triplet sublevels while in a high magnetic field, due to a symmetric part of the Zeeman term in a spin Hamiltonian and the energy difference, transitions to $m_s = +1, -1$ sublevels are blocked (Fig. 4.15).

In the hyperfine field (the field difference $\Delta B_{int} = 1$ mT between the electron and hole environment is appropriate here) the difference of spin

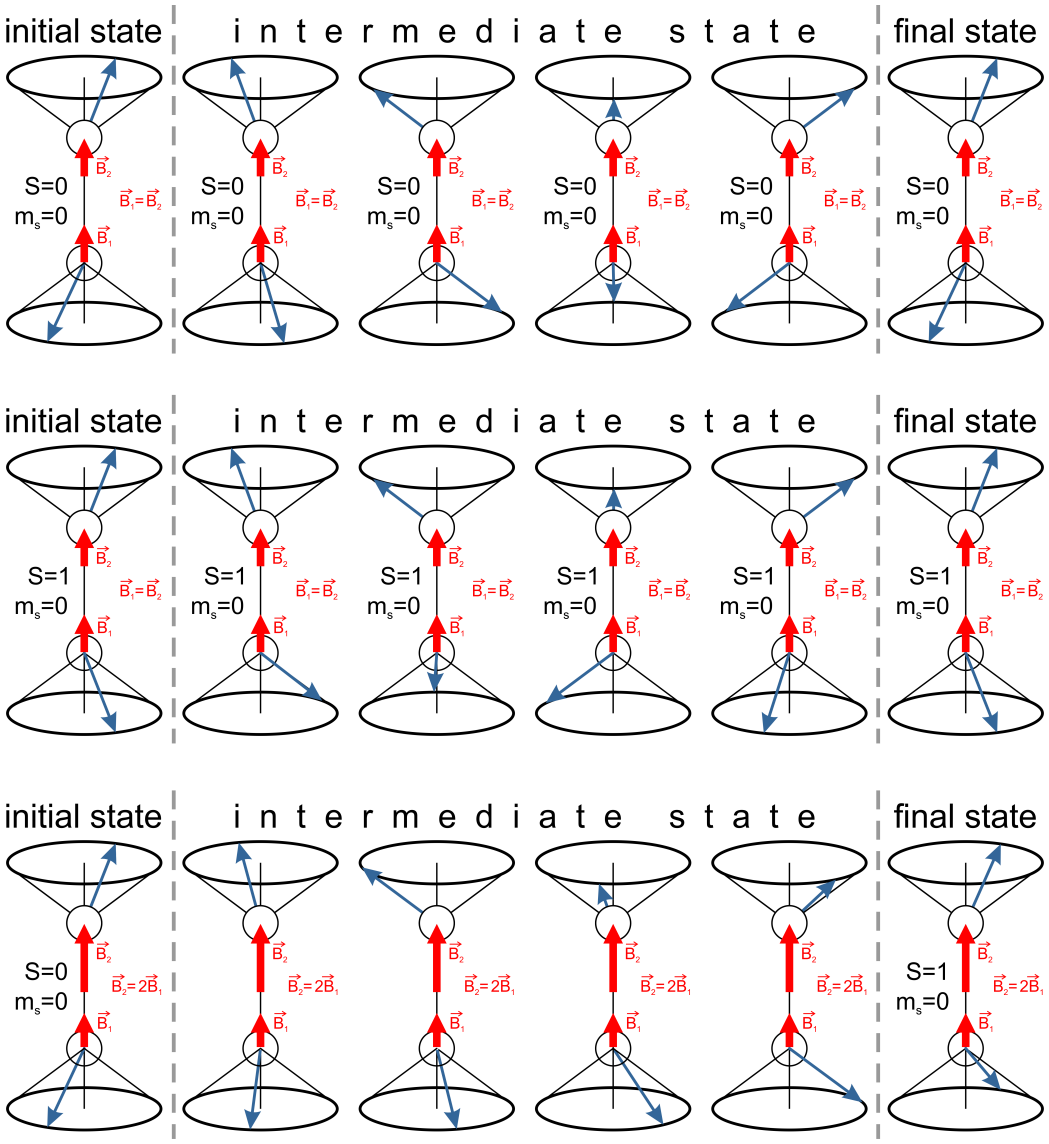

Figure 4.14. The same local magnetic fields (B_1 and B_2) experienced by the electron and hole forming $(e-h)$ pair preserve the initial spin configuration (see the top and middle panels). Differences in the local magnetic fields between the electron and hole environment cause transition of the initial singlet state ($S=0$, $m_s=0$) into the triplet one ($S=1$, $m_s=0$), as shown in the bottom panel of the figure (after [48])

precession frequency is given by

$$\Delta\omega = \frac{g\mu_B \Delta B_{int}}{\hbar}, \tag{4.20}$$

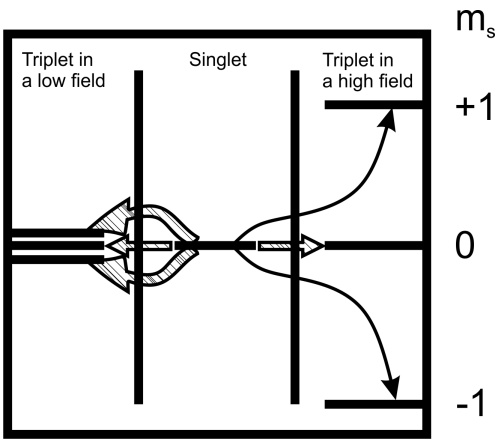

Figure 4.15. In a low magnetic field all three triplet sublevels may take part in the rephasing but at a high field rephasing to $m_s = \pm 1$ is blocked by the energy difference (after [48])

while the pair conversion time

$$t = \frac{\pi}{\Delta\omega} \approx 2 \times 10^{-8}\,\mathrm{s}, \tag{4.21}$$

where the Lande factor g was assumed as $g = g_j = g_s \approx 2$ (the orbital magnetic moment in the majority of molecules is effectively quenched). The spin flip time estimated here is comparable with the typical values of the $^1(e-h)$ pair lifetime in molecular systems which suggests that the spin conversion process can be efficient in these systems.

The γ_{ST} conversion rate of the $^1(e-h) \leftrightarrow {}^3(e-h)$ ISC process decreases with increasing B on the scale of several mT relevant for the degree of the HFM interaction to level off (saturate) at higher fields. (Fig. 4.16).

Δg mechanism

At high magnetic fields (typically of ca. 1 T for organic molecular systems [12]) dephasing of spin magnetic dipoles occurs as a result of different values of Lande g factor for electron and hole entities (g_e and g_h, respectively) forming $(e-h)$ pairs which leads to the field-induced enhancement in ISC between singlet and triplet, $m_s = 0$, states - the so called Δg mechanism. Then, the electron-hole pair spin Hamiltonian takes the form of

$$\hat{H}_{(e-h)} = g_e \mu_B \vec{B} \cdot \vec{S}_e + g_h \mu_B \vec{B} \cdot \vec{S}_h, \tag{4.22}$$

and the the difference of spin precession frequency is equal to

$$\Delta\omega = \frac{\mu_B B(g_e - g_h)}{\hbar}. \tag{4.23}$$

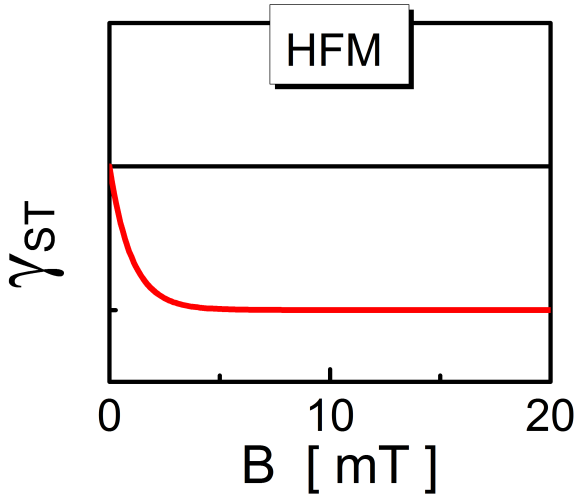

Figure 4.16. Dependence of the interaction constant of electron-hole pair conversion processes γ_{ST} on the external magnetic field B, due to the hyperfine interaction modulation

Hence the spin flip time $t = \frac{\pi}{\Delta\omega} \approx 3 \times 10^{-8}$s (for: $B = 1$ T and $g_e - g_h = 10^{-3}$ typical in organic systems) is again comparable with the $^1(e-h)$ pair lifetime. Thus, there is no $^1(e-h) \leftrightarrow {}^3(e-h)$ conversion in the absence of the external magnetic field while in the presence of the field singlet $\rightarrow$ triplet ($m_s = 0$) transition is enhanced due to the $\Delta g \mu_B B$ term ($\Delta g = g_e - g_h$) - Fig. 4.17. The γ_{ST} conversion rate of the $^1(e-h) \leftrightarrow {}^3(e-h)$ conversion process in the Δg mechanism monotonically increases with B (Fig. 4.18) [12, 48, 52].

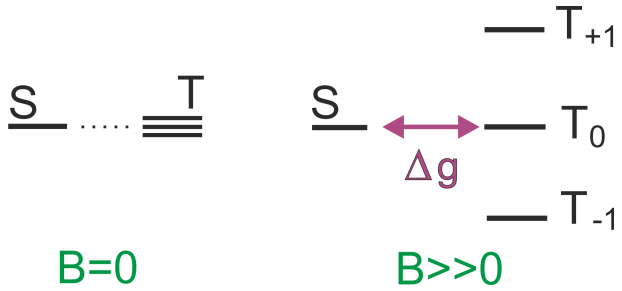

Figure 4.17. Schematic representation of the conversion mechanism of $^1(e-h) \leftrightarrow {}^3(e-h)$ pairs in the case of the Δg mechanism

The mixed effect of the HFM and Δg on γ_{ST} can also be pictured as follows: in the low magnetic field the rate constant decreases up to $B \approx 10$ mT (due to HFM) and then monotonically increases with B (due to Δg mechanism) to level off for magnetic fields of several T - Fig. 4.19 [12].

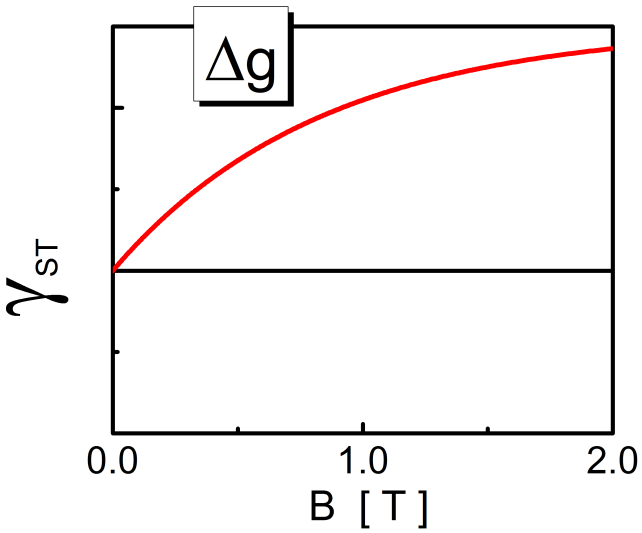

Figure 4.18. Dependence of the interaction constant of electron-hole pairs conversion processes γ_{ST} on the external magnetic field B due to the Δg mechanism

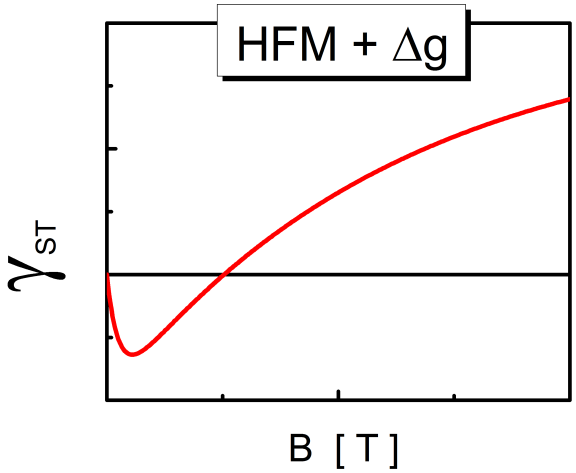

Figure 4.19. External magnetic field dependence of γ_{ST} in the case of the mixed HFM + Δg mechanism

4.1.5 Bipolaron mechanism (BP)

Bipolaron can be formed by two polarons with the same charge sign: electron-electron, $e-e$, or hole-hole, $h-h$, pairs. The bipolaron mechanism, i.e. a single carrier-type mechanism describing the line shape of MFE in the low field region (up to 10 mT), has been adopted for organic solids by Bobbert *et al.* [53] an has been further studied by Harmon and Flatté on the basis of the semiclassical theory [54]. The spin hamiltonian describing bipolarons is similar to the one for HFM of electron-hole pairs (see formula 4.19).

In order to form a bipolaron, a polaron must hop to a site occupied by another polaron. Due to the the Pauli exclusion principle (double occupation at a single site is forbidden if the resultant spin of these entities gives a triplet state but permissible for the resultant singlet state) polarons must have opposite spins. Otherwise formation of bipolarons is blocked. At zero external magnetic field efficient hyperfine spin mixing occurs. Then, polaron pairs which are initially in a triplet configuration can be mixed by HFM into a singlet configuration enabling bipolaron formation. If the external magnetic field is higher than the hyperfine field, B_{HF}, the spins coherently precess around the external field quenching the spin mixing. Thus, polaron pairs which are initially triplets will be preserved. In the case of single sign current flow in organic solids, hopping of charge carriers from site to site should be considered (Fig. 4.20). If there is an occupied site on the path, e.g. occupied low energy trap level, direct pass through this site is possible only with the bipolaron formation. Otherwise, i.e. when the precursor polarons will form a triplet polaron pair configuration, current cannot flow. This situation, called spin blocking, leads to a reduced mobility of carriers and thus also to a reduction in current. Therefore, effective charge transport through occupied state occurs only when there is a hyperfine field induced spin mixing, so when the external magnetic field is lower than the hyperfine field.

4.2 Literature review

4.2.1 MFEs in dye-sensitized solar cells

The photoconversion efficiency of DSSCs is limited by the electron transfer processes proceeding at the oxide semiconductor/dye/electrolyte interfaces. Among others, the charge recombination and exciton dissociation are generally recognized as the basic electronic processes limiting the efficiency of photovoltaic devices. Ultrafast electron transfer to TiO2 conduction band

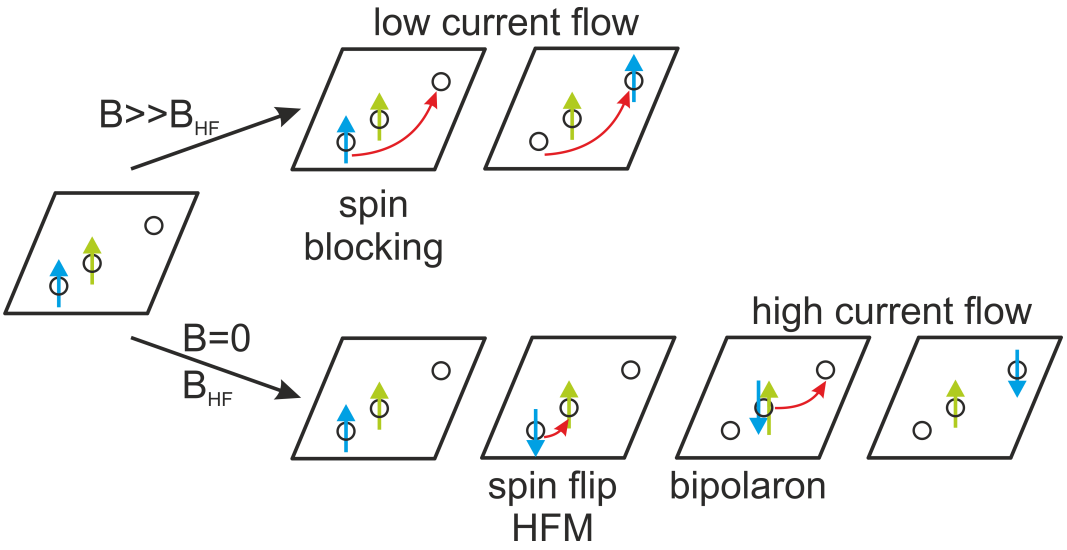

Figure 4.20. Spin blocking in transport for hopping a triplet polaron pair at a high magnetic field ($B > B_{HF}$) - top. Bipolaron formation due to the HFM spin mixing at a low magnetic field $B < B_{HF}$) - bottom

from metal-to-ligand charge transfer photoexcited state of Ru-bipyridyl dyes can occur from a singlet state (^1MLCT) as well as from a triplet state (^3MLCT) as a result of heavy metal atom induced efficient intersystem crossing ($\sim 10^{-12}$ s). For pure organic dyes this electron transfer occurs efficiently only from a singlet excited state due to spin-forbidden singlet-to-triplet intersystem crossing process [55]. Although this primary charge separation step in DSSCs has been extensively studied by femtosecond transient absorption spectroscopy [55–59] the exact nature of the spatial separation of charge carriers involving possibly an intermediate stage of geminate electron-hole pairs or exiciplex states is not fully understood so far [57, 60]. Nevertheless, if these intermediate species are endowed with the magnetic moment then a low external magnetic field of tens of mT strength can interact with them and this way change the generated photocurrent as observed in Alq3 films [36], starburst amine (m-MTDATA):bathocuproine (BCP) system [61] or in poly(3-hexylthiophene) (P3HT):[6,6]-phenyl-C60-butyric acid methyl ester ($PC_{60}BM$) bulk-heterojunction solar cells [62, 63]. Therefore, near-unity quantum efficiency of organic solar cells is achieved not only due to efficient $(e - h)$ pair dissociation by electric field but it arises through the interplay between spin, energetics and delocalization of electronic excitations in organic semiconductors [64]. The literature on magnetic field effects in DSSCs is rather sparse. A recent study on electronic processes in p-type DSSC with Au nanoparticles-doped photocathode has shown that the

photocurrent and photoconversion efficiency enhancement does not originate from increased absorption due to surface plasmon resonance (SPR) of electrons in nanoparticles but is rather induced by the local electric-magnetic field effect on electron injection process at a dye-semiconductor interface [60]. The magnetic field effects occur when effective spin mixing process takes place provided that the spin coherence time of the $(e-h)$ pairs is long enough in comparison to electron spin flip time (e.g. 2 ns in the magnetic field of 10 mT) and the electrostatic electron exchange interaction is sufficiently weak for efficient spin evolution to occur. The exchange interaction energy can be modulated by the $(e-h)$ pair radius (distance between the electron and hole) and the pair lifetime (thus also the spin coherence time) relying on the charge carrier mobility. The latter can be modified by the disorder degree of the semiconductor and defect states of the dye molecules.

Recently MFEs have been also reported for various n-types of dye-sensitized solar cells with ruthenium-based dyes [65, 66], however, the proposed mechanism of these effects is unclear. The authors suggest that the observed photocurrent increase is related to EHP model, which in fact should be inactive in such low magnetic fields (several tens of mT) due to a strong spin-orbit coupling induced by an orbital magnetic field of a heavy metal atom in a dye molecule [67, 68].

4.2.2 MFEs in organic solar cells

Over the last few years, the interest in squaraine (SQ) dyes as an electron donor material for photovoltaic applications has grown rapidly [69, 70]. It is associated with the unique photophysical properties of these organic compounds: high absorption coefficients (approximately 10^5 cm^{-1}) and narrow absorption bands only in the visible-near infrared region (from ∼550 nm even up to ∼1000 nm) [71, 72]. Due to relatively simple synthesis routes, various derivatives of SQ dyes have been developed and found to be applicable in new generation PV technologies: dye-sensitized solar cells, organic photovoltaic devices with both planar- and bulk-heterojunction architectures as well as perovskite solar cells [69]. The last decade has observed a sharp rise in the photoconversion efficiency of these devices (5.9% and 6.1% for SQ:fullerene in PHJ [73] and BHJ [74] architecture, respectively, 8.3% for SQ/polymer/fullerene tandem solar cells [75] and over 10% for the quaternary organic solar cells [70]) which indicates that SQ:fullerene based OPV cells have significant potential for future commercial applications. Moreover, squaraine has been considered as a possible material for spintronic applications [76]. Rather short exciton diffusion length ($L_D \leq 2$ nm [77]) and low charge carrier mobility in SQ thin films, in comparison to those in $PC_{70}BM$

(phenyl-C70-butyric acid methyl ester, L_D = 20 to 40 nm [78]), implied promise for use of SQ:fullerene blends with the compositional ratio strongly favoring fullerene (the best photoconversion efficiencies, 5.5%, obtained for 1:6 SQ to fullerene weight ratio) [78]. Even though the observed low fill factors (FF) for current-voltage characteristics suggest that the process of exciton dissociation / carrier pair recombination to be field-dependent [19], nevertheless, the authors of ref. [79] argue that in such systems with poor transport properties (high internal resistance and short path length of exciton diffusion in SQ) low charge collection governs the cell performance.

Nowadays, further improvement in the performance of organic solar cells can be achieved by applying the following strategies: (i) tuning or broadening the absorption band of photoactive materials for better matching with the solar spectrum [69]; (ii) employing new device architectures, especially tandem solar cells [80], maximizing the open circuit voltage by appropriate energy levels alignment, namely, a charge transfer level (in donor-acceptor systems) should lie close to a singlet state of the donor (S_1) [81]; (iii) enhancing photocurrent densities by singlet fission based strategies [82, 83]; (iv) enabling the suppression of electron-hole recombination by taking into account the interplay between spin, energetics and delocalization of electronic excitations [64]. The primary step of photocurrent generation in organic solar cells is the dissociation of photogenerated excitons by charge transfer across the donor-acceptor interface leading to the formation of bound interfacial charge-transfer states where an electron and a hole are located on separate molecules, i.e. on the acceptor and donor molecules, respectively. Such bound charge pairs can dissociate into free carriers generating a photocurrent or restore the ground state by means of geminate recombination [64, 84]. Due to larger separation distance of electron-hole pairs, compared to molecular excitons, relatively weak electrostatic electron exchange interactions result in CT states of singlet ^1CT and triplet ^3CT spin character, almost degenerate in energy. Therefore, the role of spin of electronic excitations is essential when considering the possible pathways for both photocurrent generation and recombination losses in photovoltaic devices [64, 84, 85].

Recently, magnetic field effect (MFE) technique has been recognized as a powerful tool for studying spin-dependent generation and recombination processes of spin-pair species in organic semiconductors or polymer based solar cells and light emitting diodes [38, 67, 68, 85–90]. In state-of-the-art polymer donor:$PC_{60}BM$ devices, depending on the $PC_{60}BM$ concentration and external magnetic field strength, various MFEs on a photocurrent have been observed. For pristine P3HT films or its blends with a low $PC_{60}BM$ concentration ($<$ 1 wt.%) in a low magnetic field (a few militesla) the positive component of MPC is related to the hyperfine interac-

tion modulation (HFM) in $(e-h)$ pairs while the negative component at a higher magnetic field (tens of militesla) involves exciton-charge reactions (T-q model) occurring in the triplet excitonic states [67]. Similar effects have been reported for blends with a poly(2-methoxy-5-(3,7-dimethyloctyloxy)-1,4-phenylenevinylene) (MDMO-PPV) as a donor [86]. Intermediate concentrations of $PC_{60}BM$ (30-60 wt.%) leads to the formation of CT states at the donor-acceptor interface [68, 86] whereas for a high $PC_{60}BM$ content (over 70%) strong phase separation occurs and only a negative MFE at a low magnetic field, outlined as a bipolaron (BP) mechanism, is present [86]. The MPC effect at a high magnetic field (ca. 1 T) in P3HT:$PC_{60}BM$ system and intermediate $PC_{60}BM$ content is reported to be related to the CT states without the specification of the exact mechanism of observed effects [67]. However, accordingly to other reports [68, 86], that MPC effect is associated with the dephasing of spin magnetic dipoles due to different values of Lande g factors ($\Delta g \sim 10^{-3}$) for electron and hole entities forming CT states (the Δg mechanism).

5 Experimental details

5.1 Materials

SQ2 and N719 dyes were purchased from Solaronix while $PC_{60}BM$ was purchased from Lumtec. B1 dye was synthesized according to the procedure described in the ref. [91]. All the chemicals used were of analytical grade and were used as received without any additional purification.

5.2 Sample preparation and characterization

Preparation and characterization of TiO_2 NTs and NPs photoanodes

FTO substrates (7 Ω/□, Aldrich) and titanium (Ti) plates (Steam, 99.7%) were cleaned in an ultrasonic bath sequentially in acetone, ethanol and deionized (DI) water 10 min each and then dried in a stream of hot air. Titania nanotubes (NTs) were prepared *via* a two-step electrochemical anodization of a Ti plate in a two-electrode configuration with a platinum mesh as a cathode. The distance between electrodes was set to 2.5 cm. First anodization was conducted under bias of 40 V for 2 h in the electrolyte containing 0.27 M NH_4F and 1 M H_3PO_4 in 1/99 v/v water/ethylene glycol solution at a constant temperature of 23°C controlled by a thermostat (Julabo F-12). Then, Ti plates were immersed in a 0.5 wt.% solution of oxalic acid and left overnight prior to the next anodization that was performed under the same conditions as the first one, but in the electrolyte containing 0.27 M NH_4F in 5/95 v/v water/ethylene glycol solution. In order to remove surface debris, the titanium plates covered with nanotubes were ultrasonically cleaned in a 0.05 wt.% solution of HF in DI water for 60 s. As-cleaned anodized plates were then dried at 200°C (1°C/min heating rate) for 1 h followed by

annealing at 480°C (1°C/min) for 40 min. In order to detach the nanotube membrane from Ti plates, the annealed plates were anodized again in the same way but under bias of 60 V. The obtained nanotube membranes were then transferred onto FTO substrates, pre-coated with a buffer layer, immersed in the isopropyl alcohol (IPA) filling up a Petri dish, in a similar manner to that described by Li *et al.* [92]. A 50 nm anatase buffer layer was prepared as follows: 20 μl of titanium isopropoxide (97%, Aldrich) solution in IPA with Triton X-100 (Aldrich) and acetic acid in a volume ratio of 1:20:4:2 was spin-coated at 3000 rpm onto FTO for 1 min and then annealed at 450°C (10°C/min) for 30 min. The FTO substrates covered with NT membranes were then removed from IPA and for better adhesion two drops of the above-mentioned isopropoxide in IPA solution were applied to the side of the membrane. Finally, the NTs/FTO electrodes were dried at 200°C (1°C/min heating rate) for 1 h and annealed at 450°C (10°C/min) for 1 h. For preparing NPs/FTO electrodes titania paste (Ti-nanoxide HT, Solaronix) was spread onto a FTO substrate using the "doctor blade" technique and sintered at 450°C (10°C/min) for 1 h.

Raman scattering spectroscopy measurements were carried out at room temperature using a confocal micro-Raman spectrometer (InVia, Renishaw) and a 514 nm argon ion laser, operating at a 10% of its total power (50 mW), as the excitation. X-ray diffraction (XRD) measurements were performed on a X'Pert Pro MPD diffractometer (Philips) with CuKα radiation. The morphology of the titania electrodes was characterized by scanning electron microscopy (FEI Quanta FEG 250).

Absorption Spectroscopy

UV-VIS absorbance spectra of 2×10^{-5} M dye solutions (N719, B1, SQ2) in dry ethanol were measured by a Lambda 35 UV-VIS spectrophotometer (Perkin Elmer).

Active layers of SQ2 and $PC_{60}BM$ for UV-VIS absorption and thickness measurements were deposited onto microscope glass slides in accordance with the following procedure. Microscope glass slides were cleaned using sequentially acetone, ethanol and deionized water 10 min each in ultrasonic bath and then dried in a stream of dry nitrogen followed by a 15 min ozone treatment. Afterwards substrates and materials were transferred into nitrogen-filled glove box ($[O_2] < 1$ ppm, $[H_2O] <$ 1 ppm). SQ2 and $PC_{60}BM$ were separately dissolved in anhydrous chlorobenzene (99.8%, Aldrich) at 60°C overnight and mixed in order to prepare appropriate SQ2 to $PC_{60}BM$ weight ratios. The solutions were heated at 60°C for 2 h just prior to spin-coating. SQ, SQ:PCBM (1:0.1%), SQ:PCBM (1:10%) and SQ:PCBM (1:6) thin films

were spin coated from 10, 10, 11 and 42 mg mL^{-1} solutions at rates of 1500, 1500, 1500 and 1000 rpm for 90 s giving active layers of thickness of around 20, 20, 23 and 75 nm (as determined by the Tencor Alpha Step 500 Profilometer), respectively. The films were then annealed at 110°C for 10 min. Absorbance spectra were recorded by the Lambda 35 UV-VIS spectrophotometer (Perkin-Elmer).

AFM measurements

Samples for atomic force microscopy (AFM) were prepared in the same manner as those used for absorption spectroscopy. Surface morphology was examined by a Dimension 5000 (Veeco) AFM operated in a tapping mode.

EPR measurements

Electron paramagnetic resonance (EPR) measurements of a radical cation of SQ2 were performed using a JEOL JES-FA200, X-band CW-EPR (continuous-wave electron paramagnetic resonance) spectrometer, operating at 100 kHz field modulation, coupled with a PGSTAT 100N potentiostat (Autolab). Measurements were carried out in a glass cell narrowed at the bottom, to provide proper conditions for recording of EPR spectra, equipped with a Pt wire working electrode, an Ag wire pseudoreference electrode (calibrated vs. Fc/Fc^{+}) and a Pt coil counter electrode. Electrolysis was carried out at the potential corresponding to the first oxidation potential (see Fig. 5.1). The g-factor of the generated radical cations was determined by comparison with a JEOL internal standard (Mn(II) salt), knowing that its third hyperfine line has a g-factor of 2.03324. Cyclic voltammogram of SQ2 and EPR spectra of radical cation of SQ2 are shown in Fig. 5.1 and 5.2 - 5.3, respectively.

DFT calculations

The ground state structures of the TiO_2-dye system were determined applying the electron density functional theory (DFT) - see ref. [93]. The geometric optimization was performed by a parametric method 6 (PM6) using the Scigress 2.1.0 program [94]. The DFT calculations were performed using the GAUSSIAN 03 package [95]. The geometries were optimized according to Becke's three parameters hybrid method with the Lee, Yang and Parr exchange-correlation electron density functional (B3LYP) and 3-21G basis set. To model the TiO_2 nanoparticles and surfaces, we considered $(TiO_2)_{38}$, $(TiO_2)_{76}$ and $(TiO_2)_{104}$ clusters which were obtained by appropriate "cutting" of an anatase slab exposing the (101) surface.

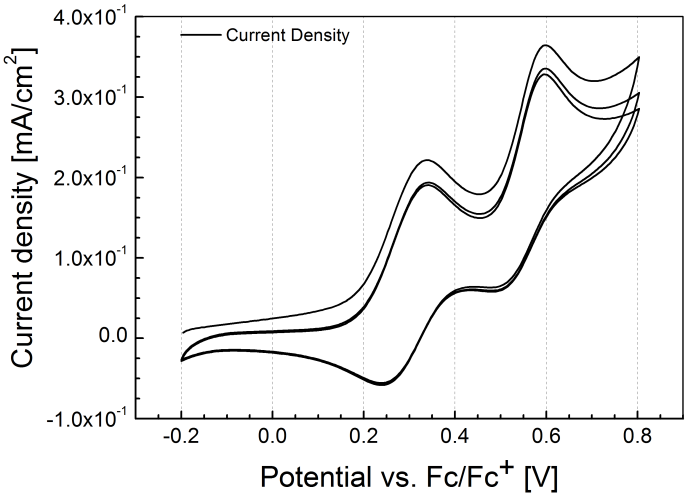

Figure 5.1. Cyclic voltammogram of SQ2. Measurements conditions: 1 mM solution of SQ2 in 0.1 M dichloromethane/tetrabutylammonium hexafluorophosphate electrolyte, scan rate: 100 $\frac{mV}{s}$

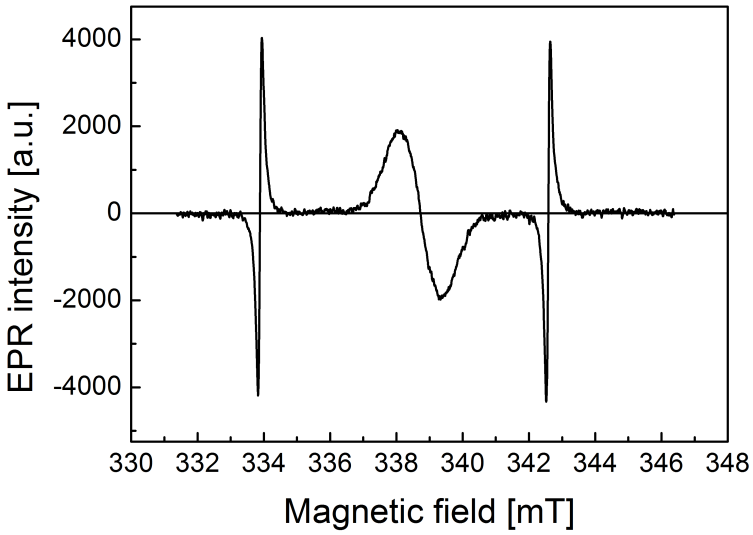

Figure 5.2. EPR spectra of radical cation of SQ2, recorded in-situ during oxidation at potential of 0.3 V vs. Fc/Fc$^+$. Measurement conditions: microwave power: 2 mW, modulation width: 0.1 mT. Two sharp lines on the sides of the spectrum correspond to the g factor internal standard of the spectrometer

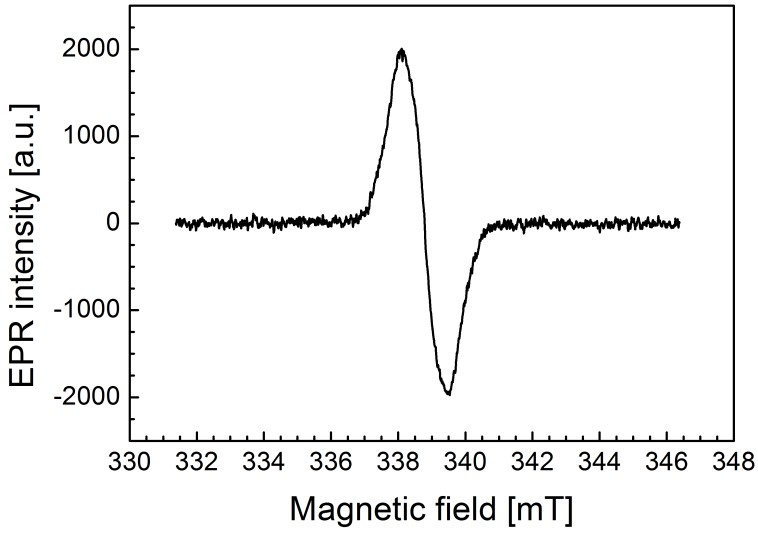

Figure 5.3. EPR spectra of radical cation of SQ2, recorded in-situ during oxidation

Energy levels

The N719 and SQ2 energy levels were taken from ref. [55, 96, 96]. The SQ2 triplet level was estimated on the basis of the data given in ref. [97, 98]. Energy levels of $PC_{60}BM$ were taken from ref. [99]. The upper limit of the CT states energy level (E_{CT}) for electron donor (D) - electron acceptor system (A) was calculated from the following formula

$$E_{CT} \approx |E^A_{LUMO}| - |E^D_{HOMO}|. \tag{5.1}$$

5.3 Solar cells preparation and characterization

Dye-sensitized solar cells

To prepare photoanodes titania electrodes were immersed in a 1×10^{-4} M solution of N719 (Solaronix) or B1 (synthesized by us [91]) dye in absolute ethanol or in a mixture of 1×10^{-3} M chenodeoxycholic acid (Solaronix) and 1×10^{-4} M SQ2 (Solaronix) dye in absolute ethanol at room temperature overnight. A platinum coated FTO was used as a counter electrode and a mixture of 0.6 M 1-butyl-3-methyl imidazolium iodide (Aldrich), 0.06 M lithium iodide (Aldrich), 0.03 M iodine (Poch), 0.1 M guanidinium isothiocyanate (Aldrich), 0.5 M 4-tert-butylpyridine (Aldrich) in acetonitrile was used as an electrolyte. The cell was assembled using a 25 μm thick,

hot-melted, ionomeric foil (Meltonix 1170-25, Solaronix) as a sealant and a spacer between the electrodes. An electrolyte was injected within two holes predrilled in the counter electrode. The final sealing was realized with the use of hot melted sealant and a microscope cover slide. The photovoltaic characteristics of the cells were measured using 150 W xenon solar simulator (Optel) equipped with an AM1.5 filter, with the light intensity adjusted to 100 mW cm^{-2} using a silicon reference cell (ReRa Systems). Photocurrent density-voltage (J-V) curves were recorded on a 2400 SourceMeter (Keithley).

Organic solar cells

SQ:$PC_{60}BM$ devices were fabricated on etched ITO coated glass substrates (resistivity = 100 $\Omega/\square$) which were cleaned using sequentially acetone, ethanol and deionized water 10 min each in ultrasonic bath and then dried under a stream of dry nitrogen followed by ozone treatment for 15 min. Afterwards substrates and materials were transferred into nitrogen-filled glove box ($[O_2] < 1$ ppm, $[H_2O] <$ 1 ppm). The ITO glass substrates were then transferred into the vacuum system connected directly with the glove box and a MoO_x layer of 8 nm thickness was thermally evaporated at a base pressure of $\sim 10^{-6}$ Torr. Afterwards SQ, SQ:PCBM (1:0.1%), SQ:PCBM (1:10%), SQ:PCBM (1:6) thin films were spin-coated in a similar manner to the sample preparation procedure used for UV-VIS absorption and thickness measurements. The devices were completed by thermal evaporation of a cathode, consisting of 8 Å LiF and 60 nm Al, through a shadow mask in a vacuum system with a base pressure of $\sim 10^{-6}$ Torr. J-V curves were recorded under 100 mW cm^{-2} AM1.5 illumination conditions in ambient air on a 2400 SourceMeter (Keithley). As a light source a class A solar simulator (Oriel) was used. A light intensity was adjusted using a silicon reference cell (ReRa Systems).

5.4 Magnetic field effect measurements

Dye-sensitized solar cells

For magnetic field effect measurements the samples were placed between the pole pieces of an electromagnet in a way that the magnetic field was parallel to the device plane. The applied magnetic field strength was controlled by an adjustable stabilized dc-power supply and a flat Hall-effect probe connected with a magnetometer (HGS-10A) placed close to the sample holder.

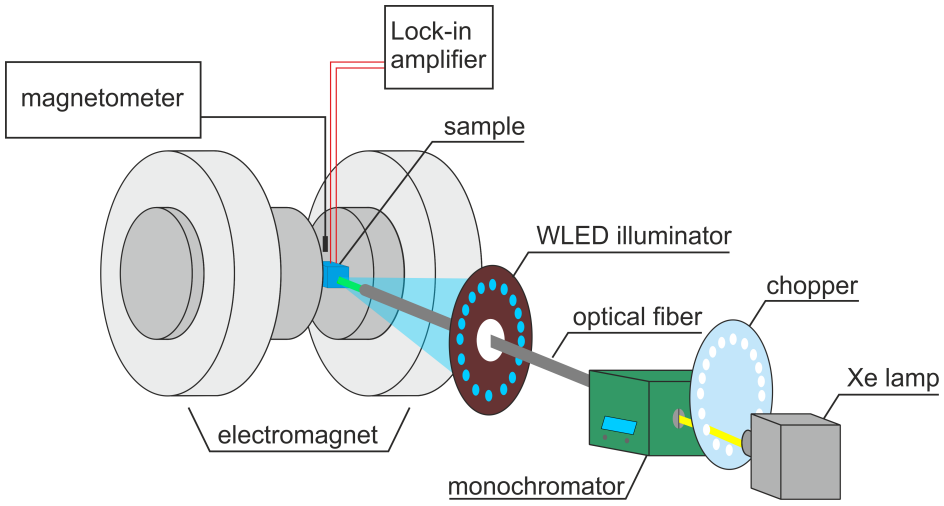

Figure 5.4. Schematic drawing of an experimental arrangement for measuring the magnetic field effects on photocurrent

The samples were illuminated simultaneously by two light sources: a constant white bias light from a homemade LED illuminator, composed of 14 white light emitting diodes (with a power of 30 mW for each diode) focused onto the sample, and a single wavelength illumination setup consisted of a xenon lamp, a monochromator (SPM 2, Zeiss Jena) connected with a one meter-long linear quartz waveguide and an optical aperture with a diameter of 5 mm to limit the active area (photon flux of approx. 10^{14} cm^{-2} s^{-1}). Between a xenon lamp and a monochromator an optical chopper (MC2000, Thor Labs) was placed to modulate the monochromatic excitation light at 5 Hz frequency. The short circuit photocurrent of solar cell was measured by lock-in amplifier (5210, EG&G Princeton Applied Research), referenced by chopper signal, connected with the sample through a current-voltage converter preamplifier (EG&G Princeton Applied Research). Measurement setup for a MFE measurements is depicted in Fig. 5.4. The monochromator output wavelength was set at 520 nm, 450 nm and 650 nm for N719, B1 and SQ2 dye based solar cells, respectively.

Organic solar cells

For MFE measurements devices were transferred through a nitrogen filled container to a Quantum Design Physical Property Measurement System (PPMS) equipped with a superconducting magnet and kept in a vacuum (< 1 mTorr). The devices were driven at a constant bias voltage $U = 0.1$ V using a Keithley 6487 Picoammeter Voltage Source and were illuminated us-

ing a L658P050 laser diode (658 nm center wavelength and 50 mW output power, ThorLabs) and a few meters long optical fiber introduced into the PPMS chamber. An incident photon flux of approx. 10^{16} cm^{-2} s^{-1} was achieved.

6 Results and discussion

6.1 MFEs in dye-sensitized solar cells

6.1.1 Characterization of dyes and TiO_2 photoandoes

In order to carry out the experimental work a set of dye-sensitized solar cells in a typical configuration with a liquid electrolyte, TiO_2 photoanode with adsorbed dye (ruthenium N719, dinuclear ruthenium B1 or fully organic squaraine SQ2) and platinum counter electrode were prepared (cf. Fig. 3.2 and Fig. 6.1). Titania electrodes had a form of randomly packed nanoparticles (NPs) film or highly ordered nanotubes (NTs) array. TiO_2 NPs photoanodes, with a thickness of about 11 μm were composed of nanoparticles of 8-10 nm average diameters (Fig. 6.2). Prepared by two step electrochemical anodization process of Ti metal foil, titania NTs with an average outer diameter of 90 nm and 6 μm in length were deposited onto the fluorine-doped tin oxide (FTO) glass substrates (Fig. 6.3) and as such were used as TiO_2 NTs photoanodes. Both of the applied TiO_2 electrodes consist of the anatase phase, as confirmed by Raman spectroscopy (Fig. 6.4) and XRD (Fig. 6.5) [100].

Titania nanotubes offer short electron percolation pathways to charge-collecting contacts in contrast to nanoparticle matrix (Fig. 6.6) while charge transport rate measured via the transient photocurrent and photovoltage decay techniques is around 10 fold slower [101], and presumably is related to the fast trapping of free electrons occurring on time scale of a few tens of picoseconds which is at least an order of magnitude faster than in sintered nanoparticle film, and is induced by the higher concentration of shallow trap states [102]. These results suggest that different lifetimes of free electrons in TiO_2 NT and TiO_2 NP conduction bands should affect two factors characterizing $(e-h)$ pairs involved as the intermediate stage of photocurrent generation process: the spin coherence time and the pair radius which is essentially the distance between a TiO_2 trapped electron and a hole localized on a dye molecule. Namely, faster transport and longer lifetime of the free

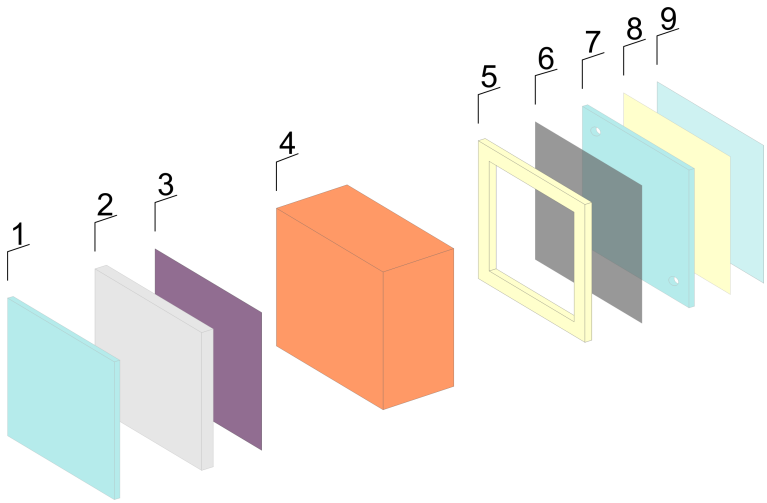

Figure 6.1. Schematic diagram of the DSSC assembled in the laboratory. 1 - FTO glass substrate, 2 - semiconductor layer, 3 - dye, 4 - electrolyte, 5 - gasket, 6 - Pt catalytic layer, 7 - FTO glass substrate with drilled holes for an electrolyte injection, 8 - gasket, 9 - microscope cover slide

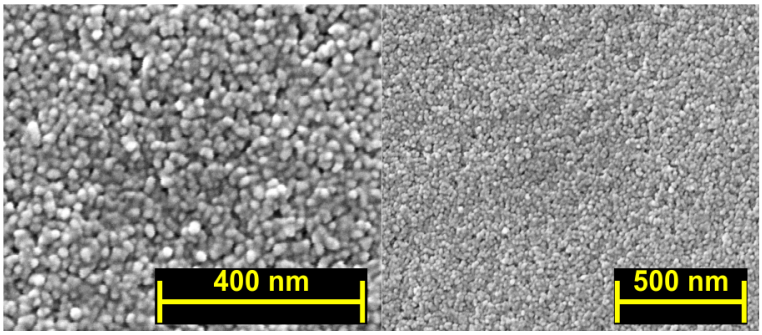

Figure 6.2. SEM image of TiO_2 NPs layer. Top view in a high (left) and low (right) magnification

electrons in a NP layer makes the $(e-h)$ pairs acquire greater radii. Moreover, the $(e-h)$ pair radius will depend also on a specific orbital arrangement of the three applied sensitizers in the form of: commercially available ruthenium N719 and squaraine-based SQ2 dyes, and reported by us earlier dinuclear ruthenium polypyridine B1 dye [91]. Absorption spectra of these dyes are shown in Fig. 6.7a, 6.7b and 6.7c, respectively, while their molecular structures are shown in Fig. 6.8a, 6.8b and 6.8c, respectively. The above mentioned ruthenium dyes exhibit the absorption bands in the visible region with maxima at 525 nm and 460 nm for N719 and B1, respectively, corresponding to $MLCT$ transitions whereas absorption band with a maximum at 650 nm for SQ2 corresponds to $\pi \rightarrow \pi^{\star}$ transition. We expect that both the

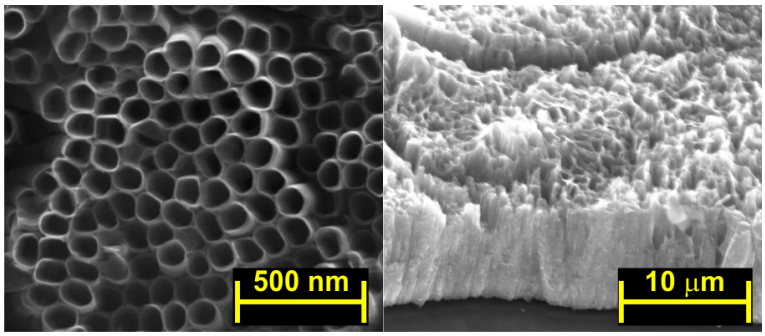

Figure 6.3. SEM image of TiO_2 NTs layer. Top (left) and cross-section (right) view

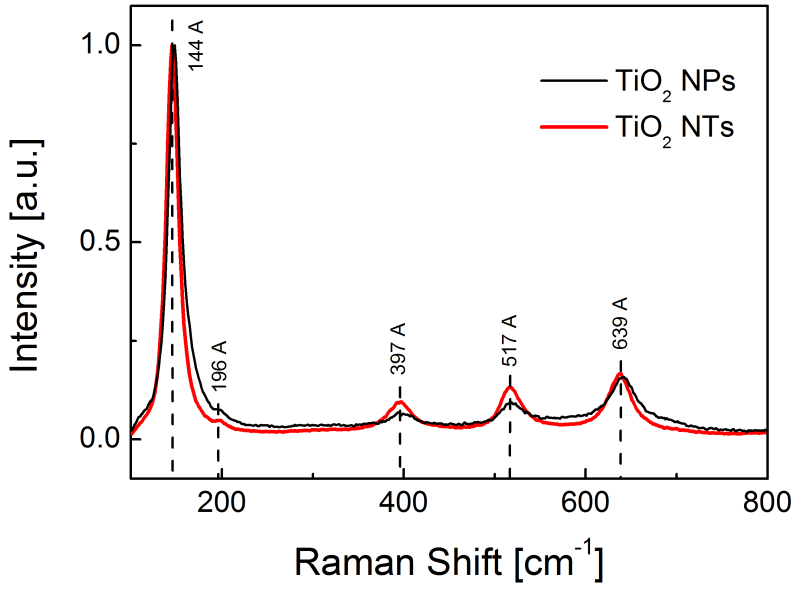

Figure 6.4. Raman spectra of TiO_2 NPs layer deposited onto FTO glass substrate and TiO_2 NTs layer deposited onto Ti plate. A - denotes spectra features for the anatase crystal structure of a TiO_2

photoanode form and the dye structure will be reflected in the MFE response of photocells.

6.1.2 Photovoltaic performance

Figure 6.9 shows J-V curves for all solar cells configurations while in Table 6.1 their performance parameters are presented.

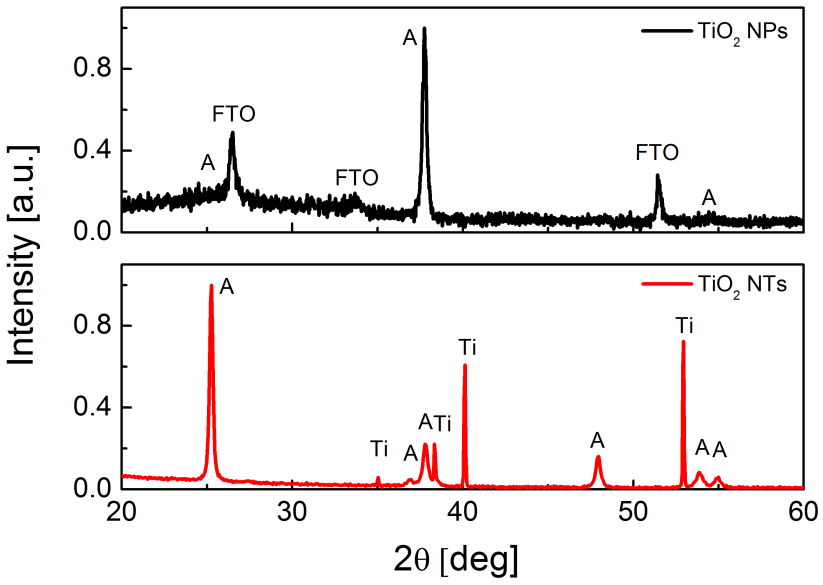

Figure 6.5. XRD patterns of TiO_2 NPs layer deposited onto FTO glass substrate (top) and TiO_2 NTs layer deposited onto Ti plate (bottom). Reflections for the anatase crystal structure, FTO glass substrate and Ti plate are denoted as: A, FTO and Ti, respectively

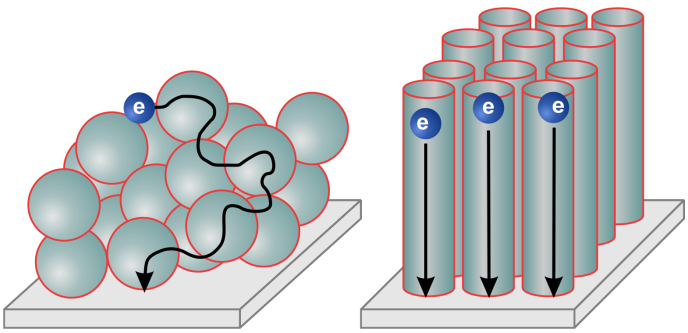

Figure 6.6. Electron diffusion path through TiO_2 nanoparticles (left) and ordered nanotubes (right)

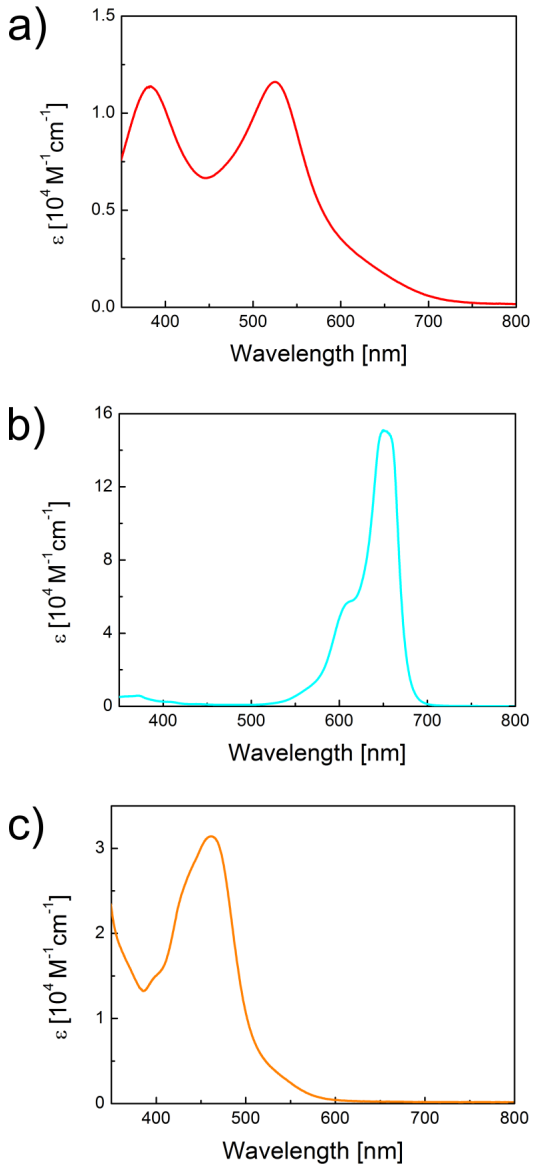

Figure 6.7. Absorption spectra of (a) N719, (b) SQ2 and (c) B1 dyes in ethanol solution

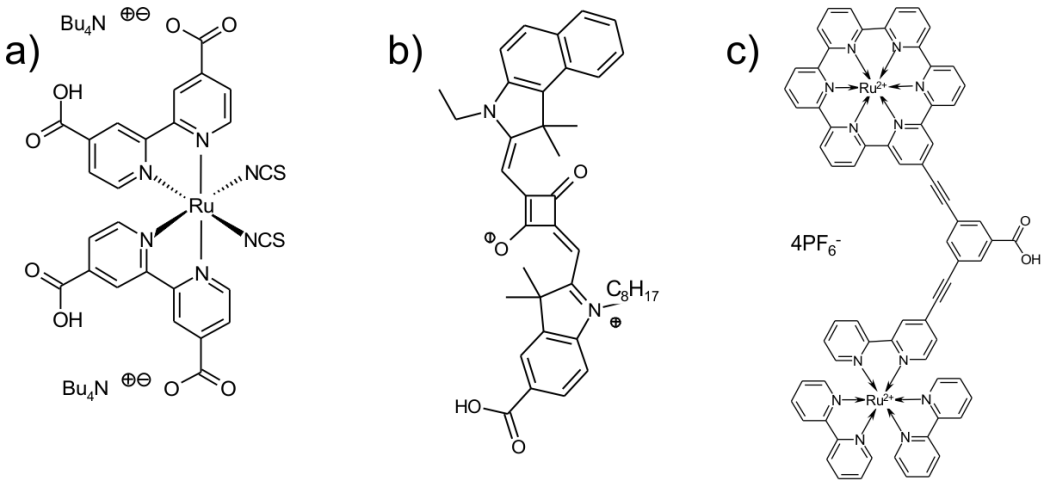

Figure 6.8. Molecular structure of (a) N719, (b) SQ2 and (c) B1 dyes

Table 6.1. Photovoltaic performance of the all dye-sensitized solar cells configurations

Dye	J_{SC} [mA/cm^2]		V_{OC} [V]		FF		PCE [%]	
	NPs	NTs	NPs	NTs	NPs	NTs	NPs	NTs
N719	12.11	6.09	0.662	0.646	0.72	0.64	5.74	2.52
SQ2	4.43	2.32	0.470	0.444	0.65	0.48	1.35	0.50
B1	0.55	0.32	0.505	0.423	0.60	0.36	0.17	0.05

6.1.3 DFT calculations

A significant role in the formation of $(e-h)$ pairs at the interface play adsorption interaction mechanism and the geometry of the dye : semiconductor system. To find possible binding modes for all used dye molecules we have performed DFT computational calculations. Accordingly, a distance between TiO_2 surface and hole localized on highest occupied molecular orbital of an oxidized dye molecule was estimated which is in fact a minimal value of $(e-h)$ pair radius (denoted further as l). Our results show that N719 dye may attach to TiO_2 surface in two ways which results in formation of $(e-h)$ pairs of different l parameters: $l_1 = 750$ pm for binding simultaneously by two protonated carboxylic (opposite thiocyanate ligands) groups and $l_2 = 780$ pm for anchoring by one of two deprotonated carboxylic groups (Fig. 6.10a and 6.10b, respectively). A dinuclear B1 dye adsorbs onto semi-

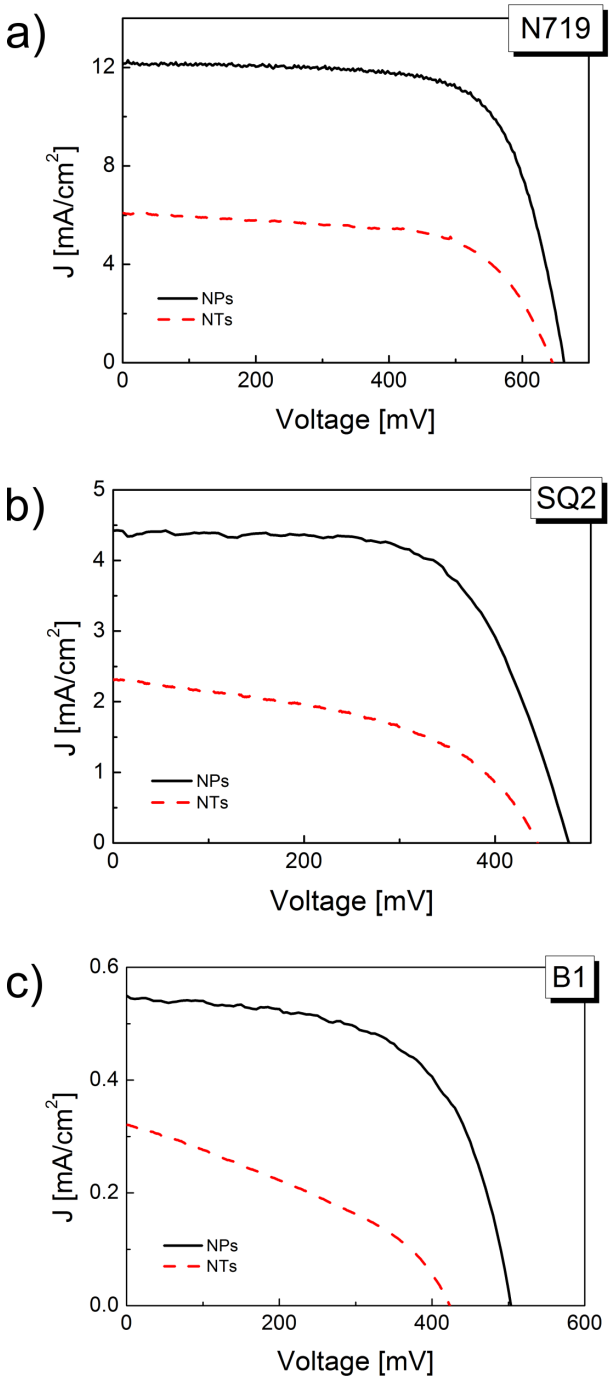

Figure 6.9. Photocurrent density-voltage curves for solar cells sensitized by (a) N719, (b) SQ2 and (c) B1 dye

conductor surface anchoring by a carboxylic benzoate group but it behaves like a pan balance and due to orientational freedom the $(e-h)$ pair parameter ranges from $l_1 = 740$ pm to $l_2 = 1150$ pm (Fig. 6.10d). There is one possible geometrical orientation of SQ2 molecule binding to TiO_2 surface which leads to the formation of $(e-h)$ pairs with a unique minimum radius of $l = 980$ pm (Fig. 6.10c).

6.1.4 Magnetic field effects

To examine the influence of external magnetic field on photocurrent (the MPC signal) we have recorded the short circuit photocurrent as a function of magnetic field strength for six configurations of dye-sensitized solar cells: TiO_2 NPs/N719 and TiO_2 NTs/N719 (Fig. 6.11a), TiO_2 NPs/SQ2 and TiO_2 NTs/SQ2 (Fig. 6.11b), TiO_2 NPs/B1 and TiO_2 NTs/B1 (Fig. 6.11c). The MPC signal data points were calculated from the following formula:

$$MPC = \frac{j_{sc}(B) - j_{sc}(0)}{j_{sc}(0)} \tag{6.1}$$

which represents a relative change of photocurrent with and without magnetic field ($j_{sc}(B)$ and $j_{sc}(0)$, respectively).

Table 6.2. The parameters used for the Lorentzian fitting shown in Fig. 6.11b A_{LFE} and B_{LFE} denote the amplitude and the half width ($B_{\frac{1}{2}}$) at half signal maximum, respectively, for low-field (LFE) and high-field (HFE) effects

Photoanode	A_{LFE} [%]	B_{LFE} [mT]	A_{HFE} [%]	B_{HFE} [mT]
NPs	-0.175	17	-0.22	400
NTs	-0.11	17	-0.28	400

For N719 dye based solar cells we have not observed any MFE within the experimental error of 0.05% whereas for B1 and SQ2 dyes a small negative MFE without saturation at the magnetic field $B = 600$ mT has been clearly observed. For both of them this negative MPC signal decreases when the TiO_2 nanoparticles are replaced by the TiO_2 nanotubes in the photoanode structure. The obtained results summarized in Tab. 6.5 indicate that the photoanode morphological architecture as well as the electronic dye structure affect magnetic field effects in dye-sensitized solar cells. In accordance

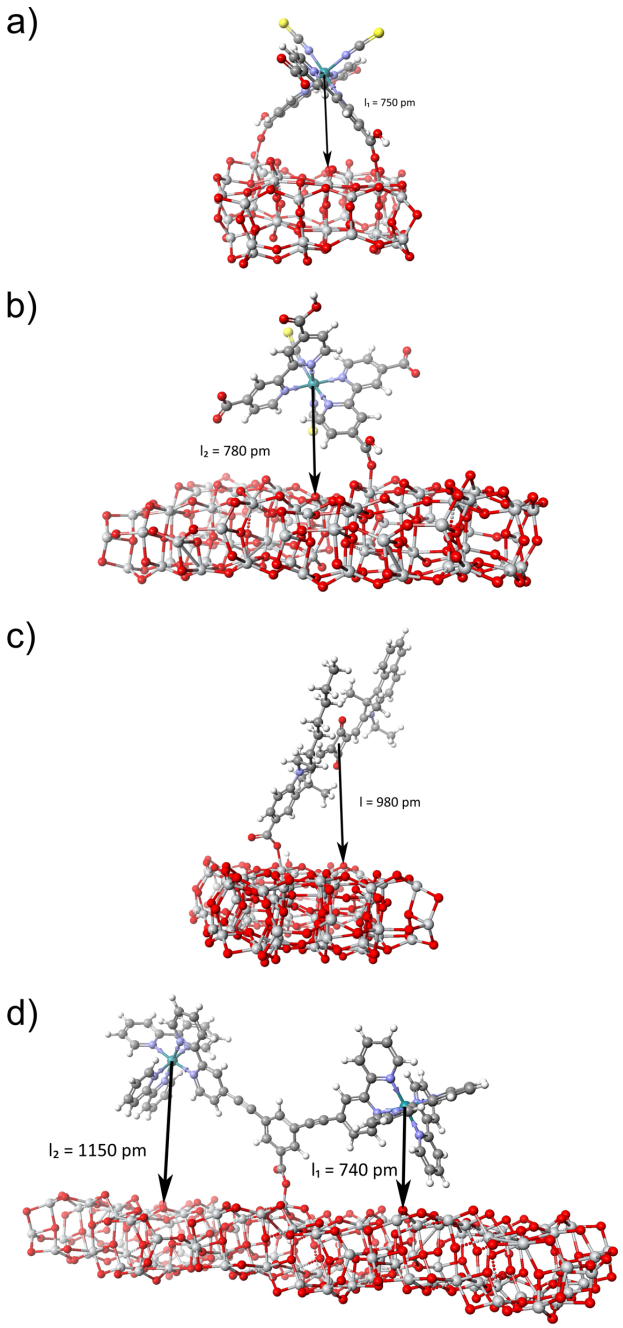

Figure 6.10. Possible binding schemes of (a,b) N719, (c) SQ2 and (d) B1 to surface of anatase TiO_2 cluster with indicated distance between the surface and a central atom (a, b, d) or a geometrical center of a hole localized on a dye molecule (c)

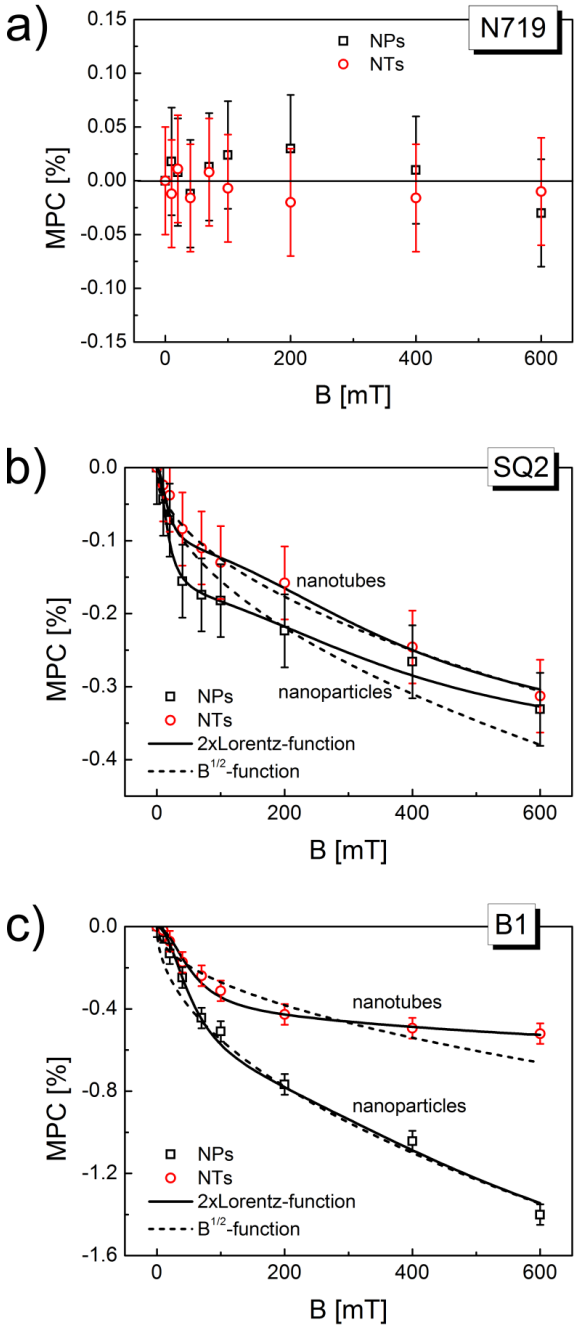

Figure 6.11. Magnetic field effect on photocurrent for DSSCs with nanoparticle/nanotube structure of TiO_2 photoanodes sensitized by (a) N719, (b) SQ2 nad (c) B1 dye. The MPC data points are fitted by Lorentzian function (solid lines, formula 6.2) and $B^{\frac{1}{2}}$ function (dashed lines, formula 6.3). Parameters used for fitting are presented in Tables 6.2 - 6.4

Table 6.3. The parameters used for the Lorentzian fitting shown in Fig. 6.11c A_{LFE} and B_{LFE} denote the amplitude and the half width ($B_{\frac{1}{2}}$) at half signal maximum, respectively, for low-field (LFE) and high-field (HFE) effects

Photoanode	A_{LFE} [%]	B_{LFE} [mT]	A_{HFE} [%]	B_{HFE} [mT]
NPs	-0.7	55	-1.3	600
NTs	-0.44	55	-0.18	600

Table 6.4. The parameters used for the single power function fitting shown in Fig. 6.11

Photoanode	A [$\% T^{-\frac{1}{2}}$]	
	SQ2	B1
NPs	-1.55	-5.5
NTs	-1.25	-2.7

with our expectations the shorter free carrier lifetime in a NT TiO_2 conduction band translates into the shorter $(e-h)$ pair spin coherence time and/or shorter radius, both of them reflecting in lower MPC signals for NT solar cells which suggests that there is a certain balance between these two factors. Furthermore, the predicted increase in a distance between TiO_2 surface and a hole localized on HOMO dye molecule passing from N719 through SQ2 to B1 (Fig. 6.10) translates into the lower exchange interaction energy of $(e-h)$ pairs which reveals in the more negative MFE signals (Fig. 6.11). However, in the case of N719 dye with the highest exchange interaction energy probably the smallest signals could not be distinguished from the background noise. For identifying the spin-mixing mechanism responsible for the observed MFEs the data points in Fig. 6.11 have been fitted with a double-Lorentzian function having the form of

$$MPC = A_{LFE}B^2/(B^2 + B_{LFE}^2) + A_{HFE}B^2/(B^2 + B_{HFE}^2), \tag{6.2}$$

or with a single power function

$$MPC = AB^{\frac{1}{2}}. \tag{6.3}$$

In the relevant components of the formula (6.2) representing the low-field (LFE) and high-field (HFE) effects, A_{LFE} and A_{HFE} parameters de-

Table 6.5. Summary of MFE results for various DSSC configurations

Dye	HOMO hole - TiO_2 surface distance l [pm]	MFE at 100 mT [%]		MFE at 600 mT [%]	
		NPs	NTs	NPs	NTs
N719	750/780	0.00	0.00	0.00	0.00
SQ2	980	-0.18	-0.13	-0.33	-0.30
B1	740-1150	-0.55	-0.31	-1.40	-0.50

note the MPC signal magnitudes for $B \to \infty$, whereas B_{LFE} and B_{HFE} determine the half width ($B_{1/2}$) at half signal maximum (HWHM) [103]. The relatively good fitting based on double-Lorentzian function (solid lines in Fig. 6.11) has been obtained for NP-B1 solar devices with the HWHM equal to $B_{LFE} = 55$ mT and $B_{HFE} = 600$ mT while for NP-SQ2 devices $B_{LFE} = 17$ mT and $B_{HFE} = 400$ mT. Note that the HWHM of the low field component is much broader than hyperfine field in the EHP model, which is typically ≈ 3 mT in organic compounds [36, 68, 103, 104]. Furthermore, the strong spin-orbit coupling in N719 and B1 dyes induced by the high orbital magnetic field of ruthenium atom switches off the hyperfine field-scale effects [68, 105], therefore, HFM spin-mixing mechanism is rather not appropriate here. Another possible alternative of observed MFE could be the T-q model in which a high triplet state concentration is of importance. Even though, for ruthenium dyes this requirement is certainly fulfilled, for a SQ2 dye after visible light absorption based on $\pi \to \pi^\star$ transitions prevailingly singlet excited states are formed due to inefficient ISC [96]. Moreover, in the T-q model the field-induced spin-mixing occurs at magnetic field strength comparable with the ZFS of 80 mT typical values [68, 86] which discards the FSM mechanism as a main origin of the observed high-field (> 100 mT) effects.

To explain the MFE in analyzed solar cells the Δg mechanism could be potentially involved, wherein spin-mixing occurs as a result of different values of Lande factor for electron and hole entities constituting $(e - h)$ pairs. Recently, this mechanism was considered for MPC effect in organic (P3HT:PCBM) photovoltaic cells (Δg is $\approx 10^{-3}$) [68] and for MPC, MPL and MEL in perovskite ($CH_3NH_3Pb_{3-x}Cl_x$) solar cell systems (Δg is ≈ 0.65) [88]. Previous EPR spectroscopy studies of TiO_2 [106, 107] and $Ru(bpy)_3^{2+}$ [108–110] have shown surprisingly different values of Lande factor for Ti^{3+} electron (g_e) and hole $Ru(bpy)_3^{3+}$ (g_h) radicals in comparison to free electron g value $= 2.0023$. It is generally recognized that Ti^{3+} is an electron center

in semiconductor conduction level while on Ru(III) radical, after electron transfer from excited ruthenium dye molecule, a hole is localized. For Ti^{3+} in nanoparticles of anatase structure $g_e = 1.988$, and for a Ru(III) complex radical $g_h = 2.63$, thus for $(e-h)$ pairs created at the photoactive solar cell interface the large value of $\Delta g \approx 0.64$ makes the MFE be controlled by the Δg mechanism as observed recently in perovskite solar cells [88]. The EPR study has shown that the Lande g factor for a hole localized onto the SQ molecule is $g_h = 2.0042$ which makes $\Delta g = 0.0162$ value large as well. Typical Δg values for organic compounds are of the order of 10^{-3} [12, 48, 68, 104, 111].

The low-field and high-field components in the double-Lorentzian function could be in fact assigned to the different relaxation times of $(e-h)$ pairs involved in dissociation/recombination processes which according to formula,

$$\tau = \frac{\hbar}{2\mu_B \Delta g B_{1/2}}, \tag{6.4}$$

are estimated as 162 ps and 15 ps for B1, comparing well with those values received for $(e-h)$ pairs in perovskite devices [88]. Nevertheless, instead of the two discrete spin pair species a broad distribution of decay times is certainly more appropriate here in such highly disordered nanocrystalline TiO_2 photoanodes showing possibly non-exponential (dispersive) relaxation [68] when an ensemble of static pairs in disordered medium is considered. However, based on spin dynamics theory of radical pair diffusion in solution [12] the completely different scenario can be alternatively outlined where relaxation mechanism of $(e-h)$ pairs is dominated by the diffusive motion character of charge carriers (mainly electrons in TiO_2 film). In this case, similarly as in π-conjugated polymer:fullerene blends [112] the high field effects of Δg origin should be modeled by the formula (6.3) [12]. Indeed, the relevant fitting of MPC data in the presence of $(e-h)$ pair diffusion (dashed lines in Fig. 6.11) is only of slightly poorer quality in comparison to the case of static spin pairs in non-diffusive environment.

6.1.5 Mechanism of magnetic effects in DSSCs

Regarding to our present investigation on various dye-sensitized solar cells we consider the following mechanism as a viable reason for the observed MFEs. First we describe mechanism for solar cells with ruthenium based sensitizers depicted in Fig. 6.12a. In this case after absorption of solar radiation by a dye ground state (S_0) a singlet excited state (^1MLCT) as well as a triplet excited state (^3MLCT), as a result of heavy metal atom induced efficient intersystem crossing ($\approx 10^{-12}$ s), is created. The analysis

of kinetic competition between electron injection from singlet excited state (fs-ps), intersystem crossing ($\approx$ 75 fs), triplet state electron injection ($\approx$ 350 ps) and triplet state decay ($\approx$ 10 ns) indicates that the electron injection in N719 sensitized TiO_2 film is dominated by injection from N719 triplet state - (^3MLCT) [55, 56]. Therefore, the injection processes lead mainly to formation of triplet $^3(e-h)$ pairs, where the electron occupies the conduction level of TiO_2 and the hole is localized on a dye molecule. The $(e-h)$ pairs can dissociate into free carriers with k_{-1} and k_{-3} rate constants forming a photocurrent, or recombine with k_1 and k_3 rate constants regenerating a dye ground state, for singlet and triplet pairs, respectively. The mutual relationships between these rate constants are as follows: $k_{-1} < k_{-3}$ due to better dissociation from triplet pairs in such a kind of heavy metal complexes [113] whereas $k_1 > k_3$ due to more efficient spin allowed $^1(e-h) \rightarrow S_0$ recombination than spin protected transition from a triplet pair state, $^3(e-h) \rightarrow S_0$. According to the scheme (Fig. 6.12a) the external magnetic field induces the intersystem crossing in electron-hole pairs (Δg mechanism) which leads to an increase in population of singlet pairs at the expense of triplet pairs. However, the dissociation rate constant from a singlet state is less than that from a triplet state ($k_{-1} < k_{-3}$) while the relevant recombination rate is much greater ($k_1 > k_3$), thus the generated photocurrent decreases as observed.

In the system with fully organic sensitizer the MFE mechanism depicted in Fig. 6.12b is slightly different. This time, due to spin forbidden molecular dye $S_1 \rightarrow T_1$ transition, the photoexcitation of S_1 state is followed by an electron transfer process at picosecond time scale (< 60 ps) resulting in singlet $^1(e-h)$ pairs. Further, the external magnetic field induces ISC from singlet to triplet pair state forming $^3(e-h)$ pairs. We should note here that in the squaraine molecule the singlet-triplet splitting energy is quite large, $\Delta E_{ST} \approx 1$ eV, leading to a low position of the first triplet state, T_1 [97, 98]. Therefore, besides dissociation, recombination pathways of a singlet pair to the dye ground state or a triplet pair to the energetically accessible T_1 state can occur. This long lived T_1 state relaxes to the ground state creating a crucial loss pathway which was recognized as the so-called triplet drain [85, 114]. Thus, in this case the generated photocurrent is limited by population of singlet pairs bearing usually in organic solids higher dissociation ability in comparison to more localized triplet pairs [36, 38, 115].

To conclude, our results show that the photogeneration of free carriers in DSSCs proceeds through $(e-h)$ pair states which play crucial role in subsequent recombination / dissociation processes. For ruthenium-based sensitizers more favorable are triplet states while for fully organic sensitizers with triplet drain this state constitutes the main source of losses. Nevertheless,

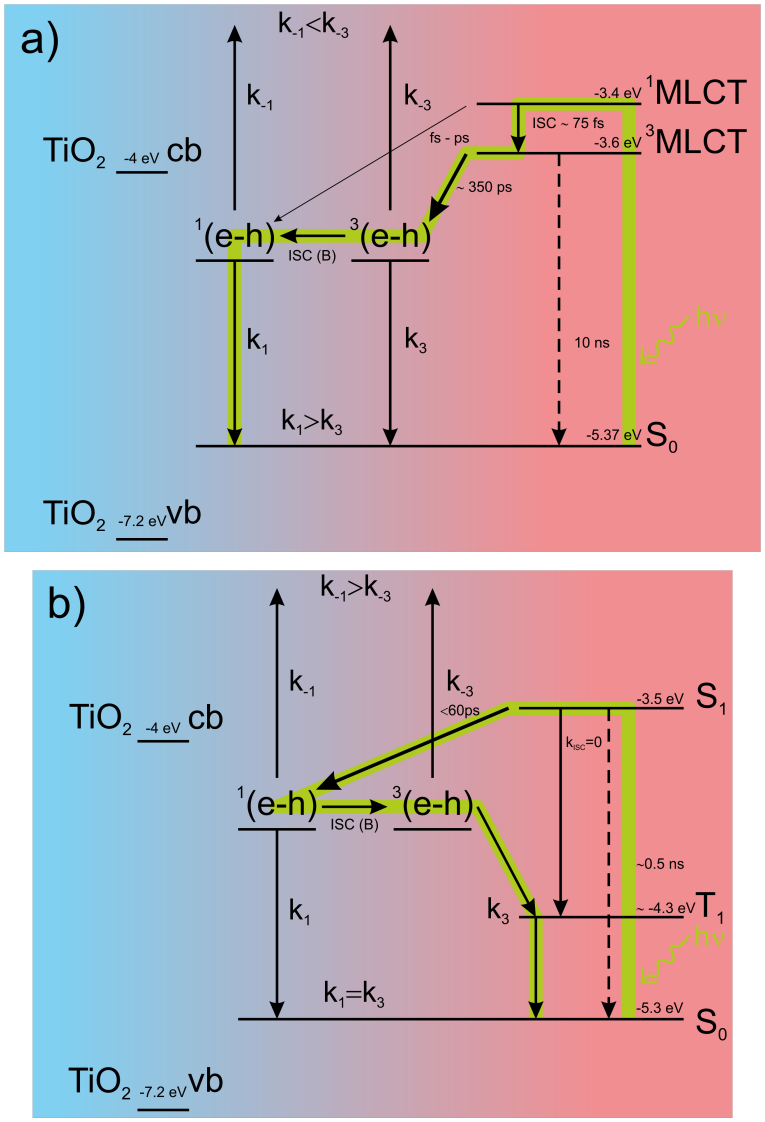

Figure 6.12. The proposed mechanism of electron transfer and charge carrier dissociation for DSSCs with (a) ruthenium N719 or B1 dye and (b) organic SQ2 dye. The time constants indicated in the picture were taken from the literature [55, 96]. The green solid lines are guide to the eyes

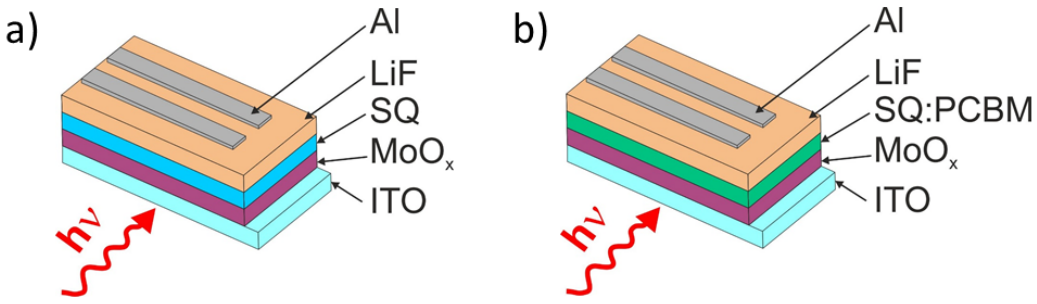

Figure 6.13. Structures of a single-layer (a) and a bulk-heterojunction (b) solar cell

in organic materials with a molecular triplet state lying higher than triplet electron-hole pair energy level dissociation from this $^3(e-h)$ pair can lead to positive MFE (and in fact to an increase in generated photocurrent) as it was observed in P3HT:PCBM organic solar cells [62] or in m-MTDATA:3TPYMB system [85].

6.2 MFEs in organic solar cells

6.2.1 Materials characterization

In this study, we fabricated single-layer solar cells, with a squaraine active layer (Fig. 6.13a), and bulk-heterojunction solar cells (Fig. 6.13b) with blends of SQ (acting as an electron donor and hole conducting material) and $PC_{60}BM$ (acting as an electron acceptor and mainly electron transporting material), with various wt.% donor to acceptor ratios. The chemical structures of the materials applied are shown in Fig. 6.14a, b while the absorption spectra of the spin-coated films of pristine SQ and $PC_{60}BM$, and the SQ:$PC_{60}BM$ (1:6 wt.) blend are depicted in Fig. 6.15. AFM topography scans of thermally evaporated MoO_x thin film and spin-coated SQ or SQ:$PC_{60}BM$ layers are presented in Fig. 6.16.

6.2.2 Photovoltaic performance

Fig. 6.17 displays the photocurrent density-voltage curves of OPV with the SQ and SQ:$PC_{60}BM$ (1:6) active layer under standard test conditions (STC). A great enhancement of photocurrent density (J_{SC}, from 1.1 to 7.3 mA/cm^2) and photoconversion efficiencies (PCE of 0.13% and 1.28% for SQ and SQ:PC60BM (1:6), respectively) is clearly seen, which compares well with SQ2/C60 planar-heterojunction solar cells reported previously for the

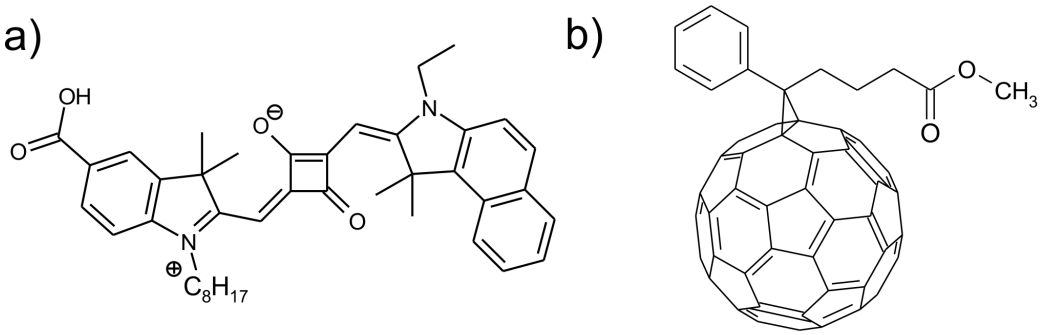

Figure 6.14. Chemical structures of squaraine dye SQ2 (a) and fullerene derivative $PC_{60}BM$ (b)

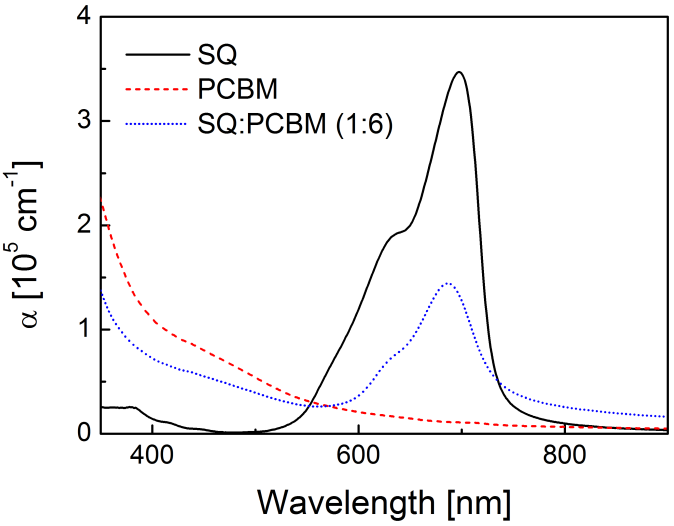

Figure 6.15. Absorption spectra of SQ (solid line), $PC_{60}BM$ (dashed line) and a blend (dotted line) of both materials with SQ to $PC_{60}BM$ 1:6 weight ratio

same type of squaraine molecule [116]. The lower value of V_{OC} for single-layer than for bulk-heterojunction solar cells is likely induced by the low shunt resistance of the thin SQ film subject to possible internal short-circuits. It should be noted that the present OPV devices were not optimized for the best performance being fabricated without any carrier blocking buffer layers (that significantly enhance the cell performance up to 6% [74, 78]) to track and unravel MFEs on as simple as possible photovoltaic systems.

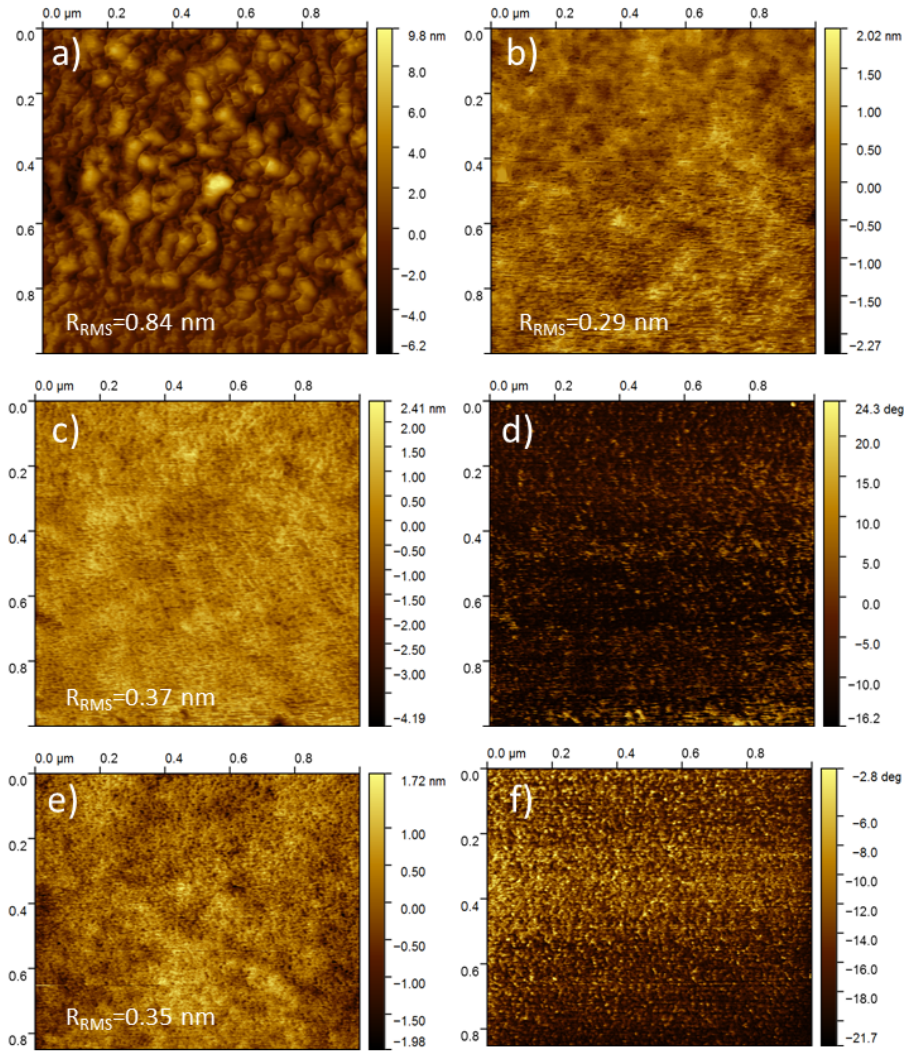

Figure 6.16. AFM topography scans of thermally evaporated MoO_x thin film (a) and spin-coated: pristine SQ (b), SQ:PC_{60}BM 1:10% (c) and SQ:PC_{60}BM 1:6 (e) thin films. R_{RMS} values represent root mean square surface roughness measured across the scan. Phase separation images of spin-coated SQ:PC_{60}BM 1:10% (d) and SQ:PC_{60}BM 1:6 (f) thin films

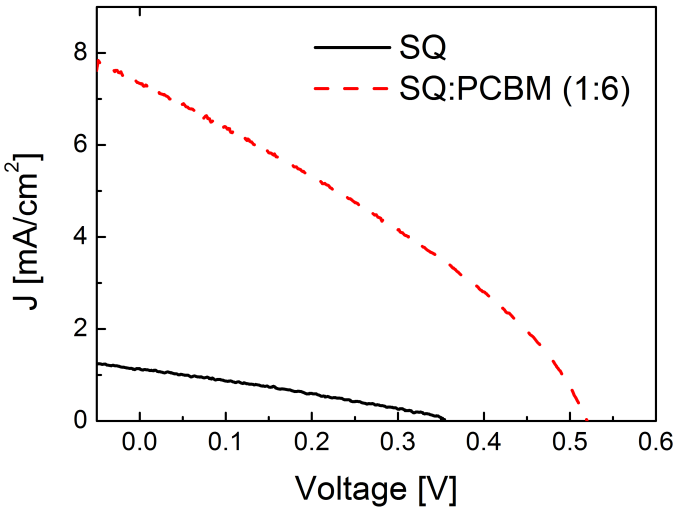

Figure 6.17. The photocurrent density-voltage curves for solar cells with a SQ (solid line) and SQ:$PC_{60}BM$ 1:6 weight ratio (dashed line) active layer

6.2.3 Magnetic field effects

In the following sections, the MFE technique is applied to examine the exciton dissociation and charge carriers recombination processes in systems under investigation. The MPC(B) response is given by

$$MPC(B) = \frac{j(B) - j(0)}{j(0)}, \tag{6.5}$$

where the respective terms represent photocurrent with and without magnetic field ($j(B)$ and $j(0)$, respectively). For identifying the spin-mixing mechanism involved in the origin of MPC signals the data points have been fitted with a double-Lorentzian function (see formula 6.2) or a single-Lorentzian function having the form of

$$MPC(B) = A_{LFE}B^2/(B^2 + B^2_{LFE}). \tag{6.6}$$

Finally, we discuss possible routes of photophysical processes responsible for the observed MFEs.

6.2.4 MFEs in squaraine single-layer solar cells

The magnetic field effects on photocurrent (the MPC signal) recorded as a function of the external magnetic field strength for two different temperatures in a sandwiched configuration, ITO/MoO_x/SQ/LiF/Al, for the

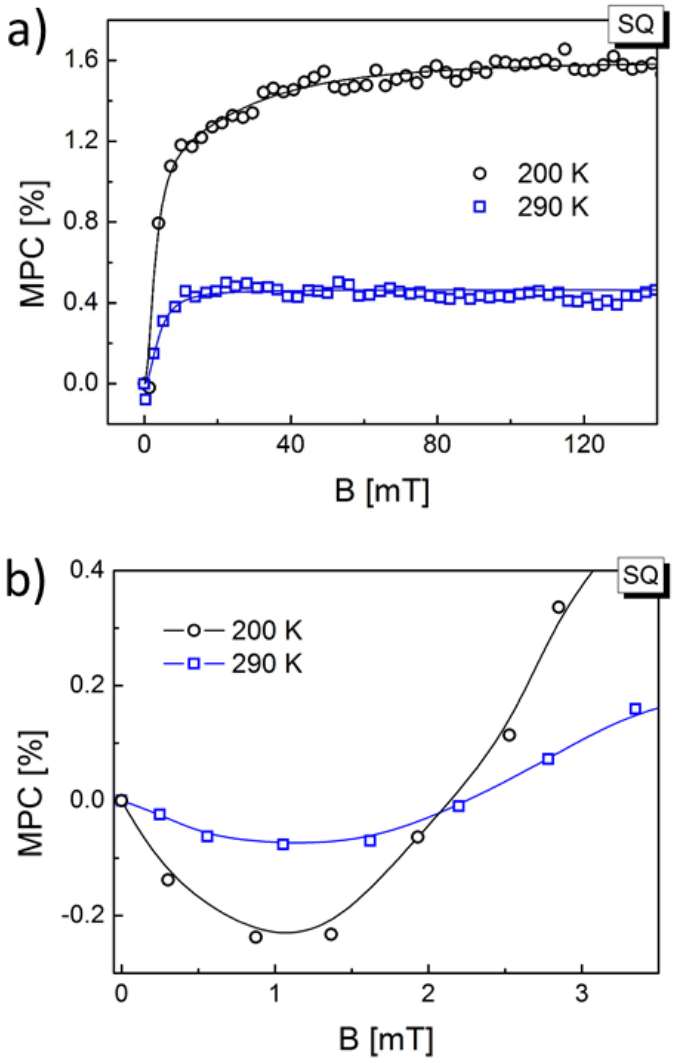

Figure 6.18. The magnetic field effect on the photocurrent for single-layer solar cells. The MPC signal as a function of magnetic field strength for two different temperatures: 200 K (circles) and 290 K (squares) in the low (0-140 mT) and ultrasmall (0-3 mT) field range are displayed in parts (a) and (b), respectively. The solid lines in part (a) represent the best fit according to the single- and double-Lorentzian functions for 290 and 200 K, respectively. Values of the relevant parameters used for fitting are collected in Tab. 6.6. The solid line in part (b) is a guide to the eye

Table 6.6. The parameters used for the Lorentzian fitting shown in Fig. 6.18a. A_{LFE} and B_{LFE} denote the amplitude and the half width ($B_{\frac{1}{2}}$) at half signal maximum, respectively, for low-field (LFE) and medium-field (MFE) effects

Temperature [K]	A_{LFE} [%]	B_{LFE} [mT]	A_{MFE} [%]	B_{MFE} [mT]
200	1.2	3	1.2	30
290	0.465	4	-	-

low-field and the ultrasmall-field regime have been depicted in Fig. 6.18a and Fig. 6.18b, respectively. At room temperature (290 K), the MPC signal saturates on a magnetic field scale characteristic of hyperfine interactions ($B_{LFE} = 4$ mT) while at lower temperature (200 K), besides the low-field component ($B_{LFE} = 3$ mT), the medium-field component ($B_{MFE} = 30$ mT) also appears (Fig. 6.18a). Thus, at 290 K, according to the electron-hole pair model [12, 36, 38, 50, 117], the external magnetic field suppresses the spin-mixing occurring at a hyperfine-field scale and consequently increases the singlet, $^1(e-h)$, to triplet, $^3(e-h)$, electron-hole pair (polaron pair) population ratio in a squaraine material. At reduced temperature, gradually increased population of triplets begins to play a more important role due to the deactivation of radiationless decay pathways. Therefore, at 200 K, besides the low-field effect (induced by HFM), another mechanism likely associated with the fine structure modulation becomes active at a higher magnetic field. When the external magnetic field competes with the internal (fine) magnetic field of electronic spin origin, it starts to modulate the molecular triplet (T) zero-field splitting and thus changes the free carrier mobility. This triplet-charge interaction mechanism (T-q) called trion model can be adopted here. Accordingly, the doublet and quartet trions are formed by the interaction between free charge carriers and triplet molecular excitons (presumably trapped in defect sites of an organic solid) populated in the SQ layer. In the FSM-scale magnetic field of the several-tens-of-mT, the population of the quartet trions is reduced whereas the population of the doublet trions increases. This leads to the lower contribution of the quartet trions and, simultaneously, higher contribution of the doublet trions to the overall scattering process. One, therefore, should observe the increase in photoconductivity of an organic solid due to increasing mobility of charge carriers which is the case in Fig. 6.18a. Another issue which we would like to explain is the amplitude enhancement of the low-field component due to temperature

reduction. Nevertheless, first we shall note that the external magnetic field can change the intersystem crossing rate in electron-hole pair intermolecular states (ISC_{eh}) but has little influence on this rate in intramolecular excitonic states (ISC_{ST}) with a larger singlet-triplet splitting energy [118]. Therefore, on the one hand an increase in the amplitude of the MPC signal originated from carrier scattering on molecular triplets can be induced by the low magnetic field associated with the HFM mechanism, namely, the external magnetic field operating on hyperfine scale reduces the population of T excitons formed from $^3(e-h)$ states thereby enhancing the mobility of free charge carriers. However, on the other hand another explanation of the amplitude change, which is in good agreement with the other results presented later in the text, is also possible. If we assume that the charge carrier hopping frequency (ω_{hop}) is on the order of hyperfine field precession frequency (ω_{hf}), i.e. $\omega_{hf}/\omega_{hop} \approx 1$ (intermediate-hopping regime), then reducing the temperature, and thereby also reducing the hopping frequency, will be reflected in an increase in the MPC signal amplitude and a decrease in its linewidth [104]. Indeed, a slight change in the width of a low-field Lorentz component with temperature reduction, from $B_{LFE} = 4$ mT to $B_{LFE} = 3$ mT, has been observed. Nevertheless, it may be also associated with the reduction of the broadly distributed decay times of $(e-h)$ pairs in such disordered materials as those used in OPV cells [68].

Let us now take a closer look at the 0-3 mT magnetic field strength range (Figure 6.18b). The ultrasmall magnetic field effect (USMFE), with the opposite sign to the low-field effect can be easily recognized. This intrinsic effect in OMAR according to semiclassical approach proposed by Koopmans and co-workers [104] originates from the competition between spin mixing and exciton formation for intermediate-hopping rates. On the other hand, to investigate the observed MPC line shapes, Vardeny and co-workers [119] applied a fully quantum-mechanical approach in which the polaron pair spin Hamiltonian includes the hyperfine interaction between each of the polaron pair constituents and one or more strongly coupled neighboring nuclei. Therefore, the existing singlet-triplet (S-T) level-crossing (LC) of $(e-h)$ pair states gives rise to excess spin intermixing between hyperfine-split spin sublevels. The external magnetic field (of ultrasmall magnitude) can change the S-T intermixing rate provided by the hyperfine interaction and this way perturb the overall relative steady state populations of the spin sublevels. The authors found that the amplitude of USMFE increases with increasing temperature with the linewidth remaining unaffected. The quantitative description of temperature dependencies, however, is lacking in that study. According to our findings, the observed ultrasmall effect is rather determined by the carrier hopping process, which is in good agreement with the modeling results

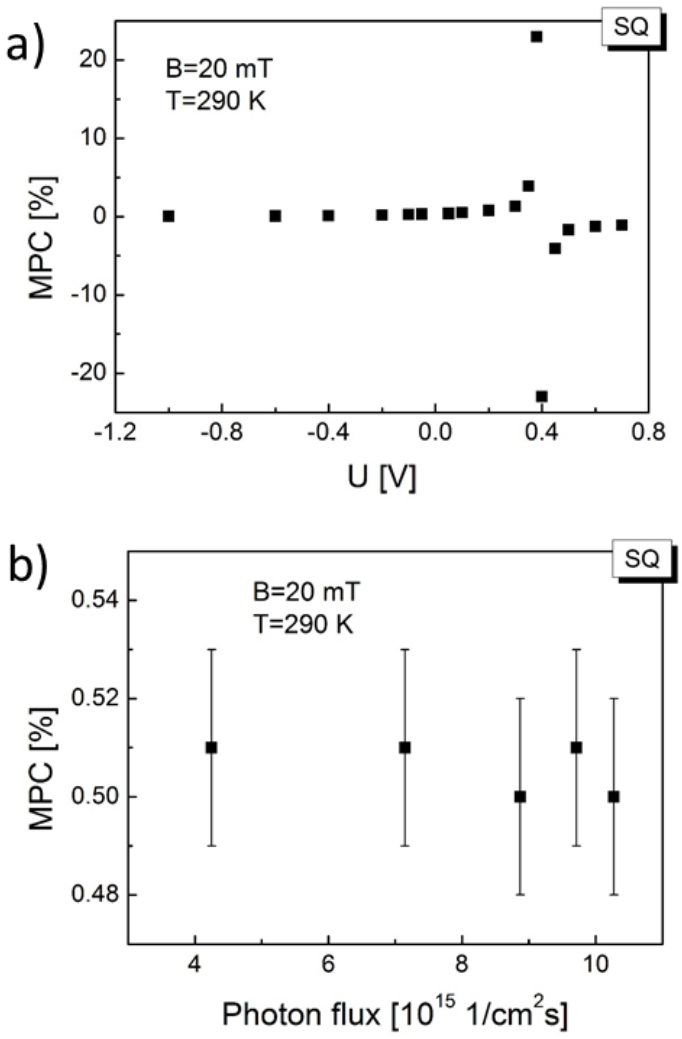

Figure 6.19. The MPC signal versus: forward and reverse bias voltage (a), and photon flux (d) at 20 mT - magnetic field and 290 K

of the Koopmans group [104]. With increasing temperature, the hopping frequency (ω_{hop}) increases, as a result a decrease in the MPC magnitude and an increase in the linewidth are consistently observed.

The MPC signal, measured at 290 K and 20 mT magnetic field strength as a function of forward and reverse bias voltage is depicted in Fig. 6.19a. At a bias voltage below (above) V_{OC}, the magnetic field effect is positive (negative) and shows a weak dependence on the applied voltages while at voltages close to V_{OC}, large values of MFE and a change of sign occur. A similar MFE on photocurrent in P3HT:PCBM bulk-heterojunction solar cells has been reported by Shakya *et al.* [62] and Lei *et al.* [120]. A great enhancement of

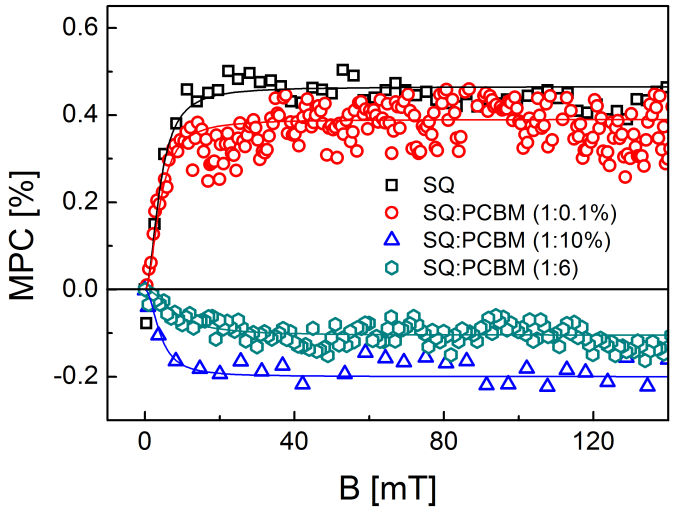

Figure 6.20. The magnetic field effect on the photocurrent for bulk-heterojunction solar cells. The MPC signal as a function of magnetic field strength for various SQ to $PC_{60}BM$ weight ratios at 290 K. The solid lines represent fit according to the single- and double-Lorentzian functions. The values of parameters used for fitting are presented in Tab. 6.7

the magnitude of the MPC signals at bias voltages around V_{OC} appears due to vanishing $j(0)$ (in the formula (6.5) as the bias voltage approaches V_{OC}. Moreover, we note that no mutual exciton-exciton interactions occur in the SQ layer as the photocurrents are proportional to the light intensities used in our measurements and therefore the MPC signals do not depend on the incident photon flux (see Fig. 6.19b).

6.2.5 MFEs in squaraine:fullerene bulk-heterojuntion solar cells

The dependence of MFEs as a function of fullerene concentration in SQ:$PC_{60}BM$ bulk-heterojunction solar cells has been investigated (Fig. 6.20). It can be seen that even a small amount of $PC_{60}BM$ (0.1 wt.%) results in a decrease of a positive low-field component (B_{LFE} = 4 mT) which indicates that $PC_{60}BM$ effectively quenches excitons in SQ layer. Further, the increase in fullerene concentration (up to 10 wt.%) leads to the formation of CT states (where the electron resides on the $PC_{60}BM$ and the hole occupies the SQ molecule) which are lower in energy then $(e-h)$ pair states as well as singlet and triplet molecular states of both SQ and $PC_{60}BM$ (cf. Fig. 6.24). The MPC signal with only the low-field component ($B_{LFE} = 4$ mT), similar to the pristine SQ devices, can be easily explained by the EHP model. The

Table 6.7. The parameters used for the Lorentzian fitting shown in Fig. 6.20. A_{LFE} and B_{LFE} denote the amplitude and the half width ($B_{\frac{1}{2}}$) at half signal maximum, respectively, for low-field (LFE) effects

Active layer	A_{LFE} [%]	B_{LFE} [mT]
SQ	0.465	4
SQ:PCBM (1:0.1%)	0.39	4
SQ:PCBM (1:10%)	-0.2	4
SQ:PCBM (1:6)	-0.105	8

sign change (from positive to negative), however, indicates that the dissociation of the electronic excited states proceeds this time *via* the *CT* states and consequently the magnetic field dependent intersystem crossing in *CT* states (ISC_{CT}) plays a crucial role. Further doping the SQ with $PC_{60}BM$ (up to 1:6 SQ to fullerene wt. ratio) reduces the magnitude of the low-field (B_{LFE} = 8 mT) negative MPC signal. In polymer:fullerene blends with such a high $PC_{60}BM$ concentration, phase separation usually occurs [86, 99]; then the corresponding MPC signal may be ascribed to the bipolaron mechanism [53] wherein HFM in charge carrier pairs with the same signs ($e-e$ in $PC_{60}BM$) occurs. However, the atomic force microscopy analysis of SQ:$PC_{60}BM$ blends indicates that fullerene is still homogeneously distributed throughout the squaraine (Fig. 6.16). Therefore, the bipolaron model operating in $PC_{60}BM$ domains may be safely neglected. We believe that here hyperfine spin mixing in *CT* states (EHP model) is still valid while the decrease of the MPC signal, in comparison to the small $PC_{60}BM$ concentration system (10 wt.% $PC_{60}BM$), is associated with reduction in the amount of active SQ:$PC_{60}BM$ interfaces.

The half-width of magnetic field dependence of the MPC signal for samples with a high $PC_{60}BM$ content should be essentially lower than that in pristine SQ due to the vanishing nuclear magnetic moment of ^{12}C as reported for the MDMO-PPV:$PC_{60}BM$ system [86]. Although in our investigation a completely opposite behavior (B_{LFE} = 8 mT and B_{LFE} = 4 mT for blends and pristine SQ, respectively) is observed, this finding corroborates our previous assignment of carrier hopping frequency to the intermediate regime ($\omega_{hop} \approx \omega_{hf}$). Then, the MPC linewidths are determined not only by the hyperfine field but also by the lifetimes of diffusively moving ($e-h$) pairs in

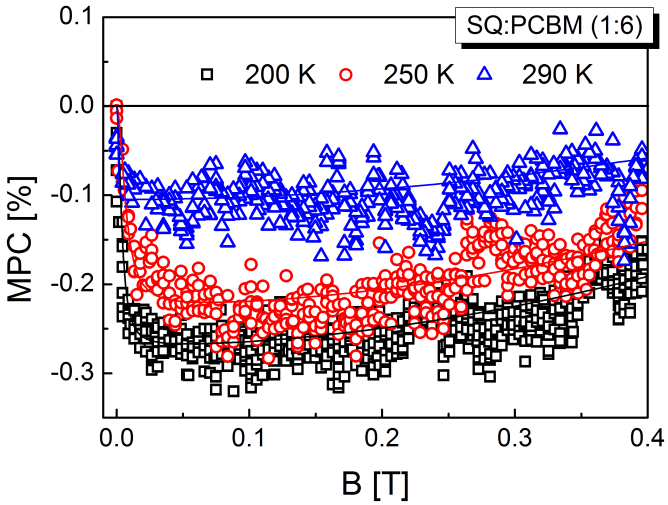

Figure 6.21. The magnetic field effect on the photocurrent for bulk-heterojunction solar cells. The MPC signals for SQ:$PC_{60}BM$ 1:6 wt. in the medium (0-400 mT) field range for various temperatures are shown. The solid lines represent fit according to the single- for LFE and double-Lorentzian functions for HFE range. The values of relevant parameters used for fitting are displayed in Tab. 6.8

Table 6.8. The parameters used for the Lorentzian fitting shown in Fig. 6.21 and Fig. 6.22a. A_{LFE} and B_{LFE} denote the amplitude and the half width ($B_{\frac{1}{2}}$) at half signal maximum for low-field effect (LFE) according to the single-Lorentzian function. A_{HFE} and B_{HFE} denote the amplitude and the half width ($B_{\frac{1}{2}}$) at half signal maximum for high-field effect (HFE) according to the double-Lorentzian functions

Temperature [K]	A_{LFE} [%]	B_{LFE} [mT]	A_{HFE1} [%]	B_{HFE1} [T]	A_{HFE2} [%]	B_{HFE2} [T]
200	-0.27	4	1.7	1.4	5	20
250	-0.225	7	1.2	1.6	5.5	15
290	-0.105	8	1.1	2	5.5	15

a solid environment exhibiting various types of structural disorder [104].

In the following section, we focus on the SQ:$PC_{60}BM$ 1:6 wt. ratio system for which the highest photoconversion efficiency has been reported so far. The negative MPC signal recorded at various temperatures (200, 250 and 290 K) saturates at the low-field scale and remains constant until about

Table 6.9. The parameters used for the KWW fitting shown in Fig. 6.22b. τ represent an average relaxation time of CT states and α is the dispersive parameter

Temperature [K]	α [-]	τ [ns]
200	0.51	1.88
250	0.5	1.02
290	0.61	0.57

200 mT. Above 200 mT, the absolute MPC value starts to decrease and at about 600 mT, the signal changes the sign (Fig. 6.21 and Fig. 6.22). With increase in the magnetic field strength the positive high-field component, rather weakly affected by the temperature, increases and does not saturate up to 9 T. Moreover, upon reducing the temperature the amplitude of the low-field negative component increases and its linewidth decreases ($B_{LFE} = 8$ mT and $B_{LFE} = 4$ mT for 290 and 200 K, respectively) which once again emphasizes the substantial influence of the thermally activated hopping frequency on the MPC signals (Fig.6.21).

In order to clarify the origin of the high-field component we have measured the Lande g factor for a hole (g_h) localized onto the SQ2 molecule by electron paramagnetic resonance (Fig. 5.3) and compared it with the g factor value taken from the literature for an electron (g_e) placed on a $PC_{60}BM$ cage [121]. It was found that $g_h = 2.0042$ and $g_e = 1.9996$, leading to $\Delta g = 0.0046$. The presence of only a positive MPC signal in the high magnetic field range and a difference in Lande factors of the order of 10^{-3} indicate that the so called Δg mechanism may be potentially involved as similarly considered for the MPC effect in P3HT:$PC_{60}BM$ photovoltaic cells ($\Delta g = 0.002$) [68]. In the EHP model a difference in precession frequency ($\Delta\omega_p$) can be induced not only by a difference in the local (of hyperfine origin) magnetic fields (ΔB) experienced by electron and hole entities forming $(e - h)$ pairs ($\Delta\omega_p = g\mu_B\Delta B/\hbar$) but also by a difference in g factors ($\Delta\omega_p = \Delta g\mu_B B/\hbar$), where B is the applied field strength. Therefore, in the Δg mechanism the applied magnetic field enhances the intersystem crossing (ISC_{CT}) between the singlet and $m_s = 0$ triplet CT states and hence the corresponding MPC signal has a sign opposite to the LFE induced by HFM [104]. The characteristic lack of pronounced temperature dependence of the high-field component amplitude is a natural consequence of the spin precession - carrier hopping frequency interrelation when the external magnetic field of

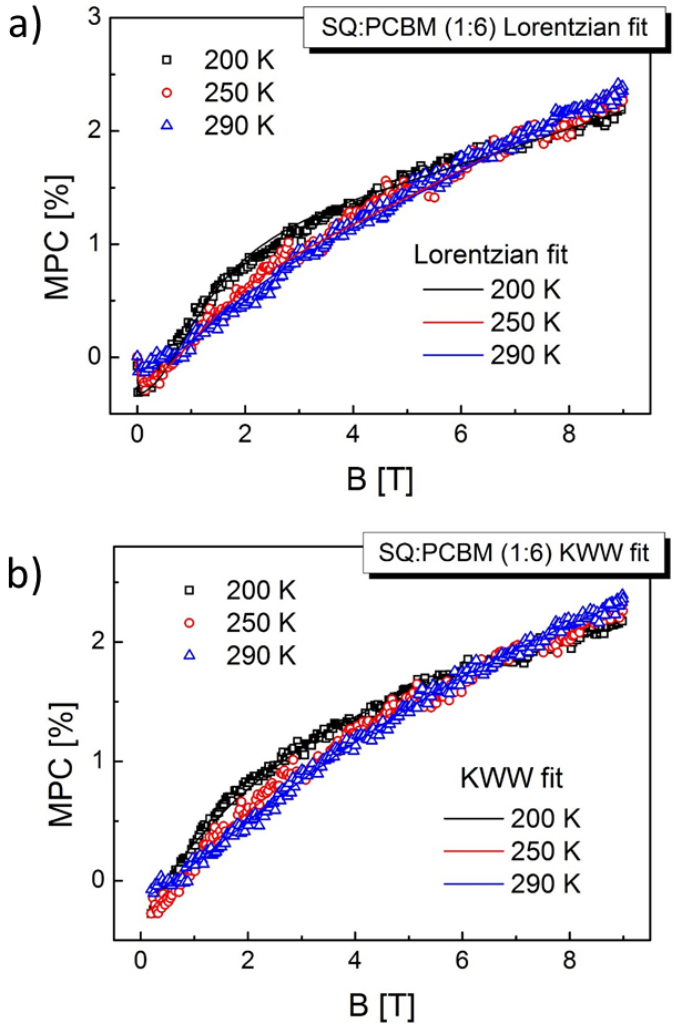

Figure 6.22. The magnetic field effect on the photocurrent for SQ:$PC_{60}BM$ 1:6 bulk-heterojunction solar cells. The MPC signals as a function of magnetic field strength for various temperatures are displayed. In part (a) the low-field negative component is approximated using a single-Lorentzian function and the high-field positive component - using a double-Lorentzian function (solid lines). For comparison, in part (b) the best fit of the high-field component applying the dispersive relaxation model is shown. The values of relevant parameters used for fitting are depicted in Tables 6.8 - 6.9

the order of several tesla enhances significantly the spin precession frequency, ω_p. Therefore, in this regime the precession frequency is definitely greater than the charge carrier hopping frequency ($\omega_p \gg \omega_{hop}$); hence a temperature induced change in hopping rate has no noticeable effect on the MPC signal (Fig. 6.22a). This outcome is significantly different from the results reported for the P3HT:PC_{60}BM devices where the signals are strongly temperature dependent [68, 122]. To better rationalize the role of CT states in dissociation/recombination decay process, the MPC data at various temperatures were fitted by the Lorentzian functions by means of formulas (6.2) and (6.6). Reasonably good fits in the high magnetic field range were obtained using the double-Lorentzian function. According to the formula 6.4 the CT states relaxation times for 290 K are estimated to be 0.82 ns and 0.06 ns. Nevertheless, a more appropriate approach should take into account a distribution of relaxation times. It was shown that for a non-exponential (dispersive) relaxation processes the Lorentzian factor, $Re[1/(1+i\omega_p\tau)]$, may be replaced by the Cole-Cole function, $Re[1/(1+i\omega_p\tau)^{\alpha}]$, where Re denotes the real part, τ represents an average relaxation time and $\alpha \leq 1$ is the dispersive parameter [68, 123]. This can be equivalently interpreted in terms of the Kohlrausch-Williams-Watts (KWW) function, the so-called stretched exponential decay, $exp(-t/\tau)^{\beta}$ with the dispersive β parameter approximately equal to the α parameter from Cole-Cole formula (according to ref. [124] $\alpha \approx \beta^{1.23}$). The respective fit depicted in Figure 6.22b gives $\alpha \approx 0.5$ for temperatures 200-290 K which indicates a 3D random distribution of CT state decay times [19]. The rather weak dependence of MPC signals with temperature increase results from a gradual decrease in relaxation time (from $\tau = 1.88$ ns for 200 K to $\tau = 0.57$ ns for 290 K) due to enhancement of all non-radiative decay pathways of CT states including dissociation and geminate recombination processes.

At a high magnetic field, besides the Δg mechanism, the thermal spin polarization associated with magnetic field dependence of formation probabilities of the singlet and triplet states populated according to the Boltzmann statistics may be also effective. Therefore the spin statistics of the CT states can be substantially controlled by spin-polarizing carriers using high magnetic fields and low temperatures, where the Zeeman energy is comparable with the thermal energy [125]. Therefore, we can calculate the relevant polarizing parameter $b = g\mu_B B/k_B T$ (where k_B is the Boltzmann constant) which gives the maximum spin polarization contribution to the MPC signal as high as $b^2/4 \approx 0.09\%$ (for $g = 2$, $B = 9$ T and $T = 200$ K). Hence, comparing this value to the experimentally obtained MPC $\approx 2.2\%$ at $B = 9$ T we can safely neglect spin polarization effects in our considerations. However, this mechanism might be of importance at cryogenic temperatures [122, 125].

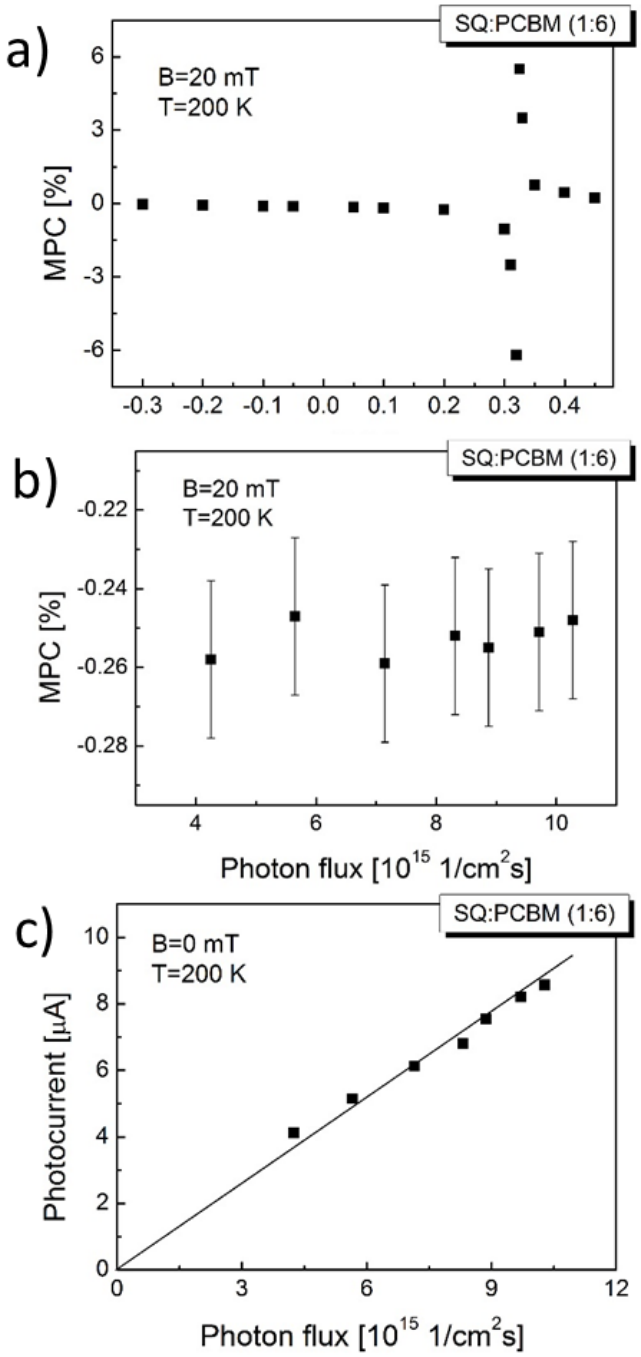

Figure 6.23. The magnetic field effect on photocurrent for bulk-heterojunction solar cells. The MPC signal for SQ:$PC_{60}BM$ 1:6 wt. versus: forward and reverse bias voltage (a), and photon flux (b) at 20 mT and 200 K. In part (c) the light intensity dependence of the photocurrent is displayed - the solid line represents a linear fit

The MPC signals, just like in the case of single-layer solar cells, do not depend on the incident photon flux and again significantly increase and change the sign at the bias voltage around V_{OC} (Fig. 6.23b and Fig. 6.23a, respectively). Moreover, the photocurrent intensity is a linear function of the photon flux (Fig. 6.23c).

6.2.6 Mechanism of magnetic field effects in organic SQ-based solar cells

We consider the following mechanism for explaining the observed magnetic field effects on photocurrent in the investigated squaraine:fullerene systems. According to the scheme based on the commonly applied EHP model, the current generation under SQ photoexcitation in single-layer solar cells (Fig. 6.24a) proceeds through an intermediate state of $(e-h)$ pairs. The initially formed $^1(e-h)$ pairs are quasi-degenerate in energy with $^3(e-h)$ pairs due to the relatively weak electrostatic exchange interactions at a larger distance between electron and hole entities compared to that within the molecular (Frenkel type) exciton states. It has been established that singlet/triplet states of $(e-h)$ pairs (or polaron pairs) can be mixed with each other by hyperfine interactions. When the external magnetic field greater than the hyperfine coupling strength is applied, the Zeeman splitting of triplet states removes degeneracy between $m_s = \pm 1$ triplet and singlet states, and thus suppresses $^1(e-h) \rightarrow ^3(e-h)$ intersystem crossing increasing the population of $^1(e-h)$ pairs. In single component organic solids the dissociation rates $(k_{-1}; k_{-3})$ differ due to the fact that the singlet pair state has a stronger ionic character than triplets and therefore singlet pair states are more strongly coupled with the ionic reaction products of the separated holes and electrons [115], and consequently, to explain MFEs consistently, the $k_{-1} > k_{-3}$ relation is usually assumed [36, 38]. In addition, the lower-energy molecular triplet exciton states (operating here as the 'triplet drain' [85]) open an efficient recombination pathway for $^3(e-h)$ pairs, and this way limit the photocurrent. Further, for MFEs the Lorentzian shape with $B_{1/2}$ width of the hyperfine scale is adequate here (cf. Fig. 6.18a) as shown by the quantum mechanical calculations based on Hamiltonian containing the electronic Zeeman interaction with the external magnetic field and the hyperfine interaction between a single electronic and nuclear dipole [126].

On the other hand, in bulk-heterojunction solar cells, the excited SQ singlet molecular excitons are effectively quenched into ^1CT states. Intersystem crossing between singlet and triplet CT states results in the formation of long-lived ^3CT states which are spin-protected from recombination to the ground

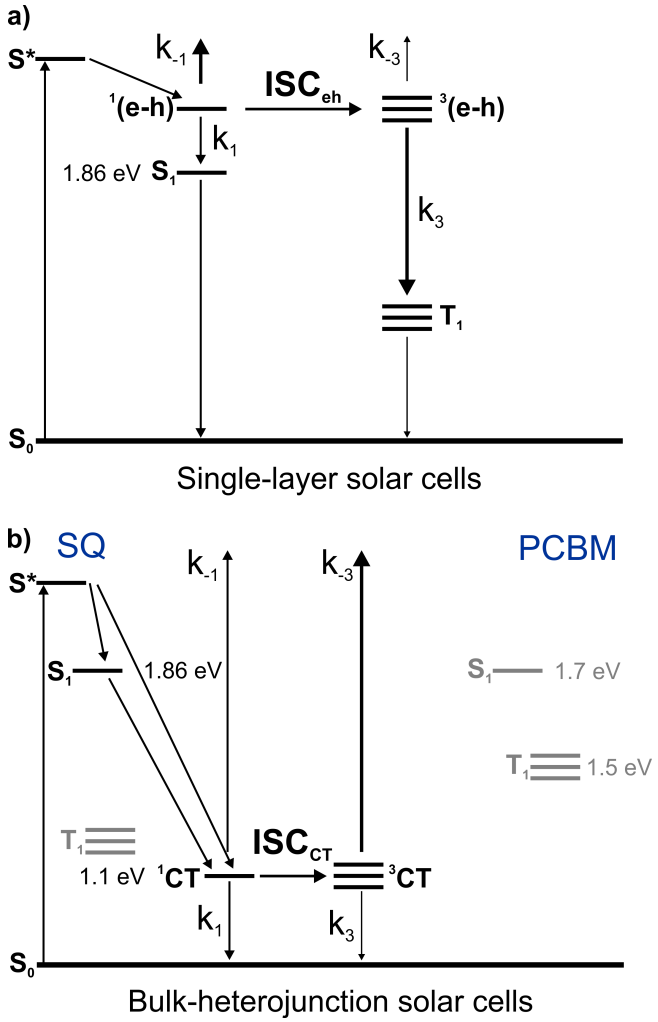

Figure 6.24. Energy diagram of the relevant excited states involved in the photocurrent generation (k_{-1} and k_{-3} reaction rate constants) and charge carrier recombination (k_1 and k_3 reaction rate constants) processes for single-layer (a) and bulk-heterojunction (b) solar cells

state due to energetically inaccessible higher lying triplet molecular excitonic states of both squaraine and fullerene molecules (Fig. 6.24b). Contrary to the single component, in electron donor-electron acceptor systems with such energy levels alignment the ^3CT dissociation channel is decisive in the photocurrent generation process, as recently reported for similar photovoltaic systems [62]. Accordingly, the long-lived triplet CT states exhibit a reduced geminate recombination rate and thus enhanced dissociation ability into free charge carriers in P3HT:PCBM devices. Moreover, a comprehensive investigation on the m-MTDATA:3TPYMB system including the direct measure-

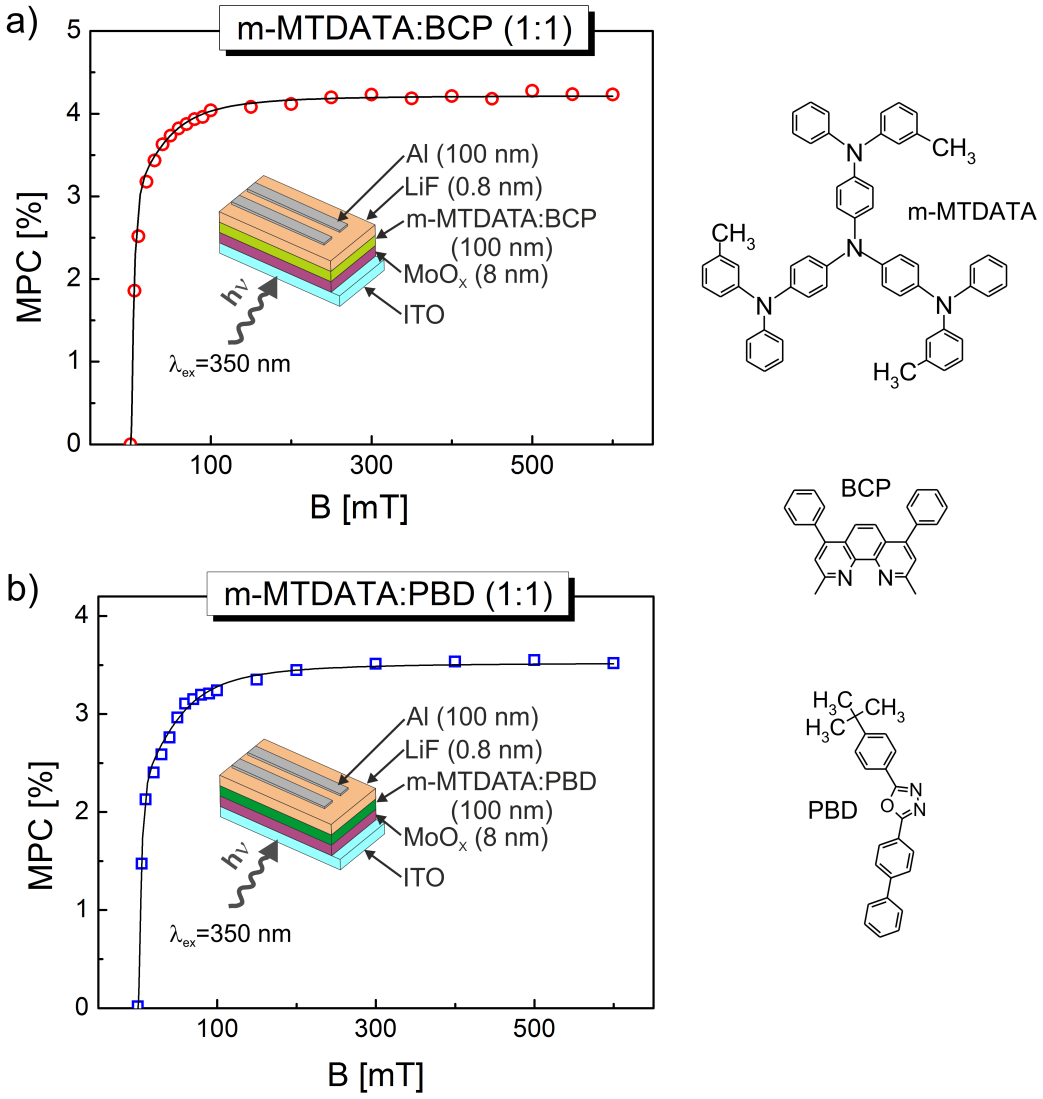

Figure 6.25. The magnetic field effect on the photocurrent (MPC) for bulk-heterojunction solar cells with (a) m-MTDATA:BCP (1:1 wt.) and (b) m-MTDATA:PBD (1:1 wt.) active layer. In the inset structures of solar cells are presented. The solid lines represent the best fit according to the double-Lorentzian function. Fitting parameters are as follows: (a) $A_{LFE} = 3.3\%$, $B_{LFE} = 4\ mT$, $A_{HFE} = 0.92\%$, $B_{HFE} = 50\ mT$, (b) $A_{LFE} = 2.5\%$, $B_{LFE} = 4\ mT$, $A_{HFE} = 1.02\%$, $B_{HFE} = 55\ mT$. The excitation wavelength was set to 350 nm. The observed low-field effect is related to the HFM mechanism while the high-field effect to the T-q interaction in a framework of the trion model

ments of CT states fluorescence and photocurrent generation under a magnetic field at various pressures also indicates more efficient triplet channels [85]. A similar outcome has been obtained for polymer (P3HT or MDMO-PPV):fullerene blends at cryogenic temperatures where MFEs of spin polarization origin were investigated [127]. Nevertheless, there are systems for which the molecular triplet state of a donor (acceptor or both of them) is lying below the CT state, e.g. m-MTDATA:BCP or m-MTDATA:PBD, and then a ^1CT state appears to be more efficient in charge carriers dissociation events - Fig. 6.25 [61] (see also [85]).

7 Final remarks and conclusions

To briefly summarize we have examined photocurrent generation processes in dye-sensitized solar cells of different architectures (TiO_2 photoanode in the form of nanoparticles or nanotubes sensitized by ruthenium N719, dinuclear ruthenium B1 or fully organic squaraine SQ2 dye) by means of magnetic field effect technique. The obtained results show that separation of charge carriers proceeds through the intermediate state of electron-hole pairs, where an electron occupies the conduction level of TiO_2 and a hole is localized on an oxidized dye molecule, for organic dye- as well as for ruthenium dye-based solar cells. Moreover, in both cases intersystem crossing between pair spin states plays a significant role in the overall photocurrent generation mechanism. For organic dye-based solar cells triplet state dissociation is rather inefficient due to fast decay of triplets. On the contrary, the lack of a triplet drain in Ru solar cells with ^3MLCT molecular states lying above $(e-h)$ pair levels ensures charge generation from triplet $^3(e-h)$ states to be much more efficient. Taking this into account we can distinguish the factors that should be considered when designing new sensitizers. We have observed that the magnitude of the weak negative magneto-photocurrent (MPC) signals in DSSCs is controlled by the radius and spin coherence time of $(e-h)$ pairs that can be experimentally modified by the photoanode morphology (TiO_2 nanoparticles or nanotubes) and the electronic orbital structure of various dye molecules (N719, B1 and SQ2 dyes). The observed MFEs are explained by the Δg mechanism ascribed to the relatively high Δg value for electron and hole entities comprising $(e-h)$ pairs.

A study of photocurrent in SQ based solar cells, conducted for a wide range of magnetic fields and temperatures, reveals that depending on the electron acceptor content, the photocurrent generation is limited by dissociation/recombination of $(e-h)$ pairs or CT states. In a weak external magnetic field, the HFM mechanism operates, where an asymmetry in local (of hyperfine origin) magnetic fields experienced by electrons and holes forming $(e-h)$ pairs induces spin dephasing of magnetic dipoles. On the other hand, in a strong magnetic field the photocurrent is affected by the Δg mech-

anism with spin dephasing ascribed to different Lande factors of electron and hole entities. The temperature dependence of the MPC signal indicates that charge carrier hopping in a disordered environment plays the essential role in a consistent analysis of MFEs in SQ:PCBM systems. The best performance parameters of solar cells are achieved in systems without molecular 'triplet drains' where the dissociation of spin-protected triplet CT states is more favorable. The findings of the present work enable novel methods to engineer photovoltaic devices utilizing organic electron donor - electron acceptor systems, in particular, to determine the alignment of energy levels involved in the photocurrent generation process. With this respect, in addition to SQ:fullerene solar cells, other systems with similar energy levels alignment, like P3HT or MDMO-PPV polymers blended with fullerene derivatives, can be distinguished.

To the best of our knowledge, we have studied here for the first time the magnetic field effects in small-molecular weight organic:fullerene bulk-heterojunction solar cells and unravelled the mechanisms underlying these effects for a wide range of magnetic field strengths. A detailed description of photocurrent generation process in dye-sensitized solar cells incorporating intermediate state of $(e-h)$ pairs has been reported for the first time as well.

Finally, we note that magnetic field effect technique is a unique tool to determine the role of the relevant excited states and their spin mixing in the process of charge carrier photogeneration, which is essential for any effective attempts to improve the performance of the new generation of solar cells. With this respect the joined static magnetic field effects (MC, MEL, MPC, MPL) and reaction yield detected magnetic electron resonance (RYDMR) measurements will certainly put more emphasis on scrutiny of existing models [128, 129]. A direct spin manipulation by a pulsed electrically detected magnetic resonance (pEDMR) has been recently demonstrated on organic materials by Boehme, Lupton and co-workers [130]. Applying combined static and pulsed magnetic field measurements on the same materials, as has been explored mainly for MEH-PPV [130] polymer and MEH-PPV:PCBM [131] blend offer completely new insight into existing models of magnetic effects [132]. Microscopically tracking of spin polarization of interfacial organic/inorganic $(e-h)$ pairs in DSSCs containing a liquid electrolyte and a thick semiconductor layer by pEDMR technique is really challenging.

Acknowledgement

First of all, I would like to express my deepest gratitude and respect to dr hab. inż. Waldemar Stampor, prof. nadzw. PG, my supervisor and mentor. I am grateful for being given the opportunity to start the PhD procedure within your research group as well as being introduced to the physics of organic solids and for all the knowledge he has shared with me. His invaluable guidance as well as time and energy involvement was crucial during my work on this Thesis. Our frequent, long discussions made a true scientist of me.

My sincere thanks to prof. Sayani Majumdar for the invitation to Aalto University, for her patience and all the consultations. I appreciate her effort in providing me with the access to all the necessary facilities and her care during my stay in Finland.

My appreciation also goes to dr hab. Maciej Zalas from the Adam Mickiewicz University in Poznan for all valuable pieces of advice and for discussions allowing us to solve out scientific problems. Thank you for making my visit to the SmartMatLab Centre at the Dipartimento di Chimica of the Università degli Studi di Milano possible.

I also would like to address all my colleagues from the Department of Physics of Electronic Phenomena. Their kindness made everyday work joyful. In particular, I would like to thank Daniel Pelczarski for the shared work and support, as well as dr inż. Piotr Grygiel for the help with measurement designing setups, Dr inż. Justyna Szostak - her comments and translational skills were precious to me, Karol Falkowski and dr Tomasz Neumann - they have given me all the pieces of advice needed to use LaTeXeditor to its fullest, and last but not least, Iwona Kuzborska - master of all administrative paperwork.

Also the scientists from The Szewalski Institute of Fluid-Flow Machinery of the Polish Academy of Sciences made a significant contribution to who I am as a researcher today: dr hab. inż. Adam Cenian, prof. IMP PAN, who allowed me to work in his science group, dr hab. inż. Katarzyna Siuzdak who guided me through the chemical aspects of my research and helped a

lot with grant applications. My gratefulness however, goes especially to dr hab. inż. Mirosław Sawczak who taught me all about experimental work and shared a tremendous amount of his knowledge with me.

I want to thank all co-authors of the publications for their commitment and fruitful cooperation.

Specjalne podziękowania kieruję do mojego wujka - Dariusza Koziary. Wujku, to dzięki Tobie połknąłem bakcyla i fizyka stała się moją pasją.

Kochani rodzice, dziękuję za trud i wysiłek jaki włożyliście w proces mojej edukacji. Jestem wdzięczny za stworzenie mi wspaniałych warunków do nauki, nieustanną wiarę we mnie i wsparcie w trudnych chwilach.

A very special recognition goes to Sonia Stasiak, my fiancée. I much appreciate her outstanding patience and understanding as well as her support and motivation in writing this Thesis.

References

[1] European Environment Agency, "Shaping the future of energy in Europe: Clean , smart and renewable," Tech. Rep. 11, Copenhagen, 2017.

[2] N. Armaroli and V. Balzani, "The future of energy supply: Challenges and opportunities," *Angewandte Chemie - International Edition*, vol. 46, no. 1, pp. 52–66, 2007.

[3] A. J. Nozik, G. Conibeer, and M. C. Beard, eds., *Advanced Concepts in Photovoltaics*. Royal Society of Chemistry, 2014.

[4] A. Luque and S. Hegedus, *Handbook of photovoltaic science and engineering*. Wiley, 2nd ed., 2011.

[5] H. Spanggaard and F. C. Krebs, "A brief history of the development of organic and polymeric photovoltaics," *Solar Energy Materials and Solar Cells*, vol. 83, pp. 125–146, 2004.

[6] J. A. Barltrop and J. D. Coyle, *Principles of photochemistry*. Wiley, 1978.

[7] W. H. Brown, B. L. Iverson, E. V. Anslyn, and C. S. Foote, *Organic chemistry*. Brooks/Cole, Cengage Learning, 7th ed., 2014.

[8] P. W. Atkins and J. De Paula, *Atkins' Physical Chemistry*. Oxford University Press, 8th ed., 2006.

[9] A. Juris, V. Balzani, F. Barigelletti, S. Campagna, P. Belser, and A. von Zalewsky, "Ru(II) polypyridine complexes: photophysics, photochemistry, eletrochemistry, and chemiluminescence," *Coordination Chemistry Reviews*, vol. 84, pp. 85–277, 1988.

[10] P. Suppan, *Chemistry and Light*. Cambridge: Royal Society of Chemistry, 1994.

[11] B. H. Bransden and C. J. Joachain, *Physics of atoms and molecules*. Pearson, 2nd ed., 2003.

[12] H. Hayashi, *Introduction to Dynamic Spin Chemistry*. World Scientific, 2004.

[13] P. W. Atkins, *Concepts in physical chemistry*. Oxford University Press, 1995.

[14] B. Wardle, *Principles and applications of photochemistry*. Wiley, 2009.

[15] H. Yersin, "Triplet Emitters for OLED Applications. Mechanisms of Exciton Trapping and Control of Emission Properties," *Topics in Current Chemistry*, vol. 241, pp. 1–26, 2004.

[16] M. Pope and C. E. Swenberg, *Electronic Processes in Organic Crystals and Polymers*. Oxford University Press, 1999.

[17] E. A. Silinsh, *Organic molecular crystals*. Springer-Verlag, 1980.

[18] A. S. Davydov, *Theory of molecular excitons*. Plenum Press, 1971.

[19] A. Köhler and H. Bässler, *Electronic Processes in Organic Semiconductors*. Wiley-VCH Verlag GmbH & Co. KGaA, 2015.

[20] J. Sworakowski, J. Lipinski, and K. Janus, "On the reliability of determination of energies of HOMO and LUMO levels in organic semiconductors from electrochemical measurements. A simple picture based on the electrostatic model," *Organic Electronics*, vol. 33, pp. 300–310, 2016.

[21] B. O'Regan and M. Grätzel, "A low-cost, high-efficiency solar cell based on dye-sensitized colloidal TiO2 films," *Nature*, vol. 353, pp. 737–740, 1991.

[22] M. Grätzel, "Photoelectrochemical cells," *Nature*, vol. 414, pp. 338–344, 2001.

[23] H. Gerischer and H. Tributsch, "Elektrochemische Untersuchungen zur spektralen Sensibilisierung von ZnO-Einkristallen," *Berichte der Bunsengesellschaft für physikalische Chemie*, vol. 72, pp. 437–445, 1968.

[24] H. Gerischer, M. Michel-Beyerle, F. Rebentrost, and H. Tributsch, "Sensitization of charge injection into semiconductors with large band gap," *Electrochimica Acta*, vol. 13, pp. 1509–1515, 1968.

[25] K. Kakiage, Y. Aoyama, T. Yano, K. Oya, J.-i. Fujisawa, and M. Hanaya, "Highly-efficient dye-sensitized solar cells with collaborative sensitization by silyl-anchor and carboxy-anchor dyes," *Chemical Communications*, vol. 51, no. 88, pp. 15894–15897, 2015.

[26] T. Kinoshita, K. Nonomura, N. Joong Jeon, F. Giordano, A. Abate, S. Uchida, T. Kubo, S. I. Seok, M. K. Nazeeruddin, A. Hagfeldt, M. Grätzel, and H. Segawa, "Spectral splitting photovoltaics using perovskite and wideband dye-sensitized solar cells," *Nature Communications*, vol. 6, p. 8834, 2015.

[27] A. Hagfeldt, G. Boschloo, L. Sun, L. Kloo, and H. Pettersson, "Dye-sensitized solar cells.," *Chemical Reviews*, vol. 110, pp. 6595–6663, 2010.

[28] K. Kalyanasundaram, *Dye-sensitized solar cells*. CRC Press, 2010.

[29] H. Kallmann and M. Pope, "Photovoltaic Effect in Organic Crystals," *The Journal of Chemical Physics*, vol. 30, pp. 585–586, 1959.

[30] W. Pisula, A. K. Mishra, J. Li, M. Baumgarten, and K. Müllen, "Carbazole-Based Conjugated Polymers as Donor Material for Photovoltaic Devices," in *Organic Photovoltaics* (C. Brabec, V. Dyakonov, and U. Scherf, eds.), pp. 93–128, Wiley-VCH Verlag GmbH & Co. KGaA, 2008.

[31] C. W. Tang, "Two-layer organic photovoltaic cell," *Applied Physics Letters*, vol. 48, pp. 183–185, 1986.

[32] N. S. Sariciftci, L. Smilowitz, A. J. Heeger, and F. Wudl, "Photoinduced Electron Transfer from a Conducting Polymer to Buckminsterfullerene," *Science*, vol. 258, pp. 1474–1476, 1992.

[33] Y.-W. Su, S.-C. Lan, and K.-H. Wei, "Organic photovoltaics," *Materials Today*, vol. 15, pp. 554–562, 2012.

[34] D. S. Ginley and D. Cahen, *Fundamentals of Materials for Energy and Environmental Sustainability*. Cambridge University Press, 2011.

[35] A. Carrington and A. D. McLachlan, *Introduction to magnetic resonance with applications to chemistry and chemical physics*. Harper and Row, 1967.

[36] J. Kalinowski, J. Szmytkowski, and W. Stampor, "Magnetic hyperfine modulation of charge photogeneration in solid films of Alq3," *Chemical Physics Letters*, vol. 378, no. 3, pp. 380–387, 2003.

[37] J. Kalinowski, M. Cocchi, D. Virgili, P. Di Marco, and V. Fattori, "Magnetic field effects on emission and current in Alq3-based electroluminescent diodes," *Chemical Physics Letters*, vol. 380, no. 5-6, pp. 710–715, 2003.

[38] B. Hu and Y. Wu, "Tuning magnetoresistance between positive and negative values in organic semiconductors.," *Nature Materials*, vol. 6, no. 12, pp. 985–991, 2007.

[39] J. M. Lupton and C. Boehme, "Magnetoresistance in organic semiconductors," *Nature Materials*, vol. 7, no. 8, p. 598, 2008.

[40] W. Wagemans and B. Koopmans, "Spin transport and magnetoresistance in organic semiconductors," *Physica Status Solidi (B) Basic Research*, vol. 248, no. 5, pp. 1029–1041, 2011.

[41] R. Johnson, R. Merrifield, P. Avakian, and R. Filippen, "Effects of Magnetic Fields on the Mutual Annihilation of Triplet Excitons in Molecular Crystals," *Physical Review Letters*, vol. 19, no. 6, pp. 285–287, 1967.

[42] P. Avakian, "Influence of Magnetic Field on Luminescence Involving Triplet Excitons," *Pure and Applied Chemistry*, vol. 37, no. 1-2, pp. 1–19, 1974.

[43] R. Johnson and R. Merrifield, "Effects of Magnetic Fields on the Mutual Annihilation of Triplet Excitons in Anthracene Crystals," *Physical Review B*, vol. 1, no. 2, pp. 896–902, 1970.

[44] V. Ern and R. E. Merrifield, "Magnetic field effect on triplet exciton quenching in organic crystals," *Physical Review Letters*, vol. 21, no. 9, pp. 609–611, 1968.

[45] A. Kadashchuk, V. I. Arkhipov, C. H. Kim, J. Shinar, D. W. Lee, Y. R. Hong, J. I. Jin, P. Heremans, and H. Bässler, "Localized trions in conjugated polymers," *Physical Review B*, vol. 76, no. 23, p. 235205, 2007.

[46] M. Cox, P. Janssen, F. Zhu, and B. Koopmans, "Traps and trions as origin of magnetoresistance in organic semiconductors," *Physical Review B*, vol. 88, no. 3, pp. 1–7, 2013.

[47] D. Pelczarski, P. Grygiel, M. Miśnik, and W. Stampor, "Photoconduction and magnetic field effect on photoconduction in hole-transporting

star-burst amine (m-MTDATA) films," *Organic Electronics*, vol. 21, pp. 54–65, 6 2015.

[48] P. Atkins, "Magnetic field effects," *Chemistry in Britian*, vol. 12, pp. 214–218, 1976.

[49] R. P. Groff, R. Merrifield, A. Suna, and P. Avakian, "Magnetic Hyperfine Modulation of Dye-Sensitized Delayed Fluorescence in an Organic Crystal," *Physical Review Letters*, vol. 29, no. 7, pp. 429–431, 1972.

[50] R. P. Groff, A. Suna, P. Avakian, and R. E. Merrifield, "Magnetic hyperfine modulation of dye-sensitized delayed fluorescence in organic crystals," *Physical Review B*, vol. 9, pp. 2655–2660, 3 1974.

[51] G. Huttmann and H. Staerk, "Delayed Luminescence of Naphthalene in Isooctane. Spectral, Lifetime, and Magnetic Field Studies of Delayed Fluorescence and Monomer Phosphorescence at 293 K," *Journal of Physical Chemistry*, vol. 95, pp. 4951–4954, 1991.

[52] E. L. Frankevich, "Nature of a New Effect of a Change in Photoconductivity of Organic Semiconductors in a Magnetic Field," *Soviet Physics JETP*, vol. 23, no. 5, pp. 814–819, 1966.

[53] P. A. Bobbert, T. D. Nguyen, F. W. A. Van Oost, B. Koopmans, and M. Wohlgenannt, "Bipolaron mechanism for organic magnetoresistance," *Physical Review Letters*, vol. 99, no. 21, p. 216801, 2007.

[54] N. J. Harmon and M. E. Flatté, "Semiclassical theory of magnetoresistance in positionally disordered organic semiconductors," *Physical Review B*, vol. 85, p. 075204, 2 2012.

[55] S. E. Koops, P. R. F. Barnes, B. C. O'Regan, and J. R. Durrant, "Kinetic competition in a coumarin dye-sensitized solar cell: Injection and recombination limitations upon device performance," *Journal of Physical Chemistry C*, vol. 114, no. 17, pp. 8054–8061, 2010.

[56] S. E. Koops, B. C. ORegan, P. R. F. Barnes, and J. R. Durrant, "Parameters Influencing the Efficiency of Electron Injection in Dye-Sensitized Solar Cells," *Journal of the American Chemical Society*, vol. 131, no. 13, pp. 4808–4818, 2009.

[57] A. Furube, R. Katoh, and K. Hara, "Electron injection dynamics in dye-sensitized semiconductor nanocrystalline films," *Surface Science Reports*, vol. 69, no. 4, pp. 389–441, 2014.

[58] C. Martín, M. Ziółek, and A. Douhal, "Ultrafast and fast charge separation processes in real dye-sensitized solar cells," *Journal of Photochemistry and Photobiology C: Photochemistry Reviews*, vol. 26, pp. 1–30, 2016.

[59] J. Sobuś, G. Burdziński, J. Karolczak, J. Idígoras, J. A. Anta, and M. Ziółek, "Comparison of TiO2 and ZnO solar cells sensitized with an indoline dye: Time-resolved laser spectroscopy studies of partial charge separation processes," *Langmuir*, vol. 30, no. 9, pp. 2505–2512, 2014.

[60] X. Xu, J. Cui, J. Han, J. Zhang, Y. Zhang, L. Luan, G. Alemu, Z. Wang, Y. Shen, D. Xiong, W. Chen, Z. Wei, S. Yang, B. Hu, Y. Cheng, and M. Wang, "Near field enhanced photocurrent generation in p-type dye-sensitized solar cells.," *Scientific Reports*, vol. 4, p. 3961, 2014.

[61] D. Pelczarski, P. Grygiel, K. Falkowski, M. Klein, and W. Stampor, "Electromodulation and magnetomodulation of exciton dissociation in electron donor (starburst amine): Electron acceptor (bathocuproine) system," *Organic Electronics*, vol. 25, pp. 362–376, 2015.

[62] P. Shakya, P. Desai, T. Kreouzis, W. P. Gillin, S. M. Tuladhar, A. M. Ballantyne, and J. Nelson, "The effect of applied magnetic field on photocurrent generation in poly-3-hexylthiophene:[6,6]-phenyl C61-butyric acid methyl ester photovoltaic devices," *Journal of Physics: Condensed Matter*, vol. 20, no. 45, p. 452203, 2008.

[63] Y. Zhang, T. P. Basel, B. R. Gautam, X. Yang, D. J. Mascaro, F. Liu, and Z. V. Vardeny, "Spin-enhanced organic bulk heterojunction photovoltaic solar cells.," *Nature Communications*, vol. 3, p. 1043, 2012.

[64] A. Rao, P. C. Y. Chow, S. Gélinas, C. W. Schlenker, C.-Z. Li, H.-L. Yip, A. K.-Y. Jen, D. S. Ginger, and R. H. Friend, "The role of spin in the kinetic control of recombination in organic photovoltaics.," *Nature*, vol. 500, no. 7463, pp. 435–439, 2013.

[65] F. Cai, J. Wang, Z. Yuan, and Y. Duan, "Magnetic-field effect on dye-sensitized ZnO nanorods-based solar cells," *Journal of Power Sources*, vol. 216, pp. 269–272, 2012.

[66] F. Cai, S. Zhang, S. Zhou, and Z. Yuan, "Magnetic-field enhanced photovoltaic performance of dye-sensitized TiO 2 nanoparticle-based solar cells," *Chemical Physics Letters*, vol. 591, pp. 166–169, 2014.

[67] Z. Xu and B. Hu, "Photovoltaic processes of singlet and triplet excited states in organic solar cells," *Advanced Functional Materials*, vol. 18, no. 17, pp. 2611–2617, 2008.

[68] A. H. Devir-Wolfman, B. Khachatryan, B. R. Gautam, L. Tzabary, A. Keren, N. Tessler, Z. V. Vardeny, and E. Ehrenfreund, "Short-lived charge-transfer excitons in organic photovoltaic cells studied by high-field magneto-photocurrent.," *Nature Communications*, vol. 5, p. 4529, 2014.

[69] G. Chen, H. Sasabe, T. Igarashi, Z. Hong, and J. Kido, "Squaraine dyes for organic photovoltaic cells," *Journal of Materials Chemistry A*, vol. 3, no. 28, pp. 14517–14534, 2015.

[70] T. Goh, J.-S. Huang, K. G. Yager, M. Y. Sfeir, C.-Y. Nam, X. Tong, L. M. Guard, P. R. Melvin, F. Antonio, B. G. Bartolome, M. L. Lee, N. Hazari, and A. D. Taylor, "Quaternary Organic Solar Cells Enhanced by Cocrystalline Squaraines with Power Conversion Efficiencies over 10%," *Advanced Energy Materials*, vol. 6, no. 21, p. 1600660, 2016.

[71] K.-Y. Law, "Squaraine Chemistry. Effects of Structural Changes on the Absorption and Multiple Fluorescence Emission of Bis[4-(dimethylamino)phenyl]squaraine and Its Derivatives," *Journal of Physical Chemistry*, vol. 91, no. 8, pp. 5184–5193, 1987.

[72] F. Silvestri, M. D. Irwin, L. Beverina, A. Facchetti, G. A. Pagani, and T. J. Marks, "Efficient squaraine-based solution processable bulk-heterojunction solar cells," *Journal of the American Chemical Society*, vol. 130, no. 52, pp. 17640–17641, 2008.

[73] X. Xiao, G. Wei, S. Wang, J. D. Zimmerman, C. K. Renshaw, M. E. Thompson, and S. R. Forrest, "Small-molecule photovoltaics based on functionalized squaraine donor blends," *Advanced Materials*, vol. 24, no. 15, pp. 1956–1960, 2012.

[74] G. Chen, H. Sasabe, Z. Wang, X. F. Wang, Z. Hong, Y. Yang, and J. Kido, "Co-evaporated bulk heterojunction solar cells with ¿6.0% efficiency," *Advanced Materials*, vol. 24, no. 20, pp. 2768–2773, 2012.

[75] J. D. Zimmerman, B. E. Lassiter, X. Xiao, K. Sun, A. Dolocan, R. Gearba, D. A. V. Bout, K. J. Stevenson, P. Wickramasinghe, M. E. Thompson, and S. R. Forrest, "Control of Interface Order by Inverse Quasi-Epitaxial Growth of Squaraine/ Fullerene Thin Film Photovoltaics," *ACS Nano*, vol. 7, no. 10, pp. 9268–9275, 2013.

[76] Y. Zheng and F. Wudl, "Organic spin transporting materials: present and future," *Journal of Materials Chemistry A*, vol. 2, no. 1, pp. 48–57, 2014.

[77] G. Wei, R. R. Lunt, K. Sun, S. Wang, M. E. Thompson, and S. R. Forrest, "Efficient, ordered bulk heterojunction nanocrystalline solar cells by annealing of ultrathin squaraine thin films," *Nano Letters*, vol. 10, no. 9, pp. 3555–3559, 2010.

[78] G. Wei, S. Wang, K. Sun, M. E. Thompson, and S. R. Forrest, "Solvent-annealed crystalline squaraine: PC 70BM (1:6) solar cells," *Advanced Energy Materials*, vol. 1, no. 2, pp. 184–187, 2011.

[79] G. Wei, S. Wang, K. Renshaw, M. E. Thompson, and S. R. Forrest, "Solution-processed squaraine bulk heterojunction photovoltaic cells," *ACS Nano*, vol. 4, no. 4, pp. 1927–1934, 2010.

[80] A. R. bin Mohd Yusoff, S. J. Lee, H. P. Kim, F. K. Shneider, W. J. da Silva, and J. Jang, "8.91% Power Conversion Efficiency for Polymer Tandem Solar Cells," *Advanced Functional Materials*, vol. 24, pp. 2240–2247, 4 2014.

[81] K. Vandewal, K. Tvingstedt, A. Gadisa, O. Inganäs, and J. V. Manca, "On the origin of the open-circuit voltage of polymerfullerene solar cells," *Nature Materials*, vol. 8, pp. 904–909, 11 2009.

[82] S. R. Yost, J. Lee, M. W. B. Wilson, T. Wu, D. P. McMahon, R. R. Parkhurst, N. J. Thompson, D. N. Congreve, A. Rao, K. Johnson, M. Y. Sfeir, M. G. Bawendi, T. M. Swager, R. H. Friend, M. A. Baldo, and T. Van Voorhis, "A transferable model for singlet-fission kinetics," *Nature Chemistry*, vol. 6, no. 6, pp. 492–497, 2014.

[83] D. N. Congreve, J. Lee, N. J. Thompson, E. Hontz, S. R. Yost, P. D. Reusswig, M. E. Bahlke, S. Reineke, T. Van Voorhis, and M. A. Baldo, "External Quantum Efficiency Above 100% in a Singlet-Exciton-Fission-Based Organic Photovoltaic Cell," *Science*, vol. 340, no. 6130, pp. 334–337, 2013.

[84] S. D. Dimitrov, S. Wheeler, D. Niedzialek, B. C. Schroeder, H. Utzat, J. M. Frost, J. Yao, A. Gillett, P. S. Tuladhar, I. McCulloch, J. Nelson, and J. R. Durrant, "Polaron pair mediated triplet generation in polymer/fullerene blends," *Nature Communications*, vol. 6, p. 6501, 2015.

[85] W. Chang, D. N. Congreve, E. Hontz, M. E. Bahlke, D. P. McMahon, S. Reineke, T. C. Wu, V. Bulović, T. Van Voorhis, and M. A. Baldo, "Spin-dependent charge transfer state design rules in organic photovoltaics.," *Nature Communications*, vol. 6, p. 6415, 2015.

[86] P. Janssen, M. Cox, S. H. W. Wouters, M. Kemerink, M. M. Wienk, and B. Koopmans, "Tuning organic magnetoresistance in polymer-fullerene blends by controlling spin reaction pathways.," *Nature Communications*, vol. 4, p. 2286, 2013.

[87] D. Sun, E. Ehrenfreund, and Z. Valy Vardeny, "The first decade of organic spintronics research," *Chemical Communications*, vol. 50, no. 50, pp. 1781–1793, 2014.

[88] C. Zhang, D. Sun, C.-X. Sheng, Y. X. Zhai, K. Mielczarek, A. Zakhidov, and Z. V. Vardeny, "Magnetic field effects in hybrid perovskite devices," *Nature Physics*, vol. 11, no. May, pp. 427–434, 2015.

[89] P. Y. Lin, T. Wu, M. Ahmadi, L. Liu, S. Haacke, T. F. Guo, and B. Hu, "Simultaneously enhancing dissociation and suppressing recombination in perovskite solar cells," *Nano Energy*, vol. 36, no. February, pp. 95–101, 2017.

[90] M. A. Cabero Zabalaga, J. Wei, H. Yang, B. B. Fan, Y. Sun, and W. Zhao, "Unraveling the Characteristic Shape for Magnetic Field Effects in PolymerFullerene Solar Cells," *ACS Omega*, vol. 2, no. 11, pp. 7777–7783, 2017.

[91] M. Zalas, B. Gierczyk, M. Klein, K. Siuzdak, T. Pedziński, and T. Łuczak, "Synthesis of a novel dinuclear ruthenium polypyridine dye for dye-sensitized solar cells application," *Polyhedron*, vol. 67, pp. 381–387, 2014.

[92] K.-l. Li, Z.-b. Xie, and S. Adams, "A reliable TiO2 nanotube membrane transfer method and its application in photovoltaic devices," *Electrochimica Acta*, vol. 62, pp. 116–123, 2012.

[93] M. Klein, R. Pankiewicz, M. Zalas, and W. Stampor, "Magnetic field effects in dye-sensitized solar cells controlled by different cell architecture," *Scientific Reports*, vol. 6, p. 30077, 2016.

[94] J. Stewart, "MO-G," 2008.

[95] M. J. Frish, G. W. Trucks, H. B. Schlegel, G. E. Scuseria, M. A. Robb, J. R. Cheeseman, J. A. Montgomery, T. Vreven, K. N. Kudin, J. C. Burant, J. M. Millam, S. S. Iyengar, J. Tomasi, V. Barone, B. Mennucci, M. Cossi, G. Scalmani, C. Rega, and P. J. A., "Gaussian03, Revision B.04, Gaussian, Inc.: Pittsburgh, PA," 2003.

[96] T. Geiger, S. Kuster, J. H. Yum, S. J. Moon, M. K. Nazeeruddin, M. Gratzel, and F. Nüesch, "Molecular design of unsymmetrical squaraine dyes for high efficiency conversion of low energy photons into electrons using TiO2 nanocrystalline films," *Advanced Functional Materials*, vol. 19, no. 17, pp. 2720–2727, 2009.

[97] P. V. Kamat, S. Das, K. G. Thomas, and M. V. George, "Photochemistry of squaraine dyes. 1. Excited singlet, triplet, and redox states of bis[4-(dimethylamino)phenyl]squaraine and bis[4-(dimethylamino)-2-hydroxyphenyl]squaraine," *Journal of Physical Chemistry*, vol. 96, no. 1, pp. 195–199, 1992.

[98] S. Webster, S. A. Odom, L. A. Padilha, O. V. Przhonska, D. Peceli, H. Hu, G. Nootz, A. D. Kachkovski, J. Matichak, S. Barlow, H. L. Anderson, S. R. Marder, D. J. Hagan, and E. W. Van Stryland, "Linear and nonlinear spectroscopy of a porphyrin-squaraine-porphyrin conjugated system," *Journal of Physical Chemistry B*, vol. 113, no. 45, pp. 14854–14867, 2009.

[99] D. Veldman, I. Pek, S. C. J. Meskers, J. Rgen Sweelssen, M. M. Koetse, S. C. Veenstra, J. M. Kroon, S. S. Van Bavel, J. Loos, and R. A. J. Janssen, "Compositional and Electric Field Dependence of the Dissociation of Charge Transfer Excitons in Alternating Polyfluorene Copolymer/Fullerene Blends," *Journal of the American Chemical Society*, vol. 130, no. 24, pp. 7721–7735, 2008.

[100] X. Chen and S. S. Mao, "Titanium dioxide nanomaterials: Synthesis, properties, modifications and applications," *Chemical Reviews*, vol. 107, no. 7, pp. 2891–2959, 2007.

[101] P. Docampo, A. Ivaturi, R. Gunning, S. Diefenbach, C. M. Palumbiny, J. Kirkpatrick, H. Geaney, V. Sivaram, L. Schmidt-Mende, M. Welland, and H. Snaith, "The influence of 1D, meso- and crystal structures on charge transport and recombination in solid-state dye-sensitized solar cells," *Journal of Materials Chemistry A*, vol. 1, pp. 12088–12095, 2013.

[102] C. Wehrenfennig, C. M. Palumbiny, H. J. Snaith, M. B. Johnston, L. Schmidt-Mende, and L. M. Herz, "Fast Charge-Carrier Trapping in TiO2 Nanotubes," *Journal of Physical Chemistry C*, vol. 119, no. 17, pp. 9159–9168, 2015.

[103] D. Pelczarski, P. Grygiel, K. Falkowski, M. Klein, and W. Stampor, "Electromodulation and magnetomodulation of exciton dissociation in electron donor (starburst amine) : electron acceptor (bathocuproine) system," *Organic Electronics*, vol. 25, pp. 362–376, 10 2015.

[104] A. J. Schellekens, W. Wagemans, S. P. Kersten, P. A. Bobbert, and B. Koopmans, "Microscopic modeling of magnetic-field effects on charge transport in organic semiconductors," *Physical Review B*, vol. 84, no. 7, p. 75204, 2011.

[105] K. Schulten, H. Staerk, A. Weller, H.-J. Werner, and B. Nickel, "Magnetic Field Dependence of the Geminate Recombination of Radical Ion Pairs in Polar Solvents," *Zeitschrift für Physikalische Chemie*, vol. 101, pp. 371–390, 9 1976.

[106] M. Fittipaldi, D. Gatteschi, and P. Fornasiero, "The power of EPR techniques in revealing active sites in heterogeneous photocatalysis: The case of anion doped TiO2," *Catalysis Today*, vol. 206, pp. 2–11, 2013.

[107] T. Rajh, J. M. Nedeljkovic, L. X. Chen, O. Poluektov, and M. C. Thurnauer, "Improving Optical and Charge Separation Properties of Nanocrystalline TiO2 by Surface Modification with Vitamin C," *The Journal of Physical Chemistry B*, vol. 103, no. 18, pp. 3515–3519, 1999.

[108] R. E. DeSimone and R. S. Drago, "Magnetic resonance studies of some low-spin d5 tris diimine complexes," *Journal of the American Chemical Society*, vol. 92, pp. 2343–2352, 4 1970.

[109] W. H. Quayle and J. H. Lunsford, "Tris(2,2'-bipyridine)ruthenium(III) in zeolite Y: characterization and reduction on exposure to water," *Inorganic Chemistry*, vol. 21, pp. 97–103, 1 1982.

[110] M. Ledney and P. K. Dutta, "Oxidation of Water to Dioxygen by Intrazeolitic Ru(bpy)33+," *Journal of the American Chemical Society*, vol. 117, pp. 7687–7695, 7 1995.

[111] H. Hayashi and S. Nagakura, "Theoretical Study of Relaxation Mechanism in Magnetic Field Effects on Chemical Reactions," 1984.

[112] F. J. Wang, H. Bassler, and Z. V. Vardeny, "Magnetic field effects in π-conjugated polymer-fullerene blends: Evidence for multiple components," *Physical Review Letters*, vol. 101, no. 23, p. 236805, 2008.

[113] W. Stampor and J. Mężyk, "Electromodulation of photoluminescence in vacuum-evaporated films of fac-tris(2-phenylpyridine)iridium(III)," *Chemical Physics*, vol. 337, pp. 151–160, 8 2007.

[114] S. Westenhoff, I. A. Howard, J. M. Hodgkiss, K. R. Kirov, H. A. Bronstein, C. K. Williams, N. C. Greenham, and R. H. Friend, "Charge recombination in organic photovoltaic devices with high open-circuit voltages," *Journal of the American Chemical Society*, vol. 130, no. 41, pp. 13653–13658, 2008.

[115] M. Wohlgenannt and Z. V. Vardeny, "Spin-dependent exciton formation rates in pi-conjugated materials," *Journal of Physics: Condensed Matter*, vol. 15, no. 3, pp. R83–R107, 2003.

[116] B. Fan, Y. Maniglio, M. Simeunovic, S. Kuster, T. Geiger, R. Hany, and F. Nüesch, "Squaraine planar-heterojunction solar cells," *International Journal of Photoenergy*, vol. 2009, p. 581068, 2009.

[117] E. Frankevich, A. Zakhidov, K. Yoshino, Y. Maruyama, and K. Yakushi, "Photoconductivity of poly(2,5-diheptyloxy-p-phenylene vinylene) in the air atmosphere: Magnetic-field effect and mechanism of generation and recombination of charge carriers," *Physical Review B*, vol. 53, no. 8, pp. 4498–4508, 1996.

[118] B. Hu, L. Yan, and M. Shao, "Magnetic-field effects in organic semiconducting materials and devices," *Advanced Materials*, vol. 21, no. 14-15, pp. 1500–1516, 2009.

[119] T. D. Nguyen, B. R. Gautam, E. Ehrenfreund, and Z. V. Vardeny, "Magnetoconductance response in unipolar and bipolar organic diodes at ultrasmall fields," *Physical Review Letters*, vol. 105, no. 16, p. 166804, 2010.

[120] Y. Lei, Q. Song, Y. Zhang, P. Chen, R. Liu, Q. Zhang, and Z. Xiong, "Magnetoconductance of polymerfullerene bulk heterojunction solar cells," *Organic Electronics*, vol. 10, no. 7, pp. 1288–1292, 2009.

[121] V. I. Krinichnyi, E. I. Yudanova, and N. G. Spitsina, "Light-Induced Electron Paramagnetic Resonance Study of Poly(3-alkylthiophene)/Fullerene Composites," *The Journal of Physical Chemistry C*, vol. 114, pp. 16756–16766, 10 2010.

[122] B. Khachatryan, A. H. Devir-Wolfman, L. Tzabari, N. Tessler, Z. V. Vardeny, and E. Ehrenfreund, "Magnetophotocurrent in Organic Bulk Heterojunction Photovoltaic Cells at Low Temperatures and High Magnetic Fields," *Physical Review Applied*, vol. 5, no. 4, p. 044001, 2016.

[123] B. Khachatryan, A. Devir-Wolfman, L. Tzabary, A. Keren, N. Tessler, Z. Vardeny, and E. Ehrenfreund, "High field magneto-photocurrent in organic bulk hetero-junction photo-voltaic cells," *Synthetic Metals*, vol. 60, pp. 8–11, 2015.

[124] F. Alvarez, A. Alegria, and J. Colmenero, "Relationship between the time-domain Kohlrausch-Williams-Watts and frequency-domain Havriliak-Negami relaxation functions," *Physical Review B*, vol. 44, no. 14, pp. 7306–7312, 1991.

[125] J. Wang, A. Chepelianskii, F. Gao, and N. C. Greenham, "Control of exciton spin statistics through spin polarization in organic optoelectronic devices," *Nature Communications*, vol. 3, p. 1191, 2012.

[126] Y. Sheng, T. D. Nguyen, G. Veeraraghavan, . Mermer, M. Wohlgenannt, S. Qiu, and U. Scherf, "Hyperfine interaction and magnetoresistance in organic semiconductors," *Physical Review B*, vol. 74, no. 4, 2006.

[127] M. K. Etherington, J. Wang, P. C. Y. Chow, and N. C. Greenham, "Recombination pathways in polymer:fullerene photovoltaics observed through spin polarization measurements," *Applied Physics Letters*, vol. 104, no. 6, p. 063304, 2014.

[128] A. L. Buchachenko and E. L. Frankevich, *Chemical generation and reception of radio- and microwaves*. VCH, 1994.

[129] Z. V. Vardeny, *Organic spintronics*. CRC Press/Taylor & Francis, 2010.

[130] D. R. McCamey, H. a. Seipel, S.-Y. Paik, M. J. Walter, N. J. Borys, J. M. Lupton, and C. Boehme, "Spin Rabi flopping in the photocurrent of a polymer light-emitting diode.," *Nature Materials*, vol. 7, no. 9, pp. 723–728, 2008.

[131] J. Behrends, A. Schnegg, K. Lips, E. A. Thomsen, A. K. Pandey, I. D. W. Samuel, and D. J. Keeble, "Bipolaron formation in organic solar cells observed by pulsed electrically detected magnetic resonance," *Physical Review Letters*, vol. 105, no. 17, pp. 12–15, 2010.

[132] C. Boehme and J. M. Lupton, "Challenges for organic spintronics," *Nature Nanotechnology*, vol. 8, no. 9, pp. 612–615, 2013.